University of Innsbruck

Master Thesis

Stable Reference Cavity for Er and Dy MOT Light

Alexander Patscheider

Supervised by Prof. Dr. Francesca Ferlaino
Institute of Experimental Physics, University of Innsbruck

Submitted to the Faculty of

Mathematics, Computer Science and Physics

February 10, 2017

Abstract

In this thesis we describe the setup and characterization of a reference cavity for the stabilization of laser light at several wavelengths. On the one hand, the cavity is used to stabilize light used for the magneto-optical trap of erbium and dysprosium atoms. On the other hand, we want to stabilize laser light for Rydberg excitation at a future date of the experiment. Additionally, the thesis covers the generation of the light at 583 nm and 626 nm, corresponding to the transitions in Er and Dy used for the narrow line MOT, respectively. For the generation of the light at 583 nm we use a seed laser emitting at 1166 nm. This light is then coupled into a Raman fiber amplifier and then frequency doubled within a second harmonic generation (SHG) crystal. With a seed power of 25 mW, we obtain slightly less than 2 W of 583-nm light. For the 626-nm light we use two fiber lasers at 1550 nm and 1050 nm together with two fiber amplifiers and mix the light in a sum frequency generation (SFG) crystal. With a maximal output power of 5 W for each fiber laser we obtain more than 2 W of light at 626 nm. The light at 626 nm is stabilized with a stable reference cavity. The two mirrors of the cavity and the spacer between them are made of ultra low expansion glass (ULE), which has a measured minimal thermal expansion coefficient at 21.78(5) °C. The locking of the laser light is done with a fiber-coupled electro-optical modulator that modulates sidebands at two different frequencies. While the laser is resonant to the atomic transition, one of these sidebands is shifted to the cavity resonance. The second sidebands are then used to generate the Pound-Drever-Hall error signal for the electronic locking setup.

Zusammenfassung

In dieser Masterarbeit beschreiben wir den Aufbau und die Charakterisierung eines optischen Resonators, welcher zur Stabilisierung von Laserlicht verwendet wird. Zum Einen wird damit das Licht, welches für die magneto-optische Falle von Erbium und Dysprosium benötigt wird stabilisiert. Zum Anderen soll der Resonator, zu einem zukünftigen Zeitpunkt des Experiments, für die Stabilisierung von Laserlicht für Rydberg Anregungen verwendet werden können. Des Weiteren behandelt die Masterarbeit die Erzeugung von Laserlicht bei einer Wellenlänge von 583 nm und 626 nm. Diese Wellenlängen entsprechen den optischen Übergängen, welche für die magneto-optische Falle für Erbium und Dysprosium verwendet werden. Für das Laserlicht bei 583 nm verwenden wir ein System aus einem Pump-Laser bei einer Wellenlänge von 1166 nm, zusammen mit einem Raman Faserverstärker und einem Kristall zur Frequenzverdopplung. Mit einer Pumpleistung von ungefähr 25 mW erhalten wir etwas weniger als 2 W Licht bei 583 nm. Für die Erzeugung von Licht bei 626 nm werden zwei Faserlaser bei den Wellenlängen 1550 nm und 1050 nm mit Faserverstärkern verstärkt und in einem nichtlinearen Kristall für Summenfrequenz addiert. Hier erhalten wir bei maximaler Leistung der Faserlaser (5 W) eine Ausgangsleistung von etwas mehr als 2 W. Die Spiegel des Resonators und der Abstandshalter dazwischen sind aus einem speziellen Glas (ultra low expansion glass), dessen thermischer Ausdehnungskoeffizient bei gemessenen 21.78(5) °C minimal ist. Zur Stabilisierung des Laserlichts werden mit einem fasergekoppeltem elektro-optischen Modulator Seitenbänder bei zwei unterschiedlichen Frequenzen auf das Licht aufmoduliert. Während der Laser zum atomaren Übergang resonant ist, wird ein Seitenband zur Resonatorresonanz geschoben und das zweite Seitenband zur Erzeugung des Pound-Drever-Hall Fehlersignals verwendet.

Contents

1. Introduction

At temperatures close to the absolute zero the atoms begin to reveal their quantum behavior. In 1911 Heike Kamerlingh Onnes observed that mercury looses suddenly its electric resistivity at a temperature of 4.2 K [43]. This discovery was related to the first realization of liquid ^{4}He only three years before. The superfluidity effect of liquid ^{4}He could be explained in 1938 by Kapitza, Allen, and Misener [3, 44]. In the following, in 1933 Walther Meißner and Robert Ochsenfeld discovered that superconducting materials repel an applied magnetic field and are therefore perfectly diamagnetic [66]. It took until 1957, when John Bardeen, Leon Neil Cooper, and John Robert Schrieffer found a theoretical microscopic approach to explain the macroscopic effect of superconductivity [9]. However, the understanding of superconductivity changed in 1986, when Johannes Georg Bednorz and Karl Alexander Mueller observed that the critical temperature, where the superconductivity appear, for copper oxide is much higher than for the materials known up to then. While for other materials the critical temperature is below 23 K for copper oxide the critical temperature is at 135 K [10]. Both, superfluidity and superconductivity, are macroscopic consequences of the bosonic and fermionic character or, more precisely, of the different statistical behavior of the particles. The Bose-Einstein statistics describes particles of whole-integer spin, called bosons. For zero temperature all identical particles occupy the lowest possible energy state in the system. On the other hand the Fermi-Dirac statistic describes the behavior of fermions (particles with half-integer spin) and at zero temperature each energy level up to the Fermi-energy is occupied by one single particle. The resulting states formed by the particles are called Bose-Einstein condensate for bosons and degenerated Fermi gas for fermions, respectively.

The complex nature of the superconductivity calls for the simulation of the systems in a better-controllable environment. The development of laser cooling techniques to cool particles with laser light to the μK regime and even lower temperatures lead to new opportunities for the investigation of many-body quantum systems and superfluidity.

With the observation of the first Bose-Einstein condensates (BEC) in 1995 [5, 13, 22], the field of ultracold atomic gases experienced a fast expansion. A special property of ultracold gases is that they allow a high controllability of internal and external degrees of freedom. Interparticle interactions can be controlled via Feshbach resonances [17], and optical lattices can be used to create spatial structures. This gives opportunity to enter a wide range of physical research fields connected to strongly correlated many-body systems as Quantum Simulators [30] and high-temperature superconductivity [19].

Among others, important aspects reached by the tunability of the interaction strength are the crossover from a BEC to a Bardeen-Cooper-Schrieffer superfluid state [39] and the superfluid to Mott transition with atoms in an optical lattice [37]. Early experiments with ultracold atomic gases haven been realized with alkali atoms as rubidium, lithium, cesium,

and sodium. With the condensation of chromium in 2005 [38] for the first time an atomic species was brought to degeneracy that carries a higher magnetic moment than alkali atoms, i. e. $6\,\mu_B$ instead of only $1\,\mu_B$. While for alkali atoms the properties are dominated by the isotropic and short range contact interaction for dipolar atoms the anisotropic and long range dipole-dipole interaction (DDI) comes into play. This makes dipolar elements of special interest for the investigation of new quantum phenomena. With chromium for example the d-wave collapse of the BEC [48] and the spin relaxation in an optical lattice have been investigated [68].

Since then, BECs and degenerated Fermi gases of erbium and dysprosium that carry even higher magnetic moments of $7\,\mu_B$ and $10\,\mu_B$, respectively, have been realized. The BEC of dysprosium was realized for the first time in the group of B. Lev [55] at Stanford, whereas the first realization of an erbium BEC was here in Innsbruck [1]. Dysprosium shares together with terbium the largest magnetic moment of all elements. While for chromium the contact interaction has to be reduced with a Feshbach resonance in order to make the DDI dominant, for erbium and dysprosium the DDI is dominant even without reducing the contact interaction.

Beside the large magnetic moment, erbium and dysprosium share additional special properties, which are the multi-valence electron character and the rich atomic electronic spectra containing many broad and narrow optical transitions [11, 54, 64] that can be used for laser cooling to very low temperatures. For both elements the $4f$ shell is not completely filled, which results in the high total angular momentum in the ground state. This high angular momentum, the large number of broad and narrow optical transitions, and the multi-valence electron characteristic give new possibilities for the growing field of Rydberg atoms. These are atoms where one electron is excited to a high principal quantum number n having a large spacial expansion, e. g. a rubidium atom excited to a state with $n = 43$ has an orbital radius that is larger by a factor of 40 compared to the ground state [57]. The combination of ultracold gases with Rydberg excitation has already lead to many exciting aspects such as the Rydberg blockade[77, 78] or the spatially ordered structure in a Rydberg gas [73]. Similar to atoms with two valence electrons, the core of the Rydberg atom remains optically active allowing imaging [65] and manipulation by light scattering [27].

The goal of our experiment is to combine for the first time two different strongly magnetic elements, erbium and dysprosium. The experiment will consist of three parts: the main chamber where the mixture experiments will be done and two additional chambers that will be attached at a later point. One of these additional chambers will be used to do Rydberg excitation experiments and for the other one a quantum gas microscope is planed.

About this thesis:

The purpose of this master thesis was to work on the generation and stabilization of the cooling light for the narrow-line MOTs of erbium and dysprosium and on the stabilization of future lasers for Rydberg excitation. For the cooling light for erbium, a seed laser in combination with a Raman fiber amplifier and a second harmonic generation crystal is used. For dysprosium we use a sum frequency generation crystal to add up the light of two fiber laser systems consisting of a fiber amplifier that is seeded by a fiber laser. For the stabilization we use a cavity with a spacer out of ultra low expansion glass (ULE) to lock

the lasers to the cavity resonance using a Pound-Drever-Hall locking scheme [25]. The assembling of the cavity and locking of the lasers was the main part of the presented thesis.

The thesis is structured as follows: In Chapter 2 the main properties of erbium and dysprosium such as atomic structure, energy spectra, and magnetic properties are discussed. The topic of Chapter 3 is the generation of the laser light for the MOTs of erbium and dysprosium. This contains a comparison of the parameters used in the already running experiments as well as a description of the laser systems that we will use in our experiment. In Chapter 4 a theoretical overview about cavities is given. Further, the requirements for our cavity such as thermal stability are discussed and the final design of the cavity is shown. The characterization and discussion of the cavity parameters is done in Chapter 5.

2. Overview on the Main Properties of Erbium and Dysprosium

In the last years the interest on strongly magnetic lanthanide atomic species increased significantly. These species give access to the study of dipolar phenomena. Recently, erbium (Er) and dysprosium (Dy) have been brought to quantum degeneracy with the creation of Bose-Einstein condensates and Fermi gases [1, 55]. In this chapter some general properties of Er and Dy such as level schemes, cooling transitions and magnetic moment are discussed.

2.1. Erbium and Dysprosium at Glance

Both, Er and Dy are rare-earth elements being part of the Lanthanide series of the periodic table. Er has an atomic number of 68 leading to a mass of 167.27 amu and Dy has an atomic number of 66 leading to a mass of 162.5 amu. The melting point of Er is 1529 °C, slightly higher than for Dy (1412 °C). This similarity is in principle an important added value when combining the two species for a quantum mixture experiment. Both, Er and Dy have different fermionic and bosonic isotopes. Er has five stable bosonic isotopes (^{162}Er, ^{164}Er, ^{166}Er, ^{168}Er, and ^{170}Er) and only one fermionic isotopes (^{167}Er). On the other hand Dy has also five stable bosonic isotopes (^{156}Dy, ^{158}Dy, ^{160}Dy, ^{162}Dy, and ^{164}Dy) but two stable fermionic isotopes (^{161}Dy, and ^{163}Dy) compared to Er. In Table 2.1 a list of all isotopes, which have a natural abundance above 1 % are listed for Er and Dy.

Table 2.1.: Relative abundances of the stable isotopes of Er and Dy which have a minimum abundance of 1 %. ^{167}Er, ^{161}Dy and ^{163}Dy are fermionic whereas the other isotopes are bosonic.

Isotope	^{164}**Er**	^{166}**Er**	^{167}**Er**	^{168}**Er**	^{170}**Er**
abundance (%)	1.61	33.6	23.0	26.8	15.0
	boson	boson	fermion	boson	boson

Isotope	^{160}**Dy**	^{161}**Dy**	^{162}**Dy**	^{163}**Dy**	^{164}**Dy**
abundance (%)	2.3	18.9	25.5	24.9	28.3
	boson	fermion	boson	fermion	boson

A special property of Er and Dy is their large magnetic moment of $7\,\mu_B$ and $10\,\mu_B$ where μ_B denotes the Bohr magneton, respectively. Together with terbium, Dy has the largest

magnetic moment of all elements. Table 2.2 gives an overview about some properties of Er and Dy.

Table 2.2.: Overview over some properties of Er and Dy. Z is the atomic number.
Note: 1 amu $\equiv$ $1.600\,539\,040(20) \times 10^{-27}$ kg [67].

	Z	mass (amu)	melting point (°C)	electron config.	mag. moment
Er	68	167.27	1529	[Xe] $4f^{12}6s^2$	$7\,\mu_B$
Dy	66	162.5	1412	[Xe] $4f^{10}6s^2$	$10\,\mu_B$

2.2. Atomic Structure

Following Mandelung's rule, the electrons for Er and Dy fill up as

$$[\mathrm{Xe}]\,4f^{12}6s^2 \qquad (\mathrm{Er}) \tag{2.1a}$$

and

$$[\mathrm{Xe}]\,4f^{10}6s^2 \qquad (\mathrm{Dy}). \tag{2.1b}$$

The notation in square brackets represent the electron configuration of Xenon,

$$(1s^2 2s^2 2p^6 3s^2 3p^6 3d^{10} 4s^2 4p^6 4d^{10} 5s^2 5p^6).$$

While the $4f$-orbital is only partially filled, the $6s$-orbital is completely filled up. This electron configuration is referred to as *submerged-shell* structure. The electrons in the $4f$-orbital have an angular momentum quantum number of $l = 3$. Considering the angular momentum projection quantum numbers $m_l = -l, \ldots, l$ and the spin projection numbers $m_s = \pm 1/2$ result in 7 states ($m_l = -3, -2, -1, 0, 1, 2, 3$), which can be doubly occupied. Therefore, in total up to 14 electrons can sit in the $4f$-orbital. The very similar electron configuration of the two atomic species to be stressed whereas Dy has 2 electrons less in the $4f$-shell compared to Er.

Depending on the spin-orbit coupling energy relative to the Coulomb interaction, different coupling schemes are necessary to find the respective quantum numbers. If the energy for the spin orbit coupling E_{s-o} is lower than the residual electrostatic interaction E_{re} the spin-orbit coupling scheme (LS-coupling[1]) can be applied. Otherwise, jj-coupling become relevant. For Er and Dy only for the ground state the LS-coupling scheme is sufficient, whereas for the excited states the jj-coupling has to be applied [80]. For the LS-coupling all spins and angular momenta add up to a total spin $\vec{S} = \sum_i \vec{s}_i$ and a total orbital angular momentum $\vec{L} = \sum_i \vec{l}_i$. The resulting total spin and total orbital angular momentum couple then to the total angular momentum, $\vec{J} = \vec{L} + \vec{S}$. Finally, the quantum state is denoted

[1]Russell-Saunders coupling scheme.

by $^{2s+1}L_J$. For Er and Dy all electron shells, except the $4f$-shell are completely filled, which results in a high total angular momentum in the ground state of $J = 6$ for Er and $J = 8$ for Dy, respectively.

Following the *LS*-coupling for the ground state results in $^3H_6$ for Er and $^5I_8$ for Dy. On the other hand, for the *jj*-coupling first the 4f electrons and the outer electrons couple independently via the *LS*-coupling scheme. This leads to two different quantum numbers J_1 and J_2 which by adding up form the final state written as $(J_1, J_2)_J$. As an example one can take the 583-nm MOT transition of Er, where an electron from the $6s$-orbital is excited to a $6p$-orbital ([Xe] $4f^{12}(^3H_6)6s6p(^3P_1^0)$). First, the inner electrons couple to $^3H_6$ and the outer electrons couple to $^3P_1$ by *LS*-coupling. Then, these two states couple to $(6, 1)_7^0$, where the subscript 7 denotes the sum $\vec{J} = \vec{j_1} + \vec{j_2}$ and the subscript 0 refers to odd party.

The bosons of Er and Dy have no hyperfine structure because their nuclear spin I is zero. In contrary, the fermionic isotope ^{167}Er has $I = 7/2$, which results in a hyperfine structure quantum number $F = 19/2$, whereby the angular momentum J couples to the nuclear spin I. For Dy the nuclear spin is $I = 5/2$, which leads to $F = 21/2$ for the electronic ground state. Table 2.3 gives a summary over all quantum numbers in the ground state of Er and Dy.

Table 2.3.: Quantum numbers for the ground state of Er ($^3H_6$) and Dy ($^5I_8$).

	Erbium	Dysprosium
total orbital angular momentum L	5	6
total spin S	1	2
total angular momentum J	6	8
nuclear spin I for bosons	0	0
nuclear spin I for fermions	$7/2$	$5/2$
total angular momentum F for fermions	$19/2$	$21/2$

Figure 2.1 shows the atomic spectra for Er and Dy. States, which are labeled in red, refer to even parity and states in black have odd parity. This very rich atomic spectra contain many different possible cooling transitions.

2.3. Laser-Cooling Transitions in Erbium and Dysprosium

The plan for the experiment is to have first a transversal cooling section (TC) to collimate the divergent beam coming out of the oven. To decelerate the atoms before trapping them a Zeeman slower is used (ZS). For the TC and the ZS the broad blue transitions (401 nm for Er and 421 nm for Dy) are used. Since one atom has to scatter many photons over a short time period transitions with a short lifetime are preferred. Additionally, the wavelength should be small, leading to a higher recoil velocity[2]. For Er (Dy) the transition at 401 nm (421 nm) has a lifetime of 4.94 ns (5.35 ns) and a recoil velocity of 6 mm/s (5.8 mm/s). Assuming, that

[2] $v_{\mathrm{rec}} = \hbar k/m$. Here, $\hbar$ is the reduced Plack's constant, m the atomic mass, and k_{B} the Boltzmann constant.

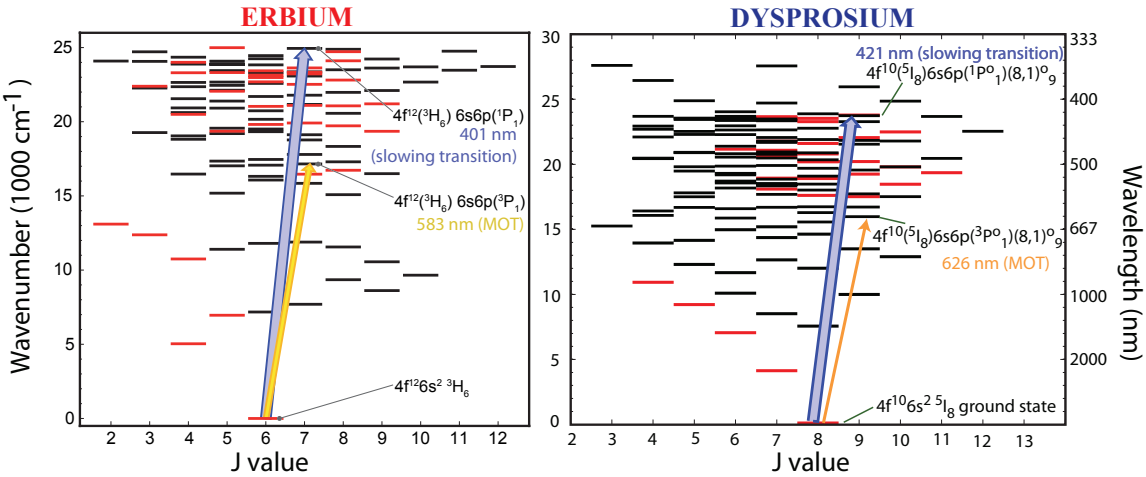

Figure 2.1.: Atomic spectra and cooling transitions of Er and Dy. In our experiment we will use the 583-nm and 626-nm transitions for the Er and Dy MOT whereas the transitions of 401 nm and 421 nm will be used for the transversal cooling and the Zeeman slower, respectively. Red lines represent states with even parity and black lines states with odd parity. Graphics taken from [8, 81].

Table 2.4.: Electron configurations and quantum numbers of the excited states. First the electrons of the inner and outer shell couple independently via the *LS*-coupling scheme and then they couple via the *jj*-coupling.

	electron configuration	*jj*-coupling
401 nm	$[\mathrm{Xe}]\,4f^{12}(^3H_6)6s6p(^1P_1^0)$	$(6,1)_7^0$
583 nm	$[\mathrm{Xe}]\,4f^{12}(^3H_6)6s6p(^3P_1^0)$	$(6,1)_7^0$
421 nm	$[\mathrm{Xe}]\,4f^{10}(^5I_8)6s6p(^1P_1^0)$	$(8,1)_9^0$
626 nm	$[\mathrm{Xe}]\,4f^{10}(^5I_8)6s6p(^3P_1^0)$	$(8,1)_9^0$

the atoms coming from the oven have a velocity of approximately 500 m/s, roughly 80 000 photons have to be scattered to slow the atoms down to 10 m/s, which is a adequate capture velocity [33, 61]. The broadness of the transition is a useful characteristic because more photons can be scattered by the atoms. After the ZS the atoms reach the main chamber with the MOT. For the MOT we use the 583-nm transition for Er and the 626-nm transition for Dy. For both, Er and Dy this means that one electron from the $6s^2$ state is excited to a $6p$ state and couple with the remaining $6s$ electron to a triplet $^3P_1$ state. Table 2.4 shows the electron configuration of the excited states of the laser cooling transitions.

The temperature limit of the Doppler cooling is given by the Doppler temperature[3], which is proportional to the linewidth of the transition. The smaller the linewidth, the lower the reachable temperature. The Doppler temperatures for the used transition are

[3] $T_\mathrm{D} = \hbar\Delta\nu/2k_\mathrm{B}$. Here, $\hbar$ is the reduced Plack's constant, $\Delta\nu$ the natural linewidth $\Gamma/2\pi$, and k_B the Boltzmann constant.

$T_D = 4.6\,\mu K$ for Er and $T_D = 3.3\,\mu K$ for Dy. In principle, also the 401-nm and 421-nm transitions could be used for the MOT, but due to the relatively high Doppler temperature of $T_D = 714\,\mu K$ for Er and $T_D = 773\,\mu K$ for Dy additional cooling steps would have to be implemented. A low temperature is preferred because of a higher loading rate into a dipole trap. For laser cooling it is very important to have a close cycling transition. This means, that most of the excited atoms do not get lost in a metastable state, but decay back into the ground state. In a metastable state the atoms would became dark to the cooling light. A big advantage of the MOT transitions for Er and Dy is that no repumper is needed because the decay probability into intermediate states is very low. For Er there are two possible intermediate states with transition probabilities of 0.017 and 0.0049 [8]. Table 2.5 gives, a list of relevant parameters of the cooling transitions, which will be used in our experiment.

Table 2.5.: Important parameters of the cooling transition of 401 nm, 421 nm, 583 nm, and 626 nm [8, 56, 58].

Parameters		Erbium		Dysprosium	
		401 nm	583 nm	421 nm	626 nm
transition rate	Γ ($^1/_s$)	1.87×10^8	1.17×10^6	2.02×10^8	0.85×10^6
lifetime	τ (ns)	5.35	857	4.94	1170
natural linewidth	$\Delta\nu$ (MHz)	29.7	0.19	32.2	0.136
saturation intensity	I_S ($^{mW}/_{cm^2}$)	60.3	0.13	56.3	0.072
doppler temperature	T_D (µK)	714	4.6	773	3.3
doppler velocity	v_D ($^{mm}/_s$)	267	21	198	12.9
recoil temperature	T_r (nK)	717	339	659	298
recoil velocity	v_r ($^{mm}/_s$)	6.0	4.1	5.8	3.9

The different isotopes of Er and Dy have different numbers of neutrons and therefore different masses. This leads to a different distribution of the electrons, resulting in a change of the charge distribution, causing a shift of the energy levels. Figure 2.2 shows this isotope shift for the bosonic isotopes of Er and Dy, which have a natural abundance above 1 %. The isotope shift for both elements is on a comparable order.

2.4. Magnetic Properties

A very special property of these two elements is their large magnetic moment of $7\,\mu_B$ for Er and $10\,\mu_B$ for Dy, where μ_B denotes the Bohr magneton. This is in contrast to other elements as alkali atoms, having a $^1S_0$ state as ground state. The exact value of the magnetic moment μ can be calculated using

$$\mu = m_J g_J \mu_B, \tag{2.2}$$

where m_J is the projection of the total angular moment in the direction of a magnetic field and g_J is the Landé g-factor, also known as the gyromagnetic ratio. The Landé factor can be calculated by [23]

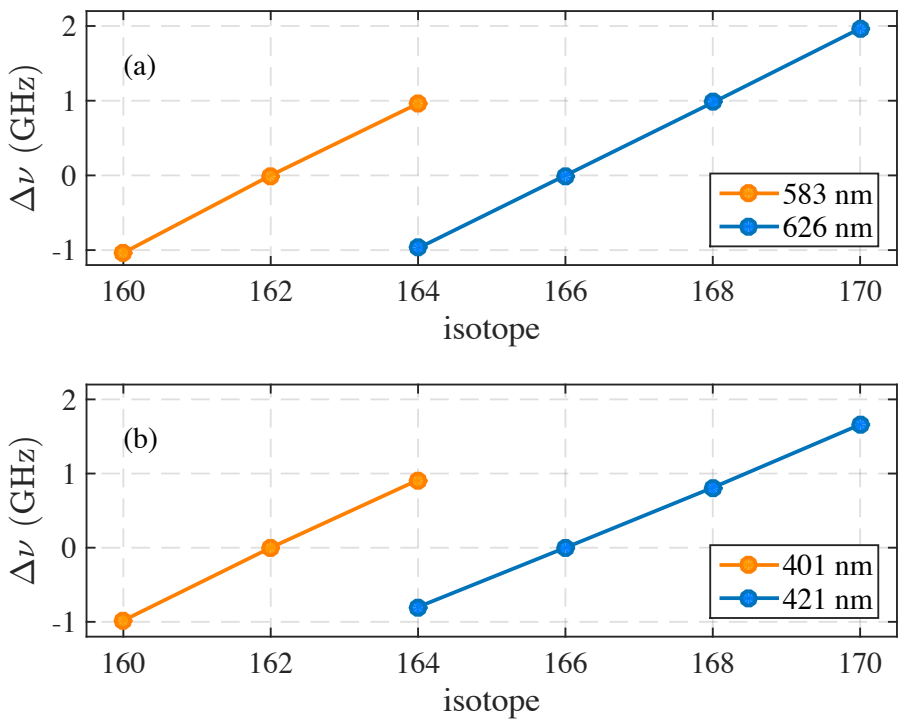

Figure 2.2.: The isotope shifts of (a) the 583-nm (Er) and 626-nm (Dy) transitions and (b) the 401-nm (Er) and 421-nm (Dy) transitions [20, 41, 42, 50].

$$g_J = 1 + \frac{J(J+1) - L(L+1) + S(S+1)}{2J(J+1)}. \tag{2.3}$$

However, corrections due to deviations from the LS-coupling and other effects, e. g. relativistic corrections, have to be considered. Inserting the Landé factor $g_J = 1.163801(1)$ [21] for Er and $g_J = 1.2415867(10)$ [29] for Dy and assuming that the atoms in the ground state are sitting in the $m_J = 6$ or $m_J = 8$ level leads to a magnetic moment of $6.98\,\mu_\mathrm{B}$ and $9.93\,\mu_\mathrm{B}$, respectively. By applying an external magnetic field, the energy level with total angular momentum quantum number J split up in $2J+1$ sub states with magnetic quantum number m_J. In Figure 2.3 the Zeeman splitting for ground state of the bosonic isotopes of Er and Dy is plotted for a magnetic field B up to 5 G. The energy shift can be calculated by

$$\Delta E(B) = m_J g_J \mu_\mathrm{B} B. \tag{2.4}$$

For the fermionic isotopes the hyperfine structure has to be taken into account and the underlying values are the m_F state and the Landé g-factor g_F. For the lowest hyperfine state ($F = {}^{19}/_2$ and $m_F = -{}^{19}/_2$ for Er and $F = {}^{21}/_2$ and $m_F = -{}^{21}/_2$ for Dy) the magnetic moment has the same value as for the bosonic ground state.

This large magnetic moment leads to completely different scattering properties since the dipole–dipole interaction is fundamentally different from the contact interaction. For two

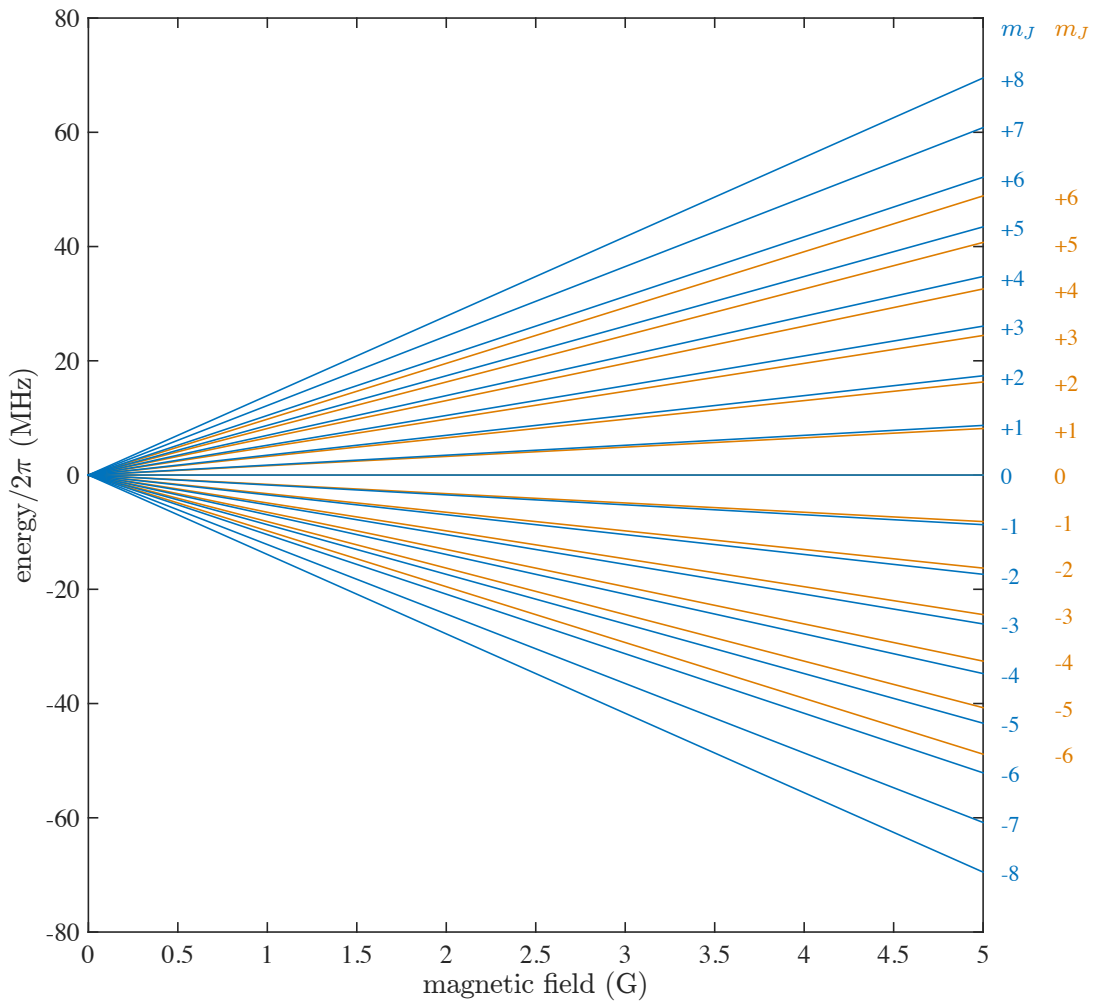

Figure 2.3.: Linear Zeeman energy splitting for the the ground state of the bosonic isotopes of Er (orange) and Dy (blue) with $J = 6$ and $J = 8$, respectively. On the right hand site of the graph the projection quantum number m_J is given.

particles with dipole moments along the unit vectors $\mathbf{e}_1$ and $\mathbf{e}_2$ the dipole–dipole interaction reads as [49]

$$U_{\mathrm{dd}}(r) = \frac{\mu_0 \mu^2}{4\pi} \frac{(\mathbf{e}_1 \cdot \mathbf{e}_2)\mathbf{r}^2 - 3(\mathbf{e}_1 \cdot \mathbf{r})(\mathbf{e}_2 \cdot \mathbf{r})}{\mathbf{r}^5}, \tag{2.5}$$

where $\mathbf{r}$ is the relative position of the atoms to each other. For a polarized sample this simplifies to

$$U_{\mathrm{dd}}(r) = \frac{\mu_0 \mu^2}{4\pi} \frac{1 - 3\cos^2(\theta)}{r^3}, \tag{2.6}$$

where θ is the angle between the direction of the polarization and the position vector $\mathbf{r}$. The two main properties of U_{dd} are the long-range character, identifiable from the factor $1/r^3$ and the anisotropy deriving from the symmetry of the Legendre polynomial of second order, $P_2(\cos\theta) = \frac{1}{2}(1 - 3\cos\theta)$. Since θ can vary between 0 and $\pi/2$, the dipole-dipole interaction can be either repulsive for atoms sitting side by side or attractive for atoms sitting in a

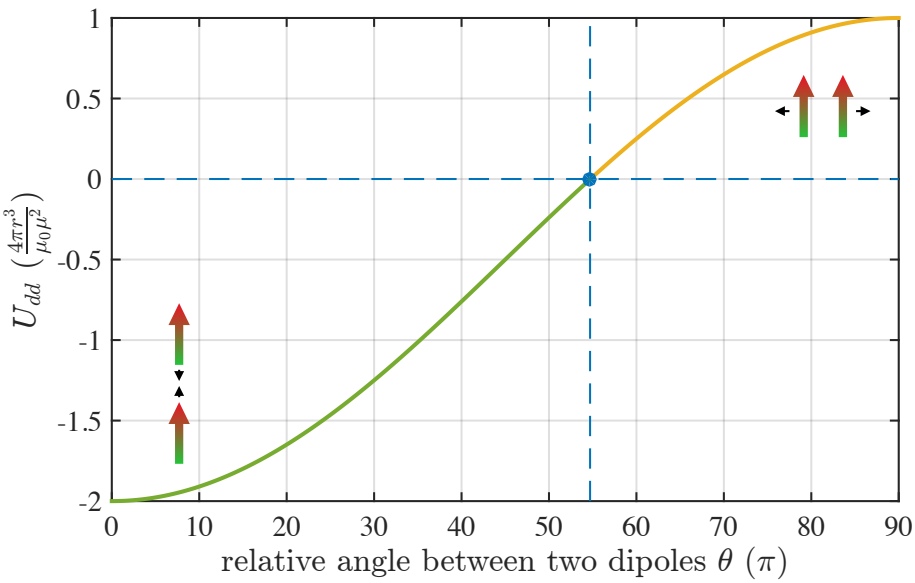

Figure 2.4.: Strength of the dipole-dipole interaction U_{dd} in dependence of the relative angle between the dipole orientation at a fixed distance r. The green part stands for attractive interaction and the red line for repulsive interaction, respectively. The blue dot marks the so called 'magic angle', where the dipole-dipole interaction vanishes.

'head to tail' configuration. Figure 2.4 shows the strength on the dipole–dipole interaction in dependence of the relative angle between the polarization and the relative position of the dipoles at a fixed distance r. For the special angle $\theta = 54.7\,^{\circ}\mathrm{C}$ the dipole–dipole interaction vanishes.

3. Laser Systems for Er-Dy Double MOT

In this Chapter, we will describe the two laser systems used for the narrow line magneto-optical traps (MOTs) of Er and Dy and the expected requirements for MOT production.

3.1. Dual Species Magneto Optical Trap

Among the different possible laser cooling transitions, Er and Dy feature an intercombination-type line, which is broad enough to provide efficient laser cooling but narrow enough to have conveniently low Doppler temperatures. This is the case of the transition at 583 nm for Er and at 626 nm for Dy. For both species, single-species MOTs are currently successfully operating on such transitions [24, 33, 61]. The relatively narrow linewidths of around $\Gamma \approx 2\pi \cdot 150\,\mathrm{kHz}$ arise as a result of a transition from the ground state being a singlet state to an excited state being a triplet state (intercombination line).

The experimental sequence in the experiments, where the narrow line MOTs are realized, is as follows: First, the atoms are loaded from the Zeeman slower (SL) into a MOT with largely detuned laser light compared to their natural linewidth, i. e. approximately $-40\,\Gamma_{583}$ for Er and $-35\,\Gamma_{626}$ for Dy, respectively. Due to the large detuning the atoms do not feel a homogeneous light force over the volume of the MOT but are resonant with the light on an ellipsoid of constant magnetic field [32]. Due to the gravitational force, the atoms will accumulate in the lower region of this ellipsoid and form a characteristic bowl-shaped MOT. This automatically prevents the Zeeman slower light to reduce the atom number in the MOT by exerting a light force on the atoms. Since for the double species MOT both atomic species feel the same magnetic field gradient, the position relative to each other can be influenced by the detuning. In a second step the MOT is compressed (cMOT) to reach lower temperatures and a higher density of the atomic cloud. During the compression the magnetic field gradient is changed as well as the detuning and the light intensity. Figure 3.1 shows a schematic representation of the passage from a MOT to a cMOT for the simple case with a $J = 0 \rightarrow J' = 1$ transition. Table 3.1 gives some typical parameters used in [61] and [33] for the realization of the narrow line MOTs.

In summary this narrow line transitions provide a exceptionally good starting point for the subsequent direct loading of a dipole trap due to the already low final temperatures and large atom densities reached after the cMOT step. Both species, Er and Dy reach similar final temperature, atom number, and atom density for comparable detunings and magnetic field gradients. This leads to the promising chance of realizing a simultaneous double species MOT using adequate trade-off parameters especially for the magnetic field gradient.

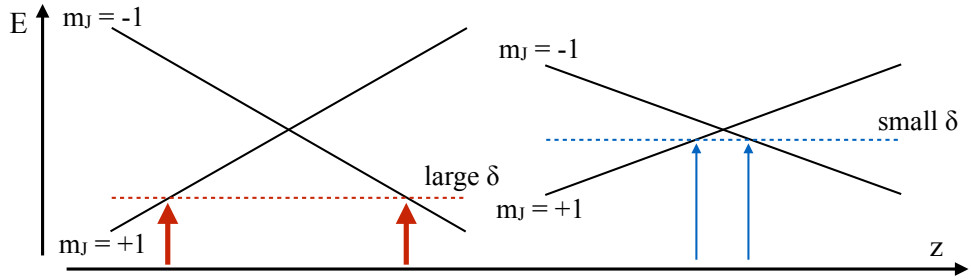

Figure 3.1.: Representation of a transition from a MOT to a cMOT. For the cMOT the magnetic field gradient, the beam intensity and the detuning are reduced compared to the starting MOT.

Table 3.1.: Summary of the parameters used for the narrow line MOTs in [61] and [33].

	Erbium	**Dysprosium**
transition	583 nm	626 nm
natural linewidth Γ	0.19 MHz	0.136 MHz
magnetic field gradient MOT	2.6 G/cm	3 G/cm
detuning MOT	$-40\,\Gamma_{583}$	$-35\,\Gamma_{626}$
magnetic field gradient cMOT	0.9 G/cm	1.5 G/cm
detuning cMOT	$-9.5\,\Gamma_{583}$	$-2.75\,\Gamma_{626}$
final temperature	10 µK	6 µK
final atom number	2×10^8	1.5×10^8
final atom density	1.5×10^{11} /cm^3	8.6×10^{10} /cm^3

An issue that could have a negative influence on the double-species MOT are possible cross talks. This means that the light at 583 nm for the Er MOT could have an effect on the Dy atoms and the light at 626 nm could have an effect on the Er atoms. Table 3.2 and 3.3 give the closest known transitions with respect to the MOT transition of each species.

Table 3.2.: Closest Er transitions near Dy MOT line.

$J \rightarrow J'$	λ (nm)	$\Delta\nu = \Gamma/2\pi$ (kHz)
$6 \rightarrow 6$	622.102	133.7
$6 \rightarrow 6$	620.2	55

Table 3.3.: Closest Dy transitions near Er MOT line.

$J \rightarrow J'$	λ (nm)	$\Delta\nu = \Gamma/2\pi$ (kHz)
$8 \rightarrow 7$	565.36	71
$8 \rightarrow 8$	597.6	67
$8 \rightarrow 7$	599.02	90

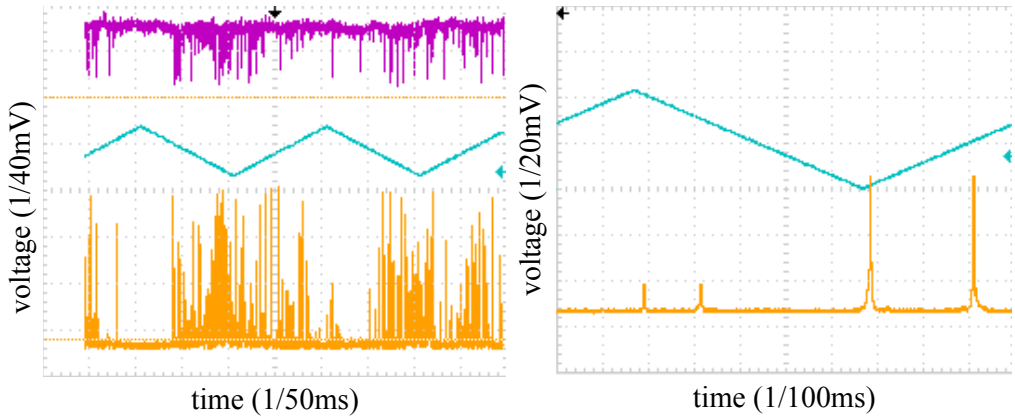

(a) Acoustic noise on the laser of 1166 nm.

(b) The acoustic noise is removed with the flexure laser design.

Figure 3.2.: Figure (a) shows the acoustic noise on the light of 1166 nm. The noise was removed (b) by changing the laser design to the flexure design. Blue is the voltage applied for the piezo scan, orange is the cavity transmission, and in (a) purple is the cavity reflection. The scan ramp is not symmetric to the cavity transmission.

The final performance of the double-MOT will also crucially depend on interspecies inelastic collisions, which have to be investigated experimentally [36].

3.2. Laser System for 583-nm Light for Erbium

To create the 583-nm light for the narrow line MOT of Er we use a commercial Raman amplifier from MPB Communications, which is seeded from a homemade grating-stabilized external cavity diode laser (ECDL) at 1166 nm.

External cavity diode laser at 1166 nm

As already mentioned above we plan to use a home built ECDL as a seed laser. There are only a few laser diodes available covering the needed wavelength of 1166nm. We chose a high power gain chip[1] based on an InAs Quantum Dot with a central wavelength at 1178 nm and a tuning range of 50 nm.

Initially, we used a laser design, which was frequently used in Innsbruck, e. g. in [76]. However, we observed a high sensitivity to acoustic noise. Figure 3.2(a) shows the cavity transmission of the 583 nm while scanning the laser over the cavity resonance. Although higher transversal modes are suppressed by the coupling, many other modes appeared when clapping or knocking on the laser table. Changing to a flexure-based laser design [47] solved this issue. Figure 3.2(b) shows the cavity transmission of the 583 nm laser with the flexure-based laser as a seed laser. The laser design works in Littrow-configuration, where

[1] GC–1178–TO–200 from Innolume, 200 mW @ 1178 nm.

the 1th diffraction order of the grating is reflected into the gain chip and the 0th order is used as an output. In comparison to the first Innsbruck design the diffraction grating and the output coupling mirror of the new design are glued on a compact flexure instead of a mirror mount. Figure 3.3 shows the design of the flexure laser. The gain chip is mounted in a

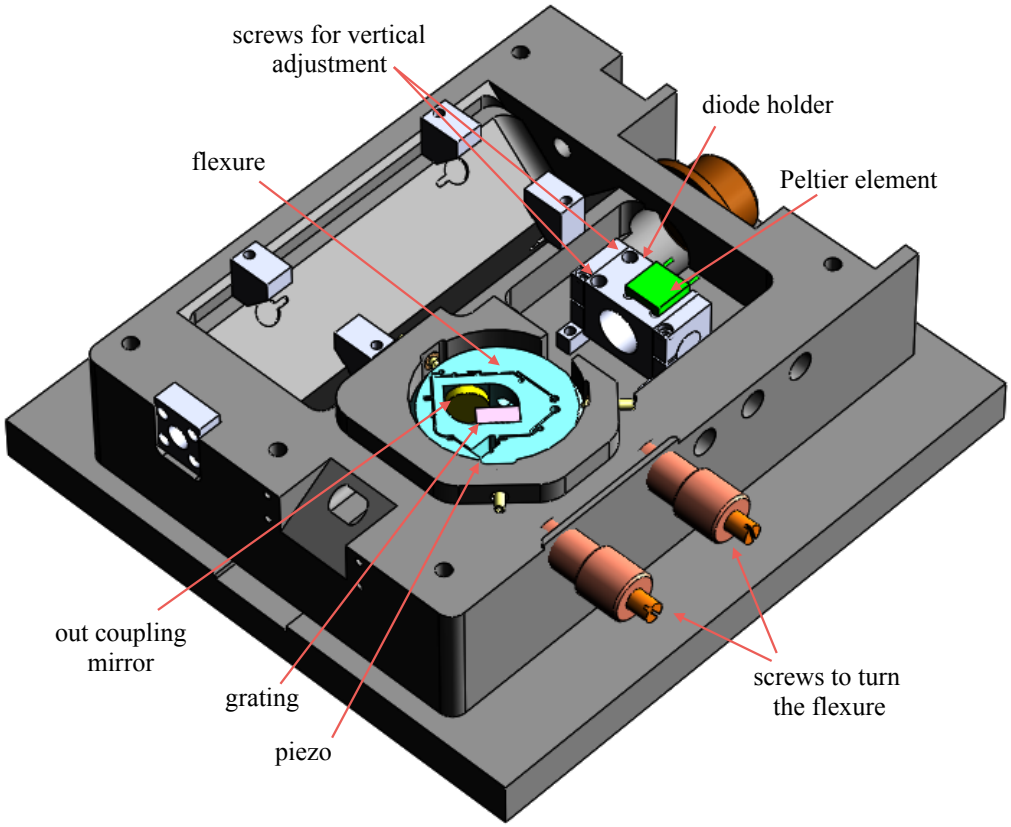

Figure 3.3.: Drawing of the flexure type laser design. The gain chip is fixed in the diode holder, which is temperature stabilized by the Peltier element. Two screws are placed in the diode holder for the vertical adjustment. For rough wavelength adjustment the flexure (blue) is turned with the brown screws on the side. The piezo element is for the fine adjustment of the wavelength.

standard collimation package from Thorlabs[2] which is used for collimation of the light. The collimation package tube sits inside an aluminum holder which gets temperature stabilized via a Peltier element[3], see Fig. 3.3. The heat from the Peltier elements is removed via a heat sink, which is glued on the Peltier element and connected to the housing. The temperature stability is further improved by stabilizing the laser housing itself using additional Peltier elements sitting between the laser housing and the baseplate.

The wavelength of the laser is adjusted by turning the flexure, whereby the grating[4] is chosen in such a way, that the angle between the 0th order and the 1th order is approximately 45 degree. This ensures that the light leaves the laser without hitting the housing. The

[2]e. g. Thorlabs LT230P-B.
[3]e. g. Peltier element with 5.1 W, 2.2 A, and 3.8 V.
[4]For 1166 nm the grating GH13-12V from Thorlabs is chosen.

rough wavelength adjustment is done by turning the flexure via two adjustment screws that press on the flexure. The fine adjustment as well as the scanning of the wavelength is done using a piezo element placed in the flexure and fixed with a screw that presses on the piezo. The special structure in the flexure allows to turn the grating without turning the whole flexure when applying a voltage to the piezo. The laser housing provides additional space for a filter- or prestabilization cavity and the possibility to evacuate the whole housing for additional temperature- and acoustic shielding. However, the linewidth and acoustic noise shielding are already sufficient without those options.

Figure 3.4 shows the characterization of the achievable output power of the 1166 nm laser for three different temperatures. For a better clearness the data points are shown without error bars. The error can be assumed with approximately 5 %. The threshold of

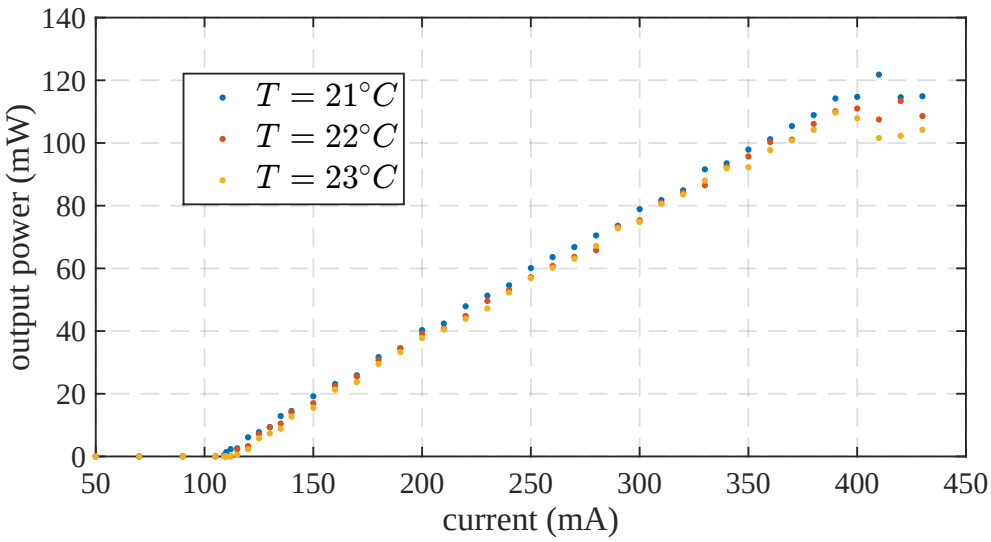

Figure 3.4.: Output power of the 1166 nm laser as a function of the current for three different temperatures. Error bars are not shown for clarity.

the gain chip was between 109 mA for 21 °C and 115 mA for 23 °C. Although the gain chip is specified up to 800 mA the output power shows a saturation after 400 mA. Since only 20 mW of 1166-nm light are needed for seeding the Raman fiber amplifier we restricted the the maximal current used to below this value to avoid this problem. Unfortunately, the Quantum Dot chip behaves in frequency domain differently than what expected (see discussion below). Therefore, we finally decided to buy a commercial system as a seed laser at 1166 nm.

Raman fiber amplifier

The commercial system consists of three elements:

- Ytterbium Fiber Laser

- Raman Fiber Amplifier
- Second Harmonic Generator

The working principle of the amplifier is based on induced Stokes-Raman-scattering, where both a pump photon and a photon of the desired frequency enter the optical material. For the Raman fiber amplifier the optical material is based on a single-mode polarization-maintaining fiber. The Stoke-Raman-scattering describes a photon at a certain frequency ν_1 interacting with the material and leaving either with lower frequency $\nu_s = \nu_1 - \nu_R$ (Stoke-Raman-scattering) or with higher frequency $\nu_A = \nu_1 + \nu_R$ (anti-Stoke-Raman-scattering). ν_R is the frequency of an oscillation- or ration mode of a molecule or a solid. The entering photon either transfer energy to the medium or gets energy from the medium. The induced Stoke-Raman-scattering occurs when a photon enters the medium together with a pump photon of higher frequency (Stoke-Raman-scattering). The photon induces the emission of a second photon, which has the same frequency as the first one. In our case, this leads to an amplification of the seed light by about a factor of ≈ 300.

After the amplification stage, the light gets frequency doubled in a Second Harmonic Generator (SHG), which in this case uses a periodically-poled lithium niobate crystal (PPLN) in single-pass configuration. The special property of a non linear crystal is that the polarization of the medium does not depend linearly on the electric field. The polarization of the material can be written as Taylor expansion. For a non linear crystal, where higher orders except the second can be neglected, the non-linear polarization of the medium in dependence of the electric field $E = \mathrm{Re}\{E(\omega)\exp(i\omega t)\}$ of the incident light can be written as

$$P_{\mathrm{nl}} = \chi^{(2)} E^2. \tag{3.1}$$

$\chi^{(2)}$ is the second order electric susceptibility, describing the strength of the non linear response. In general, $\chi^{(2)}$ is a tensor of 3th rank. However, for simplicity we take P_{nl} and E to be scalar quantities. Inserting the electric field $E = \mathrm{Re}\{E(\omega)\exp(i\omega t)\}$ gives for the polarization

$$P_{\mathrm{nl}}(t) = P_{\mathrm{nl}}(0) + \mathrm{Re}\{P_{\mathrm{nl}}(2\omega)\exp(i2\omega t)\},$$

which consists of the linear term $P_{\mathrm{nl}}(0)$ and the frequency doubled term $\mathrm{Re}\{P_{\mathrm{nl}}(2\omega)e^{i2\omega t}\}$.

PPLN is a material engineered being quasi-phase-matched. This means, that the orientation of the electric susceptibility of the crystal is inverted periodically. This avoids that the generated photons run out of phase to each other and interfere destructively. The needed period of the alternating crystal is set by the desired wavelength to be generated. The doubling efficiency, according to the company, is about 30 %.

Figure 3.5 shows the optical setup of the home made 1166 nm seed laser together with the commercial Raman fiber amplifier and the SHG crystal. An optical isolator[5] is placed to prevent that light is back reflected into the laser and disturbs the behavior of the gain chip. The 1166-nm light is fed into the Raman fiber amplifier and transported to the SHG crystal via optical fibers. Afterwards, the 583-nm light is spitted into three paths, which go to the

[5]Isowave Manufacturing: I-11B-4.

experiment, the cavity, and the wavemeter. The intensity of the 583-nm light, which goes to the experiment is stabilized with an acousto-optical modulator[6] (AOM).

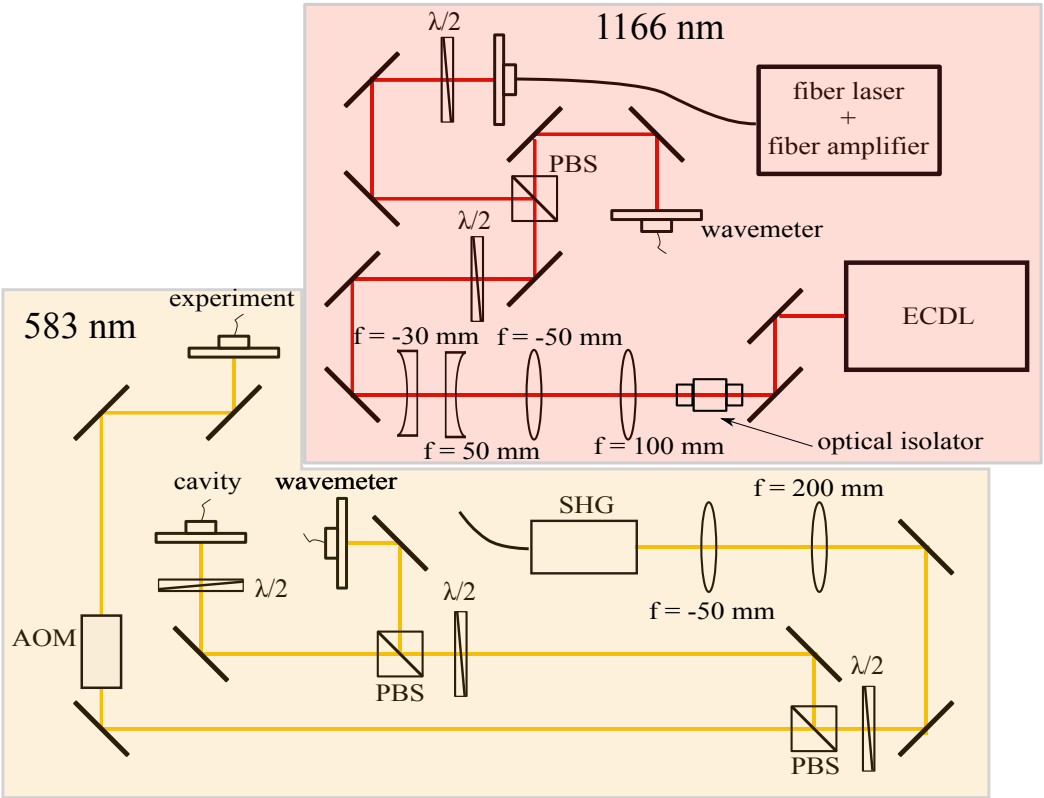

Figure 3.5.: Drawing of the optical setup for the generation of the 583-nm light. The setup is divided into the seed laser at 1166 nm and the SHG crystal with the 583 nm light.

Figure 3.6(a) shows the output power of the 583-nm light for different pump laser currents. The current is representative for the pump power. The output power also depends on the temperature of the crystal as the phase matching condition for the SHG crystal has to be fulfilled. As the temperature inside the crystal changes with the total power, the set temperature of the SHG crystal has to be adjusted for each current to maximize the output power. Figure 3.6(b) shows the output power as a function of the crystal temperature when the pump power was kept constant (4.5A). To extract the temperature at which the output power is maximal we fit $P(T) = A + B \cdot \mathrm{sinc}^2(C(T - D))$ to the data points. The fit describes the central part well and we obtain a maximum power at a temperature of 64.97(2) °C. The idea for the locking of the laser is to generate the error signal (see Sec 5.4) with the 583-nm light and feed the error signal to the 1166-nm ECDL.

[6]Gooch & Housego, 3080-215.

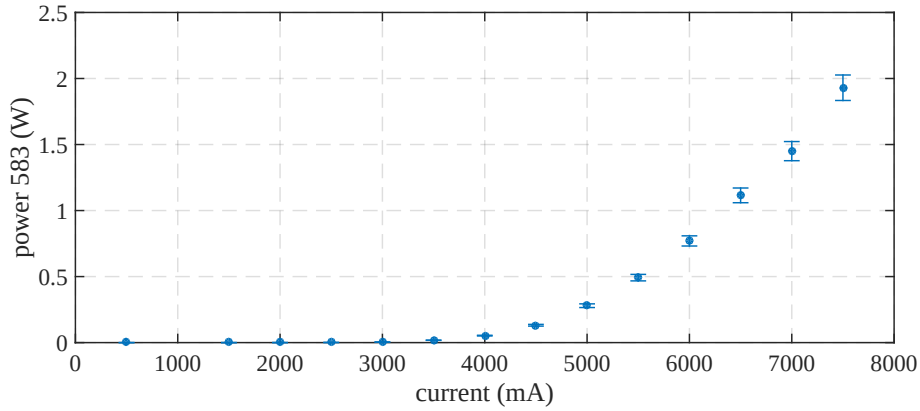

(a) Power of the 583-nm light as a function of the current of the pump laser.

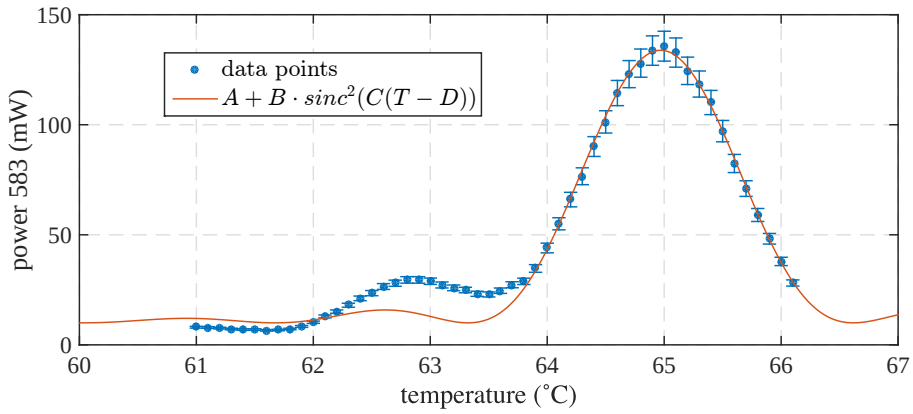

(b) Power of the 583-nm light as a function of the temperature of the SHG crystal.

Figure 3.6.: Output power of the system for the generation of 583 nm light. (a) shows the output power of 583-nm light vs. the current of the Ytterbium fiber laser. In (b) the output power of 583-nm light vs. the temperature of the SHG crystal is plotted. The amplifier current was at 4.5 A. For both measurements the seed power at 1166 nm was at 25 mW.

Issues with the Seed Laser at 1166 nm

After coupling the 583-nm light into our home built cavity (see Chap. 4) we observed that the laser was not always running single mode and sensitive to the current. Already a very slight change of the current lead to a mode-hop or a change from single-mode to multi-mode. Furthermore, it happened that after running single mode for some time the laser jumps into multi mode. The minimum time between we observed being single mode and multi mode was only a few minutes, whereas the maximum time observed was 1 to 2 hours. The current plateau, where the laser was single mode, was determined to be 0.6 mA, which makes single-mode operation at the desired wavelength very challenging. Additionally, it was observed that the long term stability of the wavelength was not satisfying. To test this, the laser was kept switched on for one night, whereby the next morning the laser was multi mode and it was not possible to get the laser back to the desired wavelength by adjusting the current and the temperature. A priori it was not clear if the laser diode itself, the electronics for the diode current or the temperature stabilization are responsible for this behavior. After careful testing of different electronics and checking the temperature stability, we concluded that the laser diode itself was responsible for the frequency instabilities. A possible solution for this issues is to use a different type of gain chip. For an ECDL, two types of gain chip are available: type A and type B. While type A has a straight stripe normal to the facets type B has a curved stripe. The tilted stripe has the advantage of reducing the self lasing and minimizing gain ripples. Another improvement would be the reduction of the cavity length of the ECDL since this would increase the current plateau where the laser runs single-mode.

From the experiences of previous experiments [33] an optimal intensity for the narrow line MOT of Er is $12 \times I_{\text{sat}}$, which leads to a total power requirement of

$$P_{583} = 12 \cdot I_{\text{sat}} \cdot A \cdot 3 \approx 60\,\text{mW}, \tag{3.2}$$

where the factor 3 refers to the three MOT beams (we use them in retro reflecting configuration), $A = \pi \cdot 4\,\text{cm}^2$ is the beam area with a beam waist of 2 cm and the saturation intensity $I_{\text{sat}} = 0.13\,\text{mW/cm}^2$ (see Table 2.5). This value for the power is just a reference value estimated with the experience of the running experiment. The exact necessary power has to be determined empirically.

3.3. Laser System for 626-nm Light for Dysprosium

The laser system we use for the creation of 626-nm has been implemented successfully in different experiments, e. g. in the groups of D. J. Wineland at NIST [79] and T. Pfau in Stuttgart [61]. The light is generated via sum frequency generation (SFG) of 1550-nm[7] and 1050-nm[8] light in a periodically poled lithium niobate (PPLN) crystal[9]. Fig. 3.7 shows the optical setup for the generation of the light 626 nm. An AOM[10] stabilizes the intensity, which goes to the experiment. The two laser systems consist of a seed laser and a fiber

[7]NKT Photonics: Koheras Boostik HPA Y10 System.
[8]NKT Photonics: Koheras Boostik HPA E15 System.
[9]Covesion: MSFG626-0.5-40.
[10]Gooch & Housego, 3080-215.

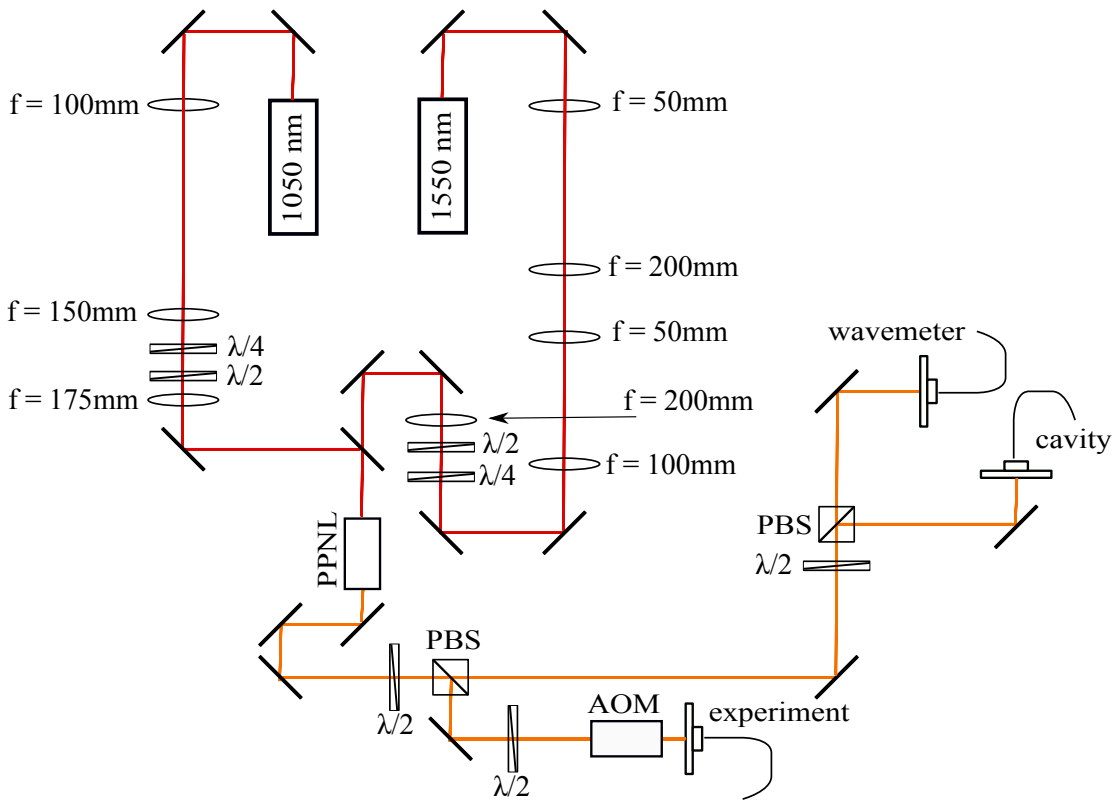

Figure 3.7.: Optical setup for the SFG of the 626-nm light. The 626-nm light is splitted into three paths: one is going to the experiment, one to the fiber coupled EOM/cavity and one goes to the wavemeter.

amplifier. The fiber amplifier for the 1550-nm system is a Er doped fiber laser, whereas the fiber amplifier for 1050-nm is ytterbium doped. The laser systems provide an output power of 5 W each and have a free running linewidth of < 1 kHz (1550 nm) and < 20 kHz (1050 nm). Both lasers can be tuned with a piezo element that has a modulation frequency limit up to 20 kHz. To lock the 626-nm we couple it into the ULE cavity and generate a PDH error signal, which we feed back to the 1050-nm seed laser while the system of 1550 nm remains free running (linewidth < 1 kHz). This is possible, because the lasers have a large mode-hop-free detuning range (10 GHz for 1050 nm and 8 GHz for 1550 nm) and a sufficient long term stability. Since the linewidth of the laser systems are small enough, the locking only needs to account for long term drifts. A more detailed description of the looking scheme is given in Sec. 5.4.

To generate the 626-nm light as efficient as possible the phase matching condition $\hbar k_{626} = \hbar k_{1550} + \hbar k_{1050}$ has to be fulfilled for the SFG crystal. The phase matching condition is fulfilled via the PPLN crystal, as explained already for the SHG crystal in Sec. 3.2. For the SFG crystal three different periodicities are available within one single crystal, 11.12 µm, 11.17 µm, and 11.22 µm, whereby we use the 11.22 µm. The quasi-phase-matching can be influenced slightly by varying the temperature of the crystal. In Figure 3.8(a) the power of the 626-nm light is plotted against the temperature of the PPLN crystal and fitted with

$P(T) = A + B \cdot \mathrm{sinc}^2(C(T - D))$. Although the data points are asymmetric, the sinc^2 describes the central part sufficiently good to extract the temperature with maximal power to 170.00(1) °C.

Additionally to the phase-matching, the intensity of the pump beams is important. Therefore, the 1550-nm and the 1050-nm light is focused into the crystal fulfilling approximately the condition $z_0 = l/2$, where z_0 is the Rayleigh length and l the length of the crystal. This is a rule of thumb recommended by Coevision. Our crystal has the dimensions (40×10×0.5) mm.

Similar to the SHF in Sec. 3.2, the SFG is based on the polarization P of the non-linear crystal. Inserting $E_{\mathrm{inc}} = E(\omega_1)e^{i\omega_1 t} + E(\omega_2)e^{i\omega_2 t}$ in Eq. 3.1 leads to

$$P_{\mathrm{NL}}(\omega_1 + \omega_2) = \chi^{(2)} \cdot E(\omega_1)E(\omega_2)e^{i(\omega_1+\omega_2 t)}, \tag{3.3}$$

oscillating at $\omega_1 + \omega_2$. Therefore, the amplitude of $P_{\mathrm{NL}}(\omega_1 + \omega_2)$ depends on the product of the amplitudes of the two incoming waves. In Figure 3.8(b) the product of the power of the pump lasers is plotted against the power of the 626-nm light. The conversion efficiency can be determined from the slope of a linear fit ($B \cdot x$), to the data points to

$$\eta_{\mathrm{conv}} = 9.48(34)\,\%$$

As for the 583-nm light the optimal intensity for the MOT can be estimated from the experience of a running experiment. In [24] a power of $\approx 50 \cdot I_{\mathrm{sat}}$ is used for each beam, leading to

$$P_{626} = 50 \cdot I_{\mathrm{sat}} \cdot A \cdot 3 \approx 135\,\mathrm{mW}, \tag{3.4}$$

where $I_{\mathrm{sat}} = 72\,\mu\mathrm{W/cm^2}$ is the saturation intensity and $A = \pi \cdot 4\,\mathrm{cm^2}$ is the beam area with a beam waist of 2 cm. The factor 3 arises from the three beams in retro reflecting configuration, which we will have for the MOT. This value is just a reference estimated with the experience of the running experiment [24]. The final necessary power has to be determined by optimizing the MOT loading phase in the experiment.

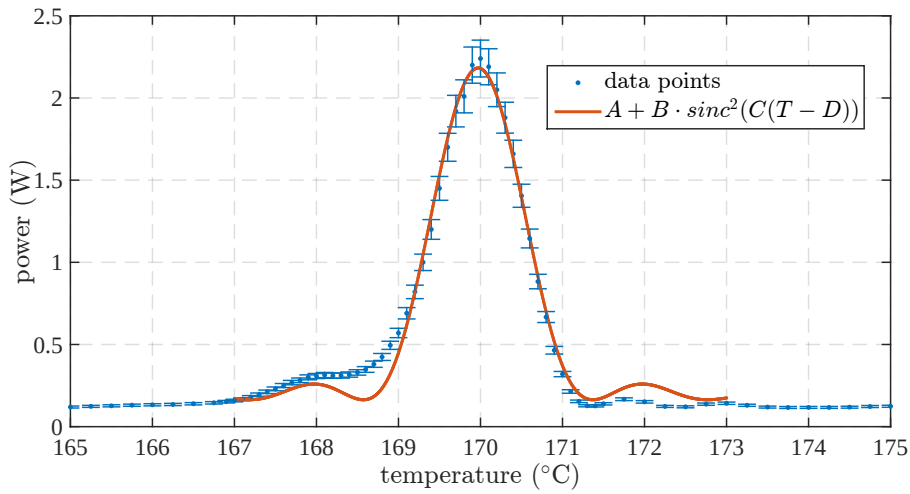

(a) Output power vs. Temperature of the SFG crystal at an amplifier current of $I_{1550} = 8.3$ A ($I_{1050} = 6$ A) and a seed laser output power of $P_{1550} = 6.7$ mW ($P_{1050} = 6.6$ mW).

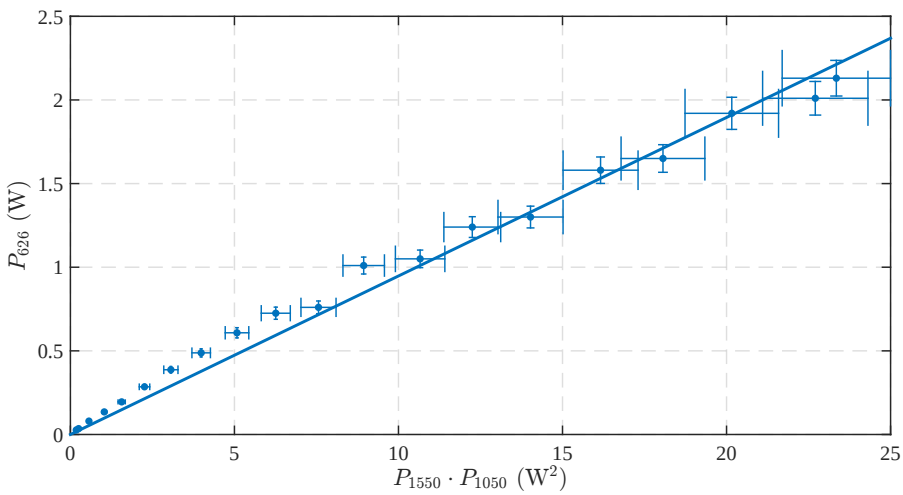

(b) The output power of 626-nm light is plotted versus the product of the power of the 1550 nm and 1050 nm laser (circles). The data points are fitted with a linear function $B \cdot x$.

Figure 3.8.: Output power of the system for the generation of 626 nm light. (a) shows the output power of 626-nm light in dependence of the temperature of the PPLN crystal. (b) shows the output power of 626-nm light in dependence of the product of the power of the 1550 nm and 1050 nm laser.

4. Design of the Vacuum Chamber and the ULE Cavity

The present Chapter describes the core project of my master thesis. Indeed, the project targets to build a stable cavity to lock narrow-line laser beams. As discussed in Chap. 3, the cavity will be used for the Er and Dy MOT light. In addition, our experiment also aims at studying Rydberg physics in Er. To excite ground-state atoms to a Rydberg level, we plan to use a two photon excitation, both in the UV. For efficient transfer, the laser light for the excitation needs to have small linewidth. Our cavity is indeed designed for light for the MOTs as well as for the Rydberg excitation light.

In this chapter, first, we discuss the frequency stability of light and give a short overview of the theoretical aspects regarding the cavity. Afterwards, we discuss the cavity requirements and describe the setup of the vacuum chamber for the cavity.

4.1. Frequency-Stability Requirements of the Light

The narrow line magneto optical traps (MOTs) of Er and Dy [33, 61] as well as Rydberg excitation schemes require lasers with a high frequency stability. The stability of a laser is described by the frequency jitter, which can be divided into fast and slow jitter. The division between slow and fast jitter depends on the time scale. The fast jitter is practically not resolvable on the respective timescale and corresponds therefore to the linewidth of the laser light. For the short term stability of the laser the fast jitter is relevant and the width in frequency should be smaller than the linewidth of the transition. For Example, if the linewidth of the laser light for the MOT is broader than the transition linewidth of the atom, it is possible, that the necessary detuning is not guaranteed anymore. In [16] it is shown, that trapping of atoms with a natural linewidth of $\approx 6\,\mathrm{MHz}$ with laser light with a linewidth of 10 MHz leads to a 40 % lower atom number compared to trapping with laser light with a linewidth of 1 MHz.

The linewidths of the cooling transitions for Er and Dy are on the order of 100 kHz and 2 kHz–10 kHz (see Table 2.5 for transition parameters), whereby the linewidths for the lasers for Rydberg excitation are on the low kHz level [57]. For laser cooling the time scale for the fast jitter is in the range of 1 µs to 1 ms, because it is the time scale where the atoms scatter photons.

The slow jitter can in practice be resolved and is therefore referred to as frequency drift and related to the long term stability. In our case, the frequency drift over one day should be such low that the laser remains resonant to the atomic transition. This means, the laser is satisfying stable if the frequency drift over one day is on the order of a few kHz. If the long

term stability of the lasers is unsatisfying, the lasers would have to be readjusted regularly.

One possibility to stabilize the lasers to the desired wavelength is to use a lock to a stable reference cavity. For example the frequency drift of a similar cavity [46] over 7 h was estimated to 2.77 Hz/s leading to a satisfying long term stability. Cavities can also be used to improve the short term stability, as it has been shown in [71], where for a dye laser at 583 nm a linewidth of 45 kHz was obtained and in [53] the linewidth of 200 kHz of a 741 nm external cavity diode laser was reduced to 1 kHz.

4.2. Basic Concepts of Cavity Physics

The aim of this section is to give a brief overview of the theoretical basics of a Fabry-Perot cavity formed by two flat mirrors as illustrated in Fig 4.1. A more detailed description can be found in many textbooks, e. g. [72]. For the derivation of the most important properties for this thesis it is sufficient to concentrate on ray optics describing the incoming wave as

$$E_{\text{inc}} = E_0 e^{i\omega t}, \tag{4.1}$$

with ω being the laser frequency and E_0 the complex amplitude. The electric field picks up

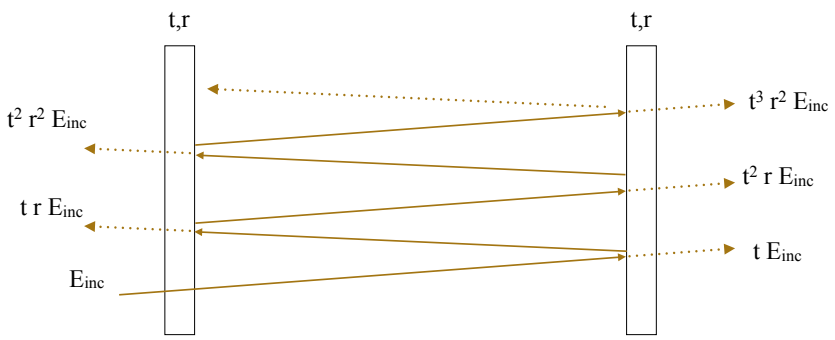

Figure 4.1.: Fabry-Perot cavity and electric field of the incoming beam. t and r label the transmission and reflection coefficient, respectively.

an additional phase while traveling between the mirrors which can be expressed as

$$\Delta\phi = \omega \frac{(n+1)L}{c}, \tag{4.2}$$

where L is the distance between the mirrors of the Fabry-Perot cavity, c is the speed of light and n labels the number of reflections before leaving the cavity. To obtain the total transmitted light field, the partially transmitted fields have to be summed up as

$$E_{\text{trans}} = E_{\text{inc}} \left(t e^{i\Delta\phi} + r^2 t e^{i3\Delta\phi} + r^4 t e^{i5\Delta\phi} + \cdots \right), \tag{4.3}$$

where r is the reflection coefficient and t the transmission coefficient of the mirrors. For the derivation we assume perfect mirrors neglecting any losses. Both coefficients are then connected via

$$r^2 + t^2 = 1. \tag{4.4}$$

Using the geometric series and taking the square of the transmitted electric field leads to the transmitted intensity

$$I_{\text{trans}} = I_{\text{inc}} \frac{T^2}{T^2 + 4R\sin^2(\Delta\phi)}. \tag{4.5}$$

In the same way, the reflected intensity can be written as

$$I_{\text{ref}} = I_{\text{inc}} - I_{\text{trans}} = I_{\text{inc}} \frac{4R\sin^2(\Delta\phi)}{T^2 + 4R\sin^2(\Delta\phi)}, \tag{4.6}$$

where $T = t^2$ is the transmission and $R = r^2$ is the reflectivity. The transmission signal of a cavity is plotted in Fig. 4.2 for two different reflectivity values.

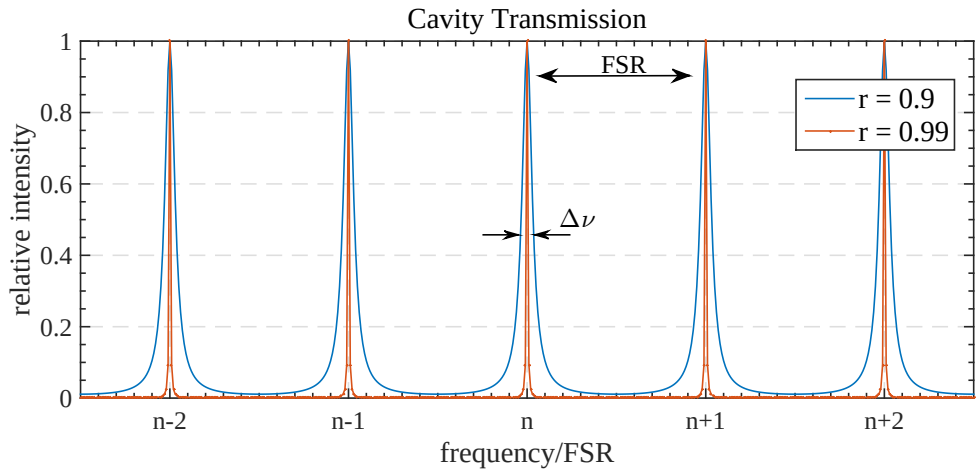

Figure 4.2.: Theoretical plot for the transmission of a cavity. The signal in blue is for a reflectivity of 0.9, whereas the red signal is for a reflectivity of 0.99. The spacing between two cavity-modes can be expressed as $\nu_n - \nu_{n-1} = \frac{c}{2L}$ and is equal to the FSR.

Important parameters of a cavity are the free spectral range (FSR) and the full width at half maximium (FWHM). The FSR

$$\text{FSR} = \frac{c}{2L} \tag{4.7}$$

describes the distance in frequency between two neighboring longitudinal modes. The full width at half maximum (FWHM) corresponds to the linewidth $\Delta\nu$ of the transmission peaks. Assuming low losses in the cavity it can be calculated as

$$\Delta\nu = \frac{FSR}{\pi} \arccos\left[1 - \frac{(1-R)^2}{2R}\right]. \tag{4.8}$$

An additional important parameter to characterize a cavity is the finesse $\mathcal{F}$, which simply is the ratio between the FSR and the FWHM:

$$\mathcal{F} = \frac{\text{FSR}}{\text{FWHM}}. \tag{4.9}$$

For the special case of low losses and high reflectivity as in our case, the finesse can be expressed as

$$\mathcal{F} = \frac{\pi\sqrt{R}}{1-R}. \tag{4.10}$$

The linewidth of the resonance can be interpreted as a decay of optical energy due to resonator losses and is therefore related to the average photon lifetime, τ_{P}, in the resonator:

$$\tau_{\mathrm{P}} = \frac{1}{2\pi\Delta\nu}, \tag{4.11}$$

where $\Delta\nu$ is the linewidth of the cavity. If we consider wave optics instead of beam optics, beside the longitudinal modes, only differing in frequency, also higher transversal modes exists, which differ in their intensity pattern and can be different in frequency. In wave optics the solution of a resonator is described by the Hermite-Gauss functions, written as TME_{nm} with the intensity distribution

$$I(x,y,z) = I_0\left[H_n\left(\frac{\sqrt{2}}{w(z)}\right)\exp\left(\frac{-x^2}{w(z)^2}\right)\right]^2\left[H_m\left(\frac{\sqrt{2}}{w(z)}\right)\exp\left(\frac{-y^2}{w(z)^2}\right)\right]^2,$$

where H_k is the kth Hermite polynomial, $w(z)$ is the waist (see below), and n and m are positive integers. In Figure 4.3 the intensity distribution in the x-y plane for different TME modes is plotted. The TME_{00} is called the Gaussian mode and is the only mode which has the same resonance conditions as obtained with ray optics, whereas higher TME modes have different resonance conditions depending on the cavity geometry. Those higher cavity modes can have a negative effect on the locking if they are to close in frequency to the TME_{00} mode and therefore influence the PDH-error signal (see App. A.1). For the geometrical case in which one cavity mirror is flat whereas the other mirror is spherical, the frequency difference between two TME_{nm} modes is given by [28]

$$\delta\nu = \frac{c}{2L}\frac{(n+m+1)}{\pi}\arccos\left(\sqrt{1-\frac{L}{\rho}}\right), \tag{4.12}$$

where L is the length of the cavity and ρ is the radius of the spherical mirror. For our cavity parameters of $L = 0.15\,\mathrm{m}$ and $\rho = -500\,\mathrm{mm}$ this leads to $\delta\nu \approx 210\,\mathrm{MHz}$. Since we will lock the laser to the TME_{00} mode it will be important, that the adjacent cavity modes are far enough away from the sidebands for the generation of the PDH error signal (see Sec A.1). Otherwise, the latter could be disturbed by the close lying cavity modes. Since our FSR equals approximately 1 GHz, cavity modes with $m + n \geq 5$ have to be sufficiently suppressed. This is easily possible with a good cavity coupling.

For the description of the coupling to a cavity the laser beam has to be treated as a Gaussian beam, which can be characterized by the q-parameter

$$\frac{1}{q} = \frac{1}{R(z)} - \frac{i\lambda}{\pi W(z)^2}, \tag{4.13}$$

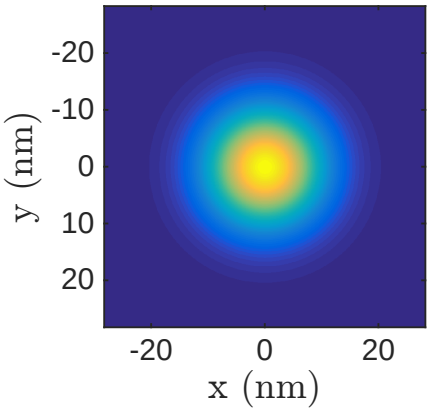

(a) TME_{00}

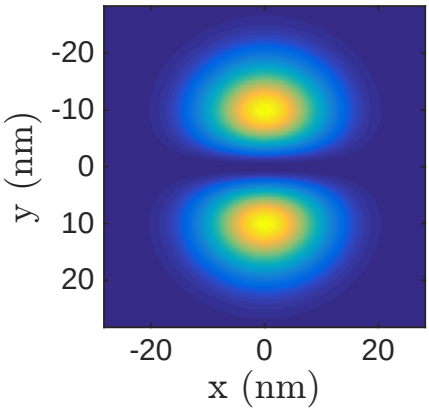

(b) TME_{01}

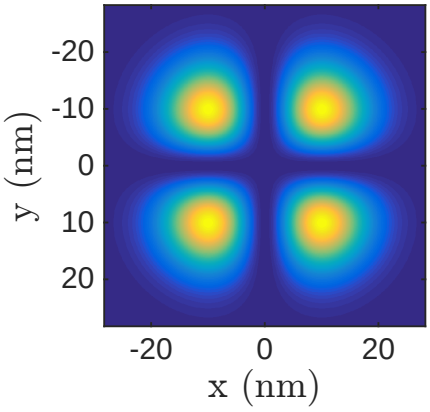

(c) TME_{11}

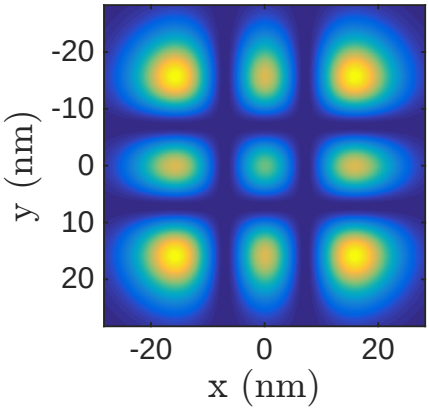

(d) TME_{22}

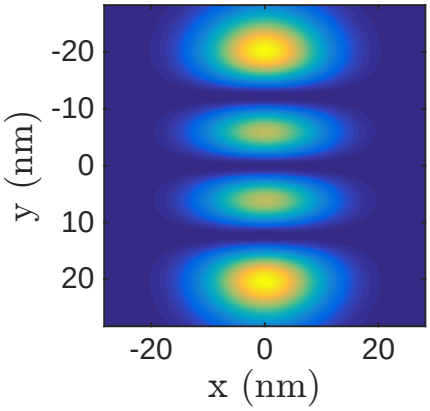

(e) TME_{04}

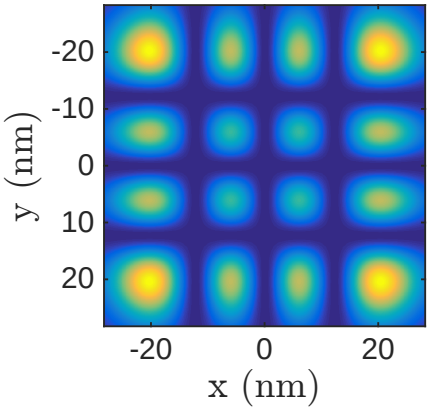

(f) TME_{33}

Figure 4.3.: The intensity distribution of different transversal cavity modes is plotted.

containing the curvature

$$R(z) = z\left[1 + \left(\frac{z_0}{z}\right)^2\right] \tag{4.14}$$

and the waist of the beam

$$w(z) = w_0\sqrt{1 + \left(\frac{z}{z_0}\right)^2}, \tag{4.15}$$

where λ is the wavelength, z is the expansion direction of the beam, w_0 is the minimum waist in the focus of the beam and z_0 is the position where the curvature of the beam is maximal, respectively. To couple a laser beam to a cavity, it is important that the beam travels exactly along the axis of the mirrors and that the curvature of the wavefront of the beam equals the radius of the mirrors. Since we use one planar mirror and one mirror with a radius of $\rho = -500\,\text{mm}$ the beam has to be focused on the planar mirror and by combining Eq. 4.14 and Eq 4.15 one obtains that the beam waist in the focus W_0 has to be

$$w_0 = \frac{L\lambda}{\pi}\sqrt{\frac{\rho - L}{L}}. \tag{4.16}$$

By inserting our cavity parameters, $L = 15\,\text{cm}$ and $\rho = -500\,\text{mm}$, we obtain for example a beam waist of $W_0 = 214\,\mu\text{m}$ for $\lambda = 626\,\text{nm}$. In Sec. 5.1 the optical setup for the coupling to the cavity is explained.

4.3. Cavity Requirements

Reflectivity Requirements

An important requirement for our cavity is the possibility to frequency stabilize light at several wavelengths. On the one hand, we want to stabilize the light for the MOT of Er and Dy and, on the other hand, we want to lock the light for Rydberg excitation. Table 4.1 gives a list of all required wavelengths or wavelength ranges. The 583-nm transition for Er and the 626-nm transition for Dy are used for the MOTs, respectively. The 631-nm transition and the 741-nm transition are even narrower transitions, that can be used for additional cooling [56] or state preparation. The exact wavelengths for the Rydberg excitations are not known yet, as many different excitation schemes are possible. For this reason a broad wavelength range was chosen. Furthermore, the largest isotope shift for Er and Dy is about 1 GHz (see Fig. 2.2), that suggests to use a cavity with $L = 15\,\text{cm}$, which leads to a FSR of 1 GHz. This makes the switching between the isotopes easier because the laser can be locked to the next cavity resonance (see Sec. 5.4).

The multiwavelenght operation requires to employ cavity mirrors with high reflectivity over a wide frequency range. The reflectivity of a mirror is related to the Bragg diffraction condition. For high reflection coatings a periodic layer structure composed of different materials enhances the reflectivity of the mirror because they lead the reflected beams to interfere constructively. By varying the thickness and the composition of the layers the characteristics of the mirror can be manipulated and high reflective and anti-reflective

Table 4.1.: List of all wavelengths we want to stabilize.

Erbium		Dysprosium	
Wavelength (nm)	Linewidth (kHz)	Wavelength (nm)	Linewidth (kHz)
583	190	626	136
631	28	741	1.78
380–450	few kHz	–	–

regions can be created. Due to technical limitations, it is hard to produce one highly reflective (> 99.96 %) mirror coating for all our required wavelengths. Therefore, we use two sets of cavity mirrors of different mirror coatings. The mirrors for one cavity are coated[1] for the 583 nm, 626 nm, 631 nm and 741 nm transitions, while the mirrors for the other cavity are coated for all wavelengths in the range from 380 nm–450 nm. Figure 4.4 shows the theoretical transmission curves for the coatings, provided by Lens-Optics. Table 4.2 gives the theoretical reflectivity and the related values for $\mathcal{F}$. For each wavelength the finesse for the theoretically best and worst case are calculated by Eq. 4.10. In comparison to other experiments, e. g. [4, 74] our cavities will have a relatively low finesse. Nevertheless, this is sufficient since the light of the lasers does not have to be narrower than 1 kHz.

Table 4.2.: Reflectivity and rough estimation of the expected finesse for the different wavelengths. For the calculations the theoretical curves from Fig. 4.4 and Eq. 4.10 are used. The 410 nm line is one possible transition for the Rydberg excitation.

	$R(\%)$		$\mathcal{F}$	
wavelength (nm)	min	max	min	max
583	99.91	99.96	4500	7800
626 & 631	99.95	99.98	6300	20 000
741	99.95	99.98	6300	15 700
410	99.92	99.98	4000	15 700

Cavity Stability

To improve the stability of the length of the cavity and therefore of the resonance frequency a spacer out of ultra low expansion glass[2] (ULE) between the cavity mirrors is placed. Although we have two cavities we use only one ULE spacer. This design is already implemented successfully in a running experiment [74]. The special property of ULE is that the linear coefficient of thermal expansion (CTE) has a zero-crossing point near room temperature providing a CTE[3] below $2 \times 10^{-9}\,\frac{1}{\mathrm{K}}$ within one degree around this point and

[1]The mirrors are manufactured and coated by Lens-Optics GmbH.
[2]From Hellma-Optics, ULE premium grade.
[3]Corning, manufacturer for glass and ceramic.

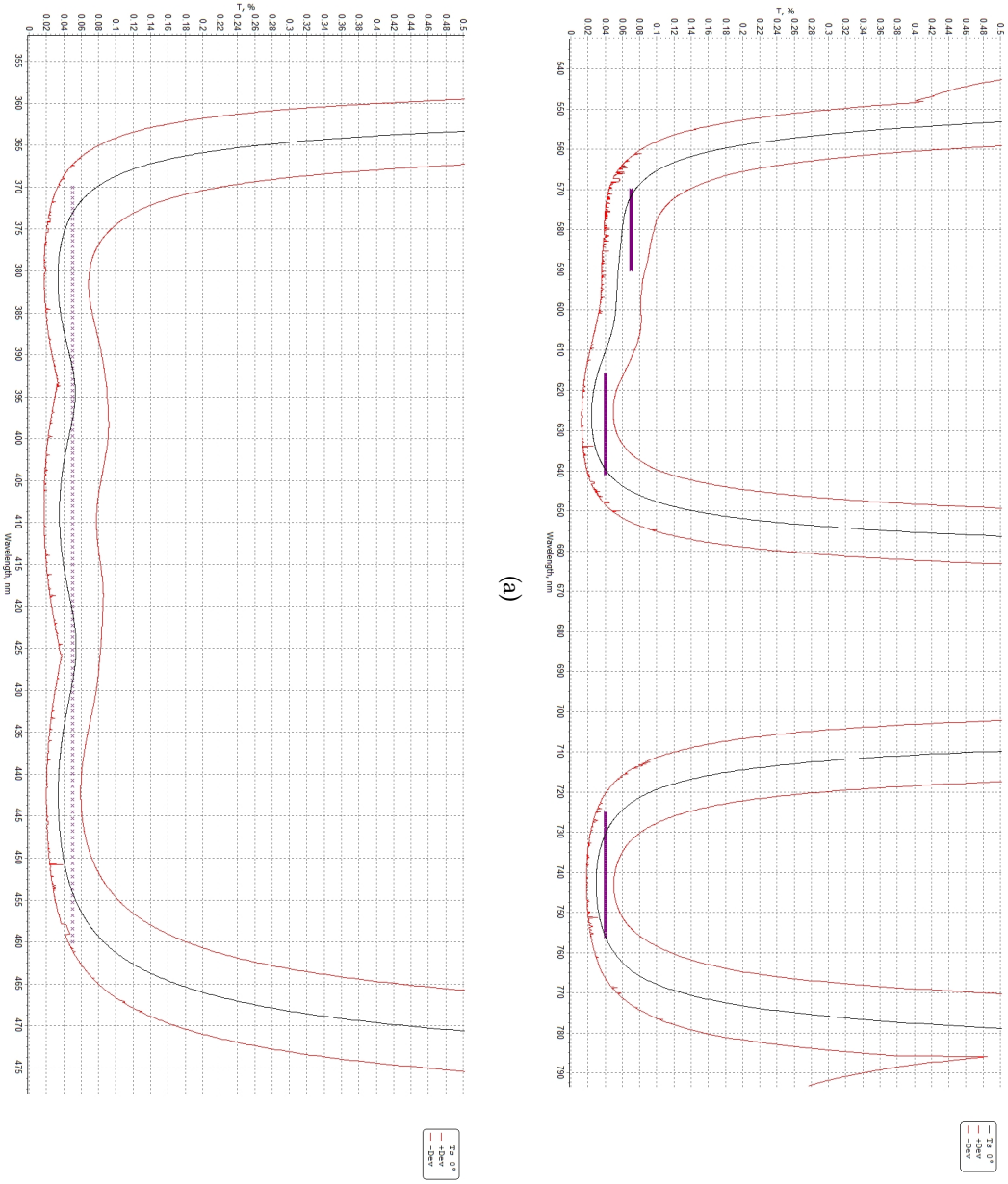

Figure 4.4.: The different coatings, used for the two sets of cavity mirrors are shown. (a) Coating for the stabilization of the 583 nm, 626 nm, 631 nm and 741 nm lasers. (b) Coating for lasers in the range of 380 nm-450 nm used for Rydberg excitation. Graphs are provided by Lens-Optics.

therefore high stability against length fluctuations. Unfortunately the exact temperature for the zero-crossing can be different for each production series and is therefore specified only to be between 0 °C and 30 °C.

The cavity mirrors are optically contacted to the ULE spacer, which is manufactured by Hellma-Optics. Also the optical contacting of the mirrors to the ULE spacer was done by Hellma-Optics. Before choosing the mirror substrate we considered several aspects: Combining different production series of ULE or even different materials as ULE and Fused Silica (when using mirrors out of Fused Silica) could shift the zero-crossing temperature out of the specified region. Fused Silica has a CTE of about $5 \times 10^{-7}\,\frac{1}{\mathrm{K}}$ being roughly independent of temperature. Due to the fact, that the CTE of Fused Silica is positive and the CTE of ULE gets negative for temperatures below the zero-crossing, the minimum CTE of the ULE spacer together with the Fused Silica mirrors gets shifted to lower temperatures. This makes the temperature regulation more elaborate. Fused Silica mirrors have the advantage that they can reduce the fractional instability from thermal noise compared to ULE mirrors [51]. Nevertheless, for our purpose of a relatively low finesse cavity the stability of ULE mirrors does not limit us.

Beside the reflectivity of the mirrors, it is important that the mirror substrate does not absorb to much light. The transmission of ULE at our desired wavelengths is sufficiently high (see gray area in Fig. 4.5) and therefore, we decided to use cavity mirrors made out of ULE glass.

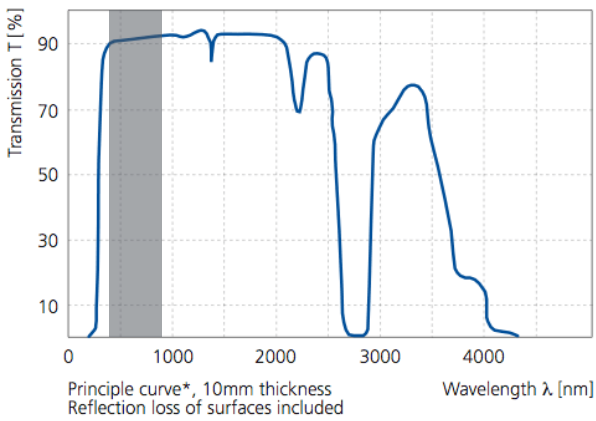

Figure 4.5.: Transmission curve of ULE glass. The gray area indicates approximately our wavelength range. Graphic taken from Präzisions Glas & Optik GmbH. December, 2016.

Regarding the long term frequency stability, we aim to stabilize the lasers in such a way that they do not drift more than the linewidth of the transition over a long enough time period, ideally one day. In our case the smallest linewidth is 1.78 kHz for the 741 nm transition of Dy. Thus, the cavity should have a long term stability on the order of $\Delta\nu \lesssim 1\,\mathrm{kHz}$. The resonance frequency of a cavity depends on the optical length nL (see Eq. 4.7) and therefore the relative frequency deviation $\Delta\nu$ of the cavity resonance can be expressed

by the relative length change $\Delta L/L$ and the relative change of the refraction index $\Delta n/n$:

$$\frac{\Delta \nu}{\nu} = \sqrt{\left(\frac{\Delta L}{L}\right)^2 + \left(\frac{\Delta n}{n}\right)^2}. \tag{4.17}$$

For our requirement of $\Delta\nu \lesssim 1$ kHz we need to reach a relative stability of

$$\frac{\Delta \nu}{\nu} \leq O(10^{-12}) \tag{4.18}$$

First, we look at the influence of change in the refraction index: by using the Clausius-Mossotti Equation [52]

$$\frac{n^2 - 1}{n^2 + 2} = \frac{N\alpha}{3} \tag{4.19}$$

we can make a connection between the refraction index n and both, the temperature T and the pressure p. Since the refraction index for air is on the order of $1 + O\left(10^{-4}\right)$ and for vacuum even much lower, we can use the taylor expansion for Eq. 4.19, expanding n^2 around 1, leading to

$$\frac{n^2 - 1}{n^2 + 2} = \frac{n^2 - 1}{3}.$$

Furthermore, inserting the molar refractivity A, which is a measure for the total polarizability of a mole, one obtains for the refractive index

$$n = \sqrt{1 + \frac{3Ap}{RT}}, \tag{4.20}$$

where R is the universal gas constant. For the relative change of the refractive index one obtains

$$\frac{\Delta n}{n} = \frac{n-1}{n}\sqrt{\left(\frac{\Delta p}{p}\right)^2 + \left(\frac{\Delta T}{T^2}\right)^2}. \tag{4.21}$$

Calculating the refractive index for a temperature and pressure comparable with our system, i. e. 20 °C and 10^{-8} mbar, leads to a relative change of refraction index on the order of 10^{-15}. Obviously, the change in temperature and pressure should be moderate for this estimation. Therefore, in the following we can neglect the influence of the refraction index on the stability of the cavity resonance and focus on the length stability.

The length change of the the ULE spacer can be described as

$$\Delta L = \alpha(T) \cdot L \cdot \Delta T, \tag{4.22}$$

where α is the coefficient of thermal expansion (CTE) and L the length of the cavity. A special property of ULE is that the CTE has a so called zero-crossing around room temperature. In Figure 4.6 the CTE is plotted between 0 °C and 44 °C with the zero-crossing temperature T_C at 20 °C.

This shows, that having a temperature stability of 10 °C around T_C gives a CTE on the order of 1.5×10^{-8} /K. Assuming the CTE to be linear around T_C gives a maximal CTE

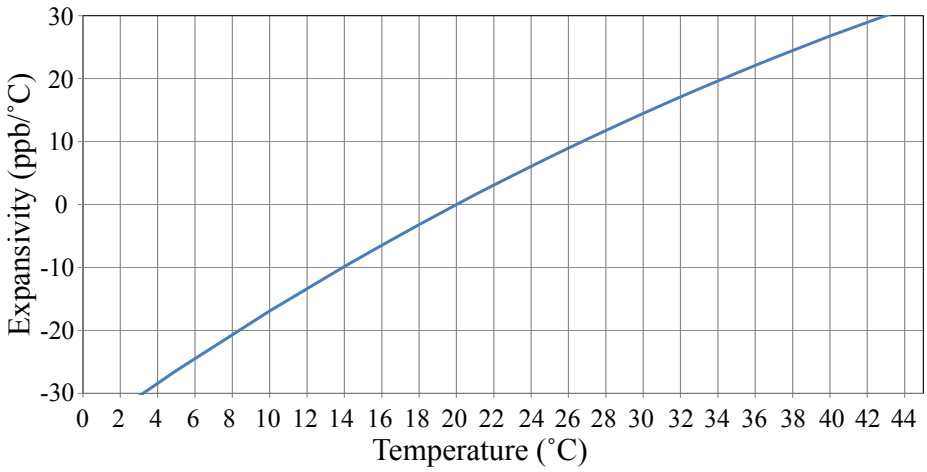

Figure 4.6.: This Figure shows the zero-crossing of the instantaneous CTE for ULE at an example temperature of 20 °C. Figure is taken from Corning, Product Information Sheet 7973 July, 2015

on the order of 1.5×10^{-11} /K for a temperature stability of 10 mK. Therefore, having a temperature stability on the order of 10 mK gives a relative length stability on the order of

$$\frac{\Delta L}{L} = O(10^{-11}) \cdot O(10^{-2}) = O(10^{-13}). \tag{4.23}$$

This is easily sufficient for our application (see Eq. 4.17).

Another effect to take into account is the length change due to vibrations. The effect of vibrations to relative length changes can be calculated by [15]

$$\frac{\Delta L}{L} = \frac{\rho g h}{2E}\sigma, \tag{4.24}$$

where $\rho = 2.21\,\mathrm{g/cm^3}$ is the mass density, g is the acceleration, h the hight of the ULE spacer, $E = 67.6\,\mathrm{GPa}$ the elastic modulus and $\sigma = 0.17$ the Poisson's ratio[4]. This results in a sensitivity of the relative frequency stability to vertical accelerations of $2.8 \times 10^{-10}\,/\mathrm{ms^{-2}}$. Vibrations in the horizontal direction should have a much lower influence because of the symmetric mounting [45]. For the lab typical values for the vertical accelerations are on the order of $3\,\mathrm{mms^{-2}}$, which leads to a minimum stability on the order of 10^{-13}. Therefore, we can assume that the vibrational stability of the cavity is sufficient for this purpose.

Another point to be noted is the drift of the frequency caused by relaxation effects of the cavity due to aging of the ULE spacer. In [26] the long term drifts of the cavity is fitted by two exponential decay functions superimposed on a linear function with a slope of 13(2) mHz/s. The two time constants of the decay functions describing the long term drifts are 32(7) days and 260(80) days. The positive sign of the linear slope indicates that the cavity length decreases and is therefore an indication for aging of the material of the spacer.

[4]Values for the material specific parameters can be found into data sheet of ULE® Corning Code 7972.

4.4. Mechanical and Electrical Design of the Vacuum Chamber

The design for the housing of the cavity was inspired by the master theses of Alexander Ritzler and Maximilian Segl [71, 74].

Vacuum Chamber Design

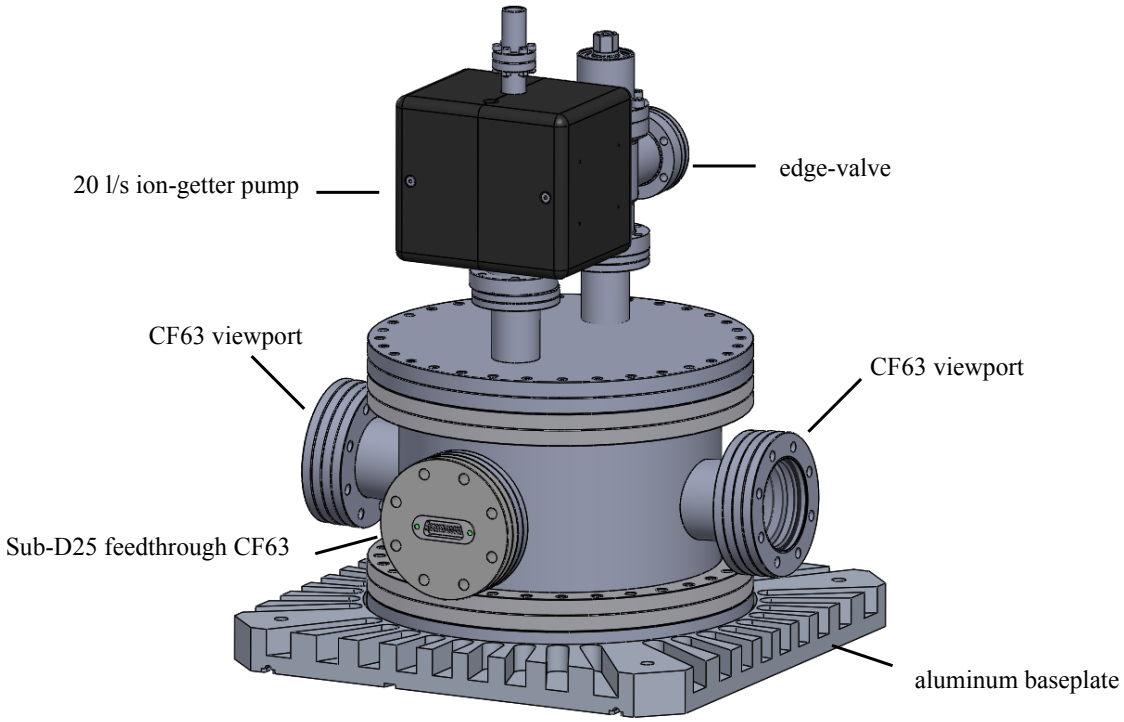

Figure 4.7.: Drawing of the vacuum chamber which houses the ULE cavity. The baseplate has a size of 400 mm × 400 mm. The height of the chamber is about 300 mm. The vacuum chamber is made of stainless steel, whereas all interior parts as well as the baseplate are made of aluminum. All vacuum parts are of the CF type. For optical access two CF63 viewports are implemented. A feedthrough with a Sub-D25 connector is used for the connection of the NTCs and the Peltier elements and a 20 l/s ion-getter pump is installed for pumping.

Fig. 4.7 shows the complete design. The vacuum chamber has a cylindrical shape and is closed by two CF250[5] flanges. The vacuum chamber has two CF63 viewports for optical access and an electrical feedthrough with a Sub-D25 connector for electrical connections. The viewports are attached at an angle of 3° to avoid disturbing reflections. We use an

[5] ConFlat (CF) is a special flange design which uses a knife edge in combination with a copper gasket as a sealing technique. The number stands for the DN type (DN250 in this case) and indicates the diameter of the system.

all-metal angled valve for the initial pump down with a turbo pump and a 20 l/s ion-pump[6] to hold the pressure afterwards at the low 10^{-8} mbar level.

The inner part of the vacuum chamber is formed by two consecutive shieldings as shown in Fig. 4.8 which shows a cut through the vacuum chamber. The ULE spacer forming the cavity together with the mirrors is sitting on a V-shaped block supported by 4 rings made of Viton, intended to reduce vibrational distortions. The location of the Viton rings is determined by the so called Airy points, $a/L \approx 0.2113$, at which the bending of a held bar is minimized and the facets of the end of the bar are parallel to each other. L relates to the length of the ULE spacer and a is the distance between the Airy point and the nearer end of the bar.

We temperature stabilize the outer shielding via six Peltier elements[7], whereas the inner shielding is sitting on Teflon spacers to ensure heat is transported mainly by radiation from outer to inner shielding. The reduced heat transport results in a long thermalization time constant, which corresponds to the principle of a low-pass, i. e. fast temperature changes below the characteristic time constant are suppressed providing a higher stability against temperature fluctuations. In Figure 4.9 the temperature of the aluminum block that holds the cavity is plotted against time. The temperature of the outer shielding was set from 32.5 °C to 30.5 °C. With an exponential fit the thermalization constant was determined to 9.6(7) h. The dip around 25 h was probably caused by a temperature failure of the air conditioning system of the lab and is an artifact deriving from the measurement method. The temperature in the lab increased by a few degree and this influenced the values of the resistors used for the voltage dividers to read out the temperature. The inner part of the cavity should not have experienced the temperature change.

Due to possible flatness imperfections of the Peltier elements, we use tin sheets with a thickness of 100 µm to compensate unevenness and therefore to increase the heat conductivity. We glue coated windows into the holes of both shieldings to have optical access to the cavities. Further, this should give additional shielding against thermal noise. All metallic inner parts of the vacuum chamber are made of aluminum for a better heat conductivity. To remove the heat produced by the Peltier elements, the vacuum chamber sits on a large heat sink. To reduce the temperature difference for the Pelter elements that stabilize the outer shielding six Peltier elements are used to cool the lower flange of the cavity. At the same time this Peltier elements temperature stabilize the vacuum chamber. At the time the housing for the cavity was built the CF250 flanges and the tube were available only out of stainless steal and therefore the vacuum chamber itself has a 5 times less thermal conductance than aluminum. Therefore, a copper plate sitting on the Peltier elements was included to increase the contact area from the Peltier elements on the baseplate to the lower flange of the vacuum. For future cavity projects aluminum CF vacuum components are recommended. Figure 4.10 shows temperature simulations[8] for both cases, with and without the additional copper plate. If we have to go to low temperatures (CTE of ULE is specified between 0 °C and 30 °C) the heat sink is not big enough to remove the heat

[6] Agilent Vaclon Plus 20.
[7] Multicomb MCPE-241-10-13 Peltier Cooler, 71.8 W.
[8] SolidWorks 2014.

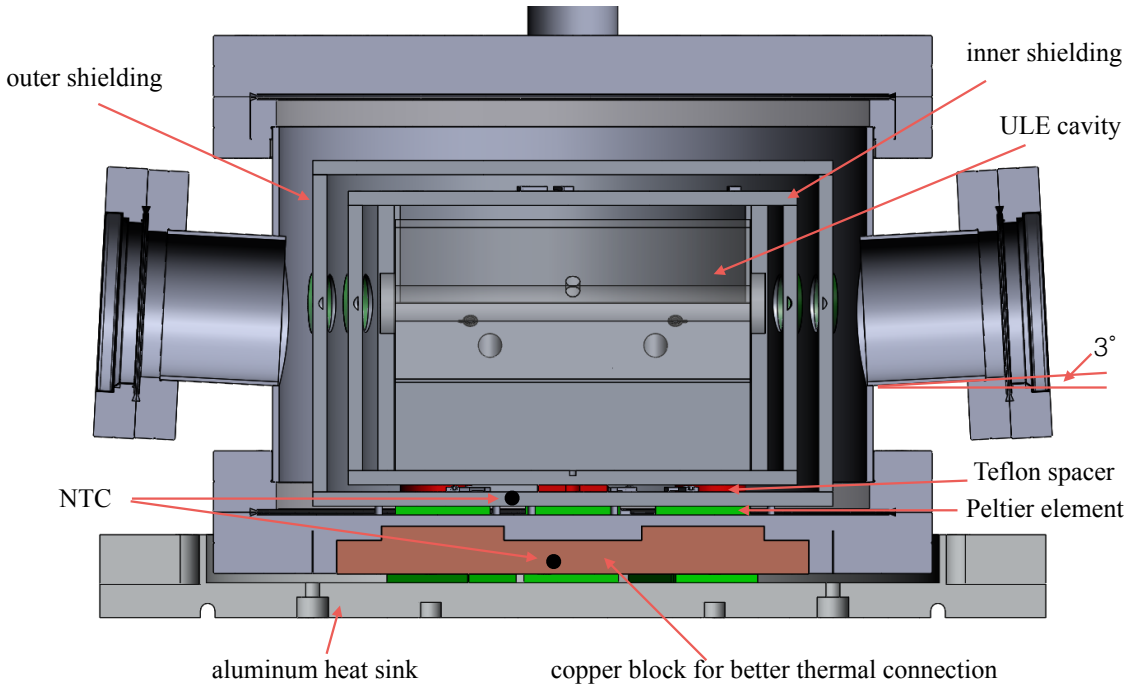

(a) Cut through the vacuum chamber. The cavity spacer is seen from the side.

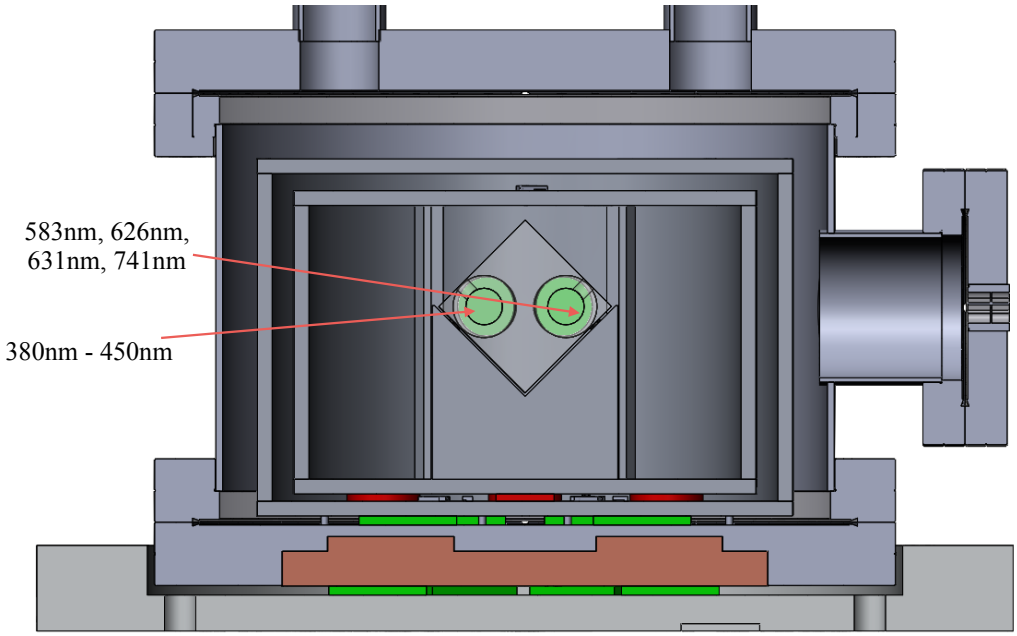

(b) Cut through the vacuum chamber. The cavity spacer is seen from the front.

Figure 4.8.: Vertical cuts through the vacuum chamber. In (a) the cavity spacer is seen from the side. The Peltier elements are illustrated in green and the Teflon spacer in red. The position of the NTCs which are used for temperature regulation are marked by a black dot. Many other NTCs are distributed over the vacuum chamber. In (b) the cavity spacer is seen from the front and the two cavities with the different coatings are labeled.

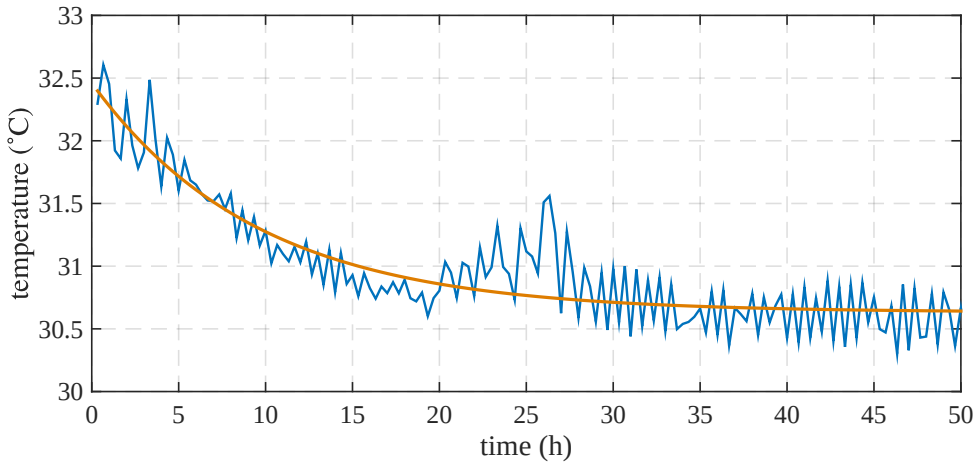

Figure 4.9.: Record of the temperature of the aluminum holder of the cavity. Note that the dip at 25 h was caused by a failure of the air conditioning system of the lab. The data points are fitted with an exponential function $y = A + B\exp(t/\tau)$, where t denotes the time. The time constant τ was determined to 9.6(7) h.

produced by the Peltier elements. The heat transport of the vacuum chamber to the outer shielding by thermal radiation can be calculated by

$$\dot{Q} = \epsilon\sigma\left(A_{\text{chamber}}T^4_{\text{chamber}} - A_{\text{shielding}}T^4_{\text{shielding}}\right) \tag{4.25}$$

where ϵ is the emissivity of the material, σ is the Stefan-Boltzmann constant, A the surface area and T is the temperature. By assuming 0.2 for ϵ and a temperature difference of 10 °C leads to a thermal radiation of 15 W from the vacuum chamber to the shielding. This means that 15 W of the cooling power of the Peltier elements are used to make up the heating from the vacuum chamber walls.

The temperature difference between the shielding and the vacuum chamber should be as low as possible and therefore a water cooling system is implemented in the baseplate. The water cooling system consists of a copper tube that was pressed into a channel on the bottom of the baseplate. Testing the reachable temperature with the water cooling showed that this simple solution is satisfying for our purpose.

Temperature Control

Thermistors[9] (NTCs) for the temperature regulation and monitoring are allocated at different positions in the vacuum chamber. The monitoring of the NTCs is done with an Arduino system[10]. The two NTCs planned for the temperature regulation are sitting on the copper plate below the lower flange of the vacuum chamber and on the outer shielding (see Fig. 4.8). The temperatures are stabilized with a simple analog PID controller. In the Appendix A.3,

[9] Epcos B57541G1, 10 kΩ at 25 °C.
[10] Arduino Due.

the measurement bridge, which generates the error signal, and the PID drawing are shown, respectively. For the connection of the electronic components inside the vacuum chamber we use wires insulated with Kapton™[11]. The advantage of using Kapton™is that it has a low outgassing rate compared to standard isolation materials. The wires are soldered to the Sub-D connector at the feedthrough and the electronic components and to isolate the solder joints we use tape out of Kapton™.

[11]Twisted pair wire, 311-KAPM-060-PAIR1-20M.

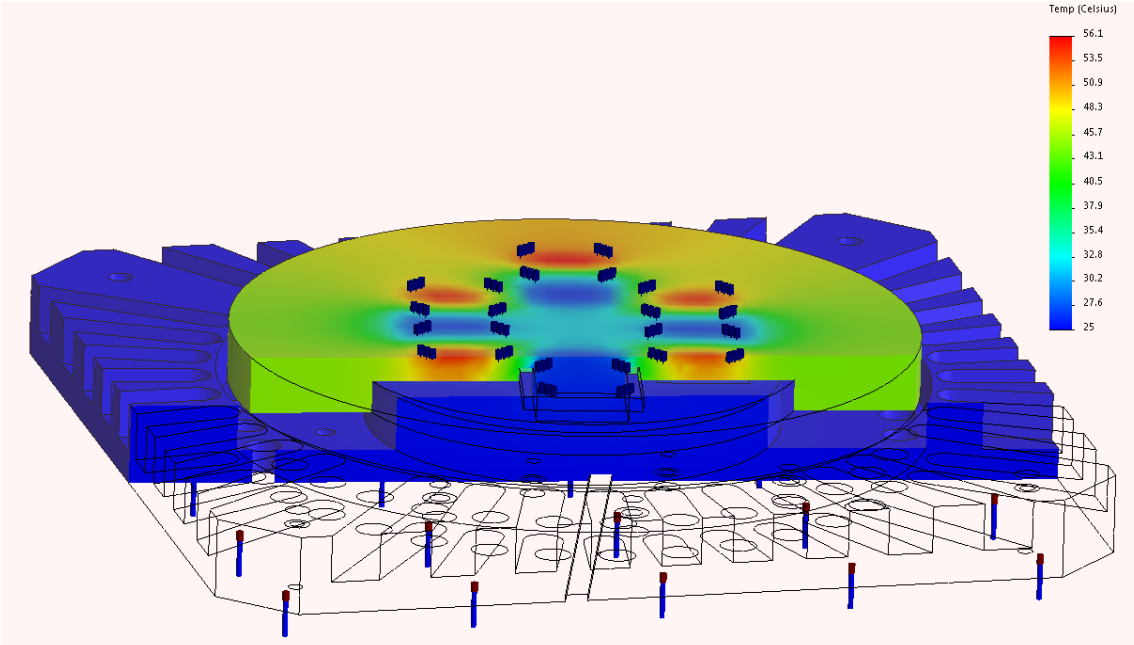

(a) Heat sink and lower flange without the additional copper plate.

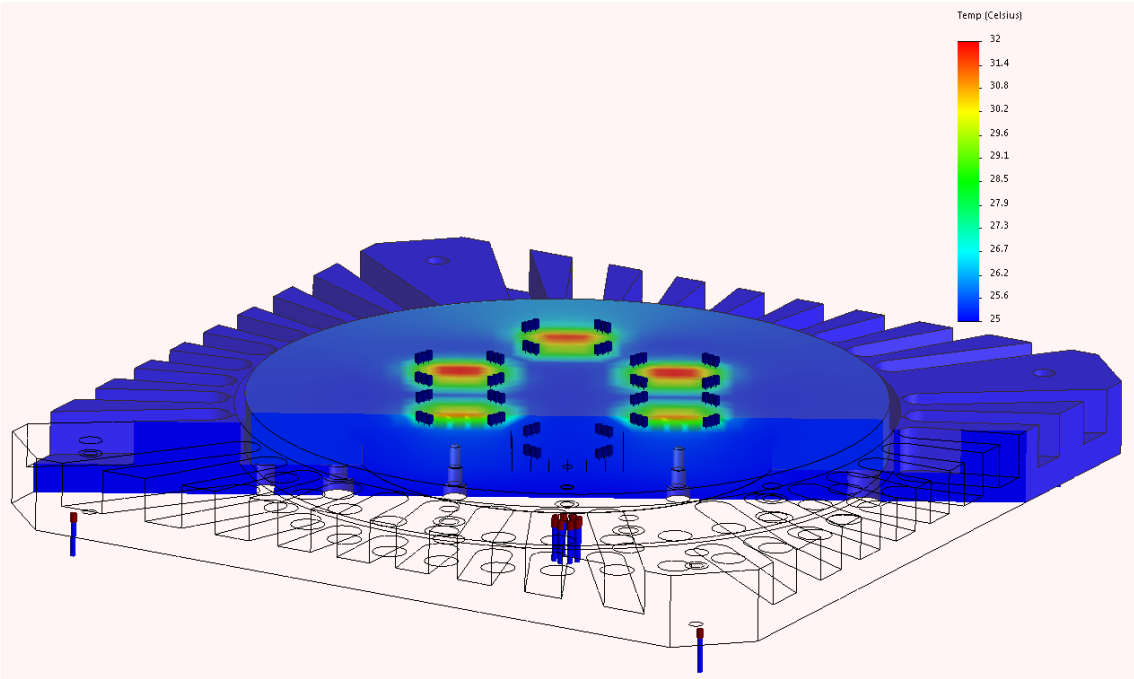

(b) Heat sink and lower flange with the additional copper plate.

Figure 4.10.: Temperature simulations, done with SolidWorks 2014, for the two types of base plates we tested. It is assumed, that six Peltier elements are sitting on the lower flange, which are heating with a total power of 100 W. Below the lower flange 6 Peltier elements should remove the heat and transport it to the aluminium heat sink. In (a) no additional copper plate was placed and the heat can not be removed satisfyingly. In (b) the copper plate solves the issue of the heat transport.

5. Experimental Part

In this Chapter, we present the main experimental results concerning the characterization of the cavity performance, i. e. the zero-crossing temperature of the CTE of the ULE glass, the finesse, and the free spectral range of the cavity.

5.1. Optical Setup for the Coupling of the Lasers to the Cavity

For a good mode matching between the light and the cavity, it is important to fulfill the condition from Eq. 4.16

$$w_0 = \frac{L\lambda}{\pi}\sqrt{\frac{\rho - L}{L}}, \tag{5.1}$$

where λ is the wavelength, L is the length of the cavity and ρ is the radius of the curved mirror. Table 5.1 gives the theoretically calculated values for the necessary beam waists on the planar mirror w_{planar} of the cavity. These beam waists can be achieved, by putting a

Table 5.1.: Calculated beam waists on the planar mirror of the cavity w_{planar} for the light of 583 nm, 626 nm, 631 nm, and 741 nm. The cavity length is $L = 15$ cm and the radius of the curved mirror is $\rho = 500$ mm.

λ (nm)	w_{planar} (mm)
583	0.206
626	0.2137
631	0.2145
741	0.2325

lens in front of the cavity to focus the beam. Figure 5.1 shows the lens in front of the cavity, forming a lens system with the curved mirror of the cavity. We assume the curved mirror with $\rho = -500$ mm being a lens with $f = \frac{\rho}{n-1} = -1000$ mm, because the refractive index n of ULE is approximately 1.5[1].

We calculate the beam waist on the planar mirror of the cavity in dependence of the waist of the incoming collimated beam via ray transfer matrix analysis. For a lens with a focal length of 500 mm the incoming beam should have a beam waist of ≈ 0.5 mm. Our fiber output coupler[2] is chosen such that the beam diameter is already on the right order

[1]Corning, manufacturer for glass and ceramic.
[2]Thorlabs, SM1Z in combination with CP11/M.

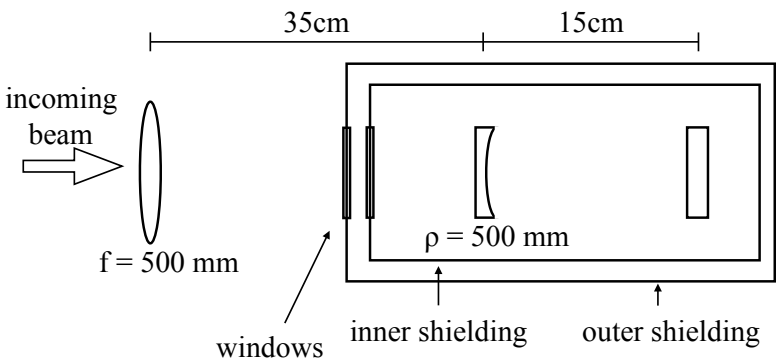

Figure 5.1.: Schematic presentation for the coupling to the cavity. The laser beam gets focused through the 500 mm lens into the cavity, whereby the curved mirror can be assumed as a lens with focal length −1000 mm.

and for fine adjustment the position of the lens and therefore the beam size can be tuned. Figure 5.2 shows the optical setup for coupling of the 626-nm light and the 583-nm light into the cavity.

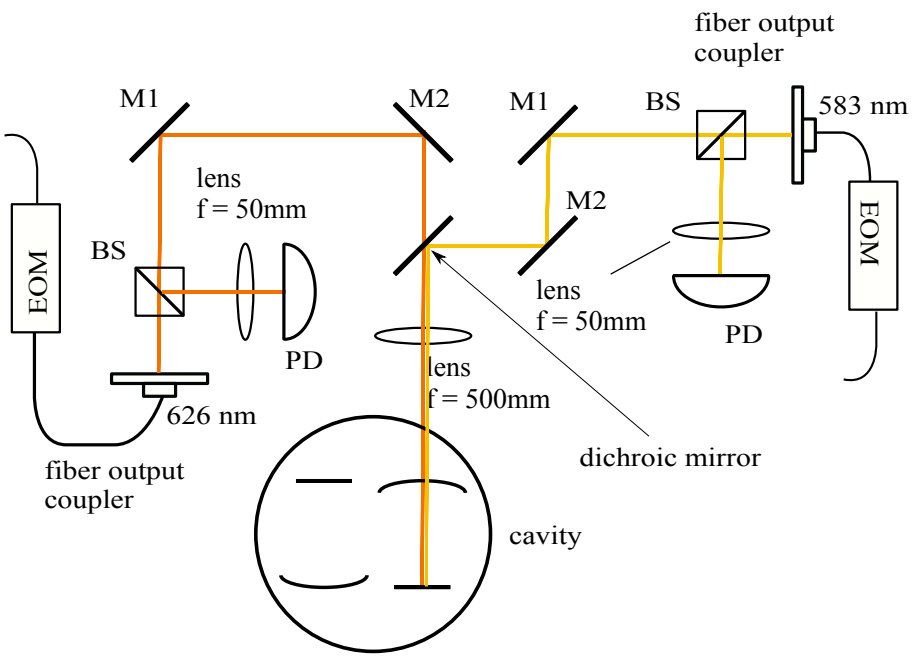

Figure 5.2.: Optical setup to couple the light of 583 nm and 626 nm into the cavity. After the fiber output coupler the light gets coupled into the cavity with the mirrors M1 and M2. A dichroic mirror overlaps the 583-nm light (yellow) with the 626-nm light (orange). The light is then focused onto the planar mirror. The reflected light is picked up with a beam splitter (BS) and detected with a photodiode (PD).

We guide the laser beams via the fiber-coupled EOM to a breadboard, where the setup to couple the light into the cavity is placed. A dichroic mirror[3] overlaps the 583-nm and the 626-nm light and we couple the light with the mirrors labeled by M1 and M2 into the cavity. We focus both beams into the cavity through the same lens. After the output coupler a 50-50 beam splitter splits the reflected signal of the cavity for the generation of the PDH error signal. One reason to use a 50-50 beam splitter instead of a polarizing beam splitter in combination with a $\lambda/4$ in front of the cavity, as in [71], is that we want to add the 631-nm light and the 741-nm light in the future and there is no standard dichroic mirror available to overlap the 626-nm and the 631-nm light. Therefore, the light has to be overlapped with a PBS and with a $\lambda/4$ in front of the cavity the separation of the reflected signal is not possible.

5.2. Modulation-Transfer Spectroscopy

To achieve a stable operation of the cavity, one first needs to determine the value of the temperature at which the cavity, i. e. ULE mirrors and ULE spacer, exhibits a minimal thermal expansion. To determine this temperature, we measure the resonance frequency of the cavity because a change of the cavity length results in a change of the free spectral range (FSR) (see Sec. 5.3). We measure the relative length of the cavity by measuring changes in the resonance frequency with respect to the frequency of a reference signal. At the time when this measurement was done we had only the laser of 626 nm for Dy available and therefore we used this laser for the measurement. Since Dy has a high melting point (see Sec. 2.1), one would need a high temperature oven to create neutral hot Dy vapor. Instead, we use a hollow cathode lamp (HCL) to produce the atomic sample. The HCL is a glass cell with a cathode and an anode inside. The cathode is coated with the desired element, in our case with dysprosium. The glass cell is filled with argon, which serves as a buffer gas and gets ionized in an electric discharge process when a high voltage is applied between cathode and anode. The applied voltage during the spectroscopy was 117.1 V with a current of 14.9 mA. After the ionization the Ar+ ions are accelerated and impact into the cathode. In this way the Ar+ ions sputter the dysprosium away in form of atomic vapor by depositing their kinetic energy. The hot atomic vapor exhibits a too large Doppler broadening to be used as a reference. In order to avoid this we use a Doppler-free spectroscopy technique, namely the modulation-transfer spectroscopy. This method employ two counter-propagating laser beams to interrogate the atoms. One beam, known as pump beam, has a higher intensity with respect to the weak probe beam. Figure 5.3 shows the setup for the generation of the MTS signal and Appendix A.2 outlines the generation of the spectroscopy signal.

We guide the laser light with a fiber from the setup of the 626-nm laser to the spectroscopy setup. After the fiber output coupler the light is divided into pump and probe beam with a $\frac{\lambda}{2}$-waveplate and a polarizing beam splitter (PBS). The best signal-to-noise ratio has been obtained using a relative power ratio of approximately $I_{\text{pump}}/I_{\text{probe}} \approx 4$. The pump beam goes through an EOM, which imprints sidebands onto the beam at a modulation frequency of 5 MHz. The frequency is generated by a direct-digital synthesizer (DDS) and enhanced by an LC-circuit, formed by the EOM crystal that acts as a capacitor and an inductance

[3]Thorlabs, DMLP605.

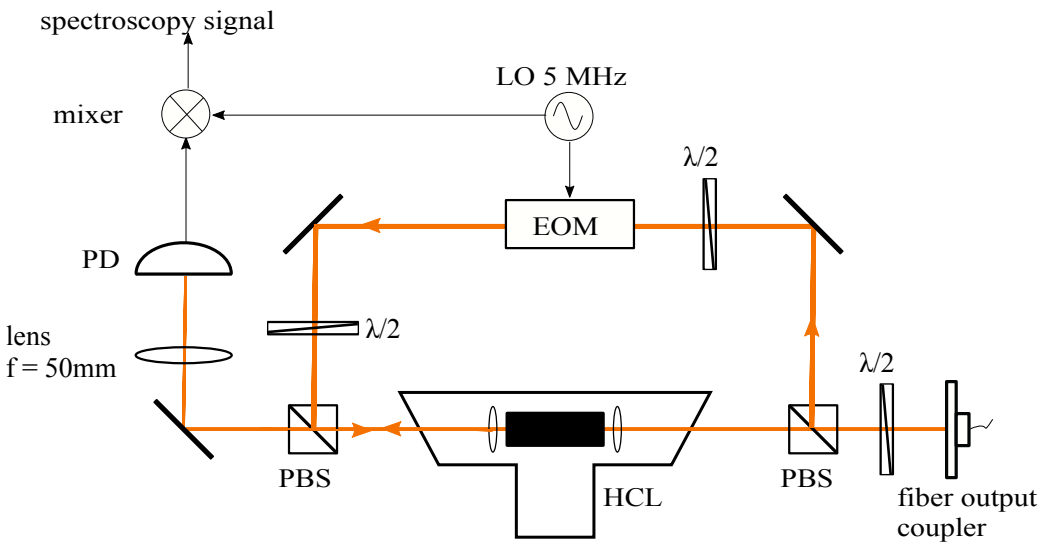

Figure 5.3.: The setup for the MTS. The ratio between the pump beam and the probe beam is $I_{\text{pump}}/I_{\text{probe}} \approx 4$. The modulation frequency applied to the EOM is 5 MHz and generated by a local oscillator (LO), which consists of a frequency generator in combination with a LC-circuit. The probe beam is detected with a photodiode. To obtain the final spectroscopy signal, the photodiode signal is mixed with the modulation frequency of the EOM. PD: photodiode, PBS: polarizing beam splitter, HCL: hollow cathode lamp.

of $L = 56\,\mu\text{H}$. Afterwards, the pump beam gets overlapped with the probe beam in the HCL. Figure 5.4 shows an example of the MTS signal for Dy. Two transitions can be assigned to the bosonic isotopes ^{164}Dy and ^{162}Dy, whereas three transitions can be assigned to fermionic isotopes. The amplitude of the resonances for the bosonic isotopes compared to the fermionic isotopes is much higher because the additional hyperfine structure of the fermions leads to more states, i. e. 9 for Dy, over which the fermions are distributed. Therefore, the number of fermions resonant to the respective light is only slightly more than 10 % of all fermions. The resonance of the bosonic ^{160}Dy and the resonances of the other fermionic transitions are out of the scan range.

The frequency difference between the ^{164}Dy and the ^{162}Dy resonance can be extracted by fitting the theoretical spectroscopy signal, Eq. 5.9, to the data and is determined to be 960.2(1) MHz. This agrees within the error bars with the value of 962(2) MHz obtained in [41]. The transition frequencies of the hyperfine states relative to the bosonic isotope ^{162}Dy can be calculated by

$$\Delta\nu_{\text{HFS}} = \Delta_{162} + E_{\text{e}}(F_{\text{e}}, J_{\text{e}}, I) - E_{\text{g}}(F_{\text{g}}, J_{\text{g}}, I), \tag{5.2}$$

where Δ_{162} is the isotope shift with respect to the bosonic ^{162}Dy and E_{i} are the hyperfine energies

$$E_{\text{i}} = \frac{1}{2}A_{\text{i}}C_{\text{i}} + \frac{1}{2}B_{\text{i}}\frac{3C_{\text{i}}\,(C_{\text{i}}+1) - 4I\,(I+1)\,J_{\text{i}}\,(J_{\text{i}}+1)}{2I\,(2I-1)\,2J_{\text{i}}\,(2J_{\text{i}}-1)} \tag{5.3}$$

with

$$C_{\text{i}} = F_{\text{i}}\,(F_{\text{i}}+1) - J_{\text{i}}\,(J_{\text{i}}+1) - I\,(I+1)\,. \tag{5.4}$$

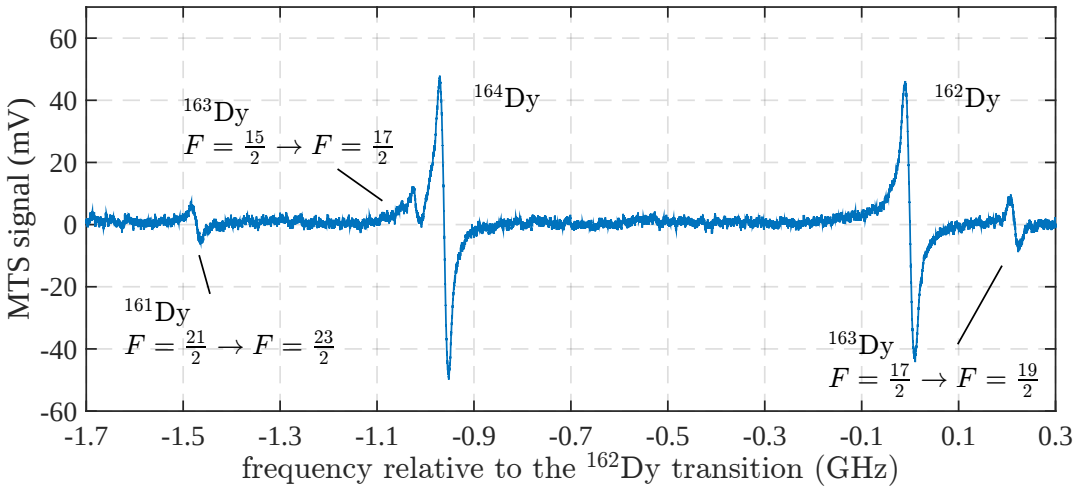

Figure 5.4.: Modulation-transfer spectroscopy signal for dysprosium. Two transitions can be assigned to the bosonic isotopes, whereas three transition are of fermionic isotopes. The hyperfine transitions are labeled by $F \rightarrow F'$. The signal was averaged over ten recording cycles.

Table 5.2 gives the hyperfine coefficients A and B and Table 5.3 gives the calculated and measured frequency differences of the hyperfine transitions relative to the ^{162}Dy bosonic isotope that corresponds to Fig. 5.4. The measured frequency differences agree within the error bars with the theoretically calculated ones.

Table 5.2.: Hyperfine A and B coefficients for the ground state (g. s.) and the excited state (e. s.) of the 626-nm transition [41], [29] (as cited in [58]).

g. s.	A (MHz)	B (MHz)
^{161}Dy	−116.2322	1091.574
^{163}Dy	162.7543	1153.8684
e. s.		
^{161}Dy	−187.0(1)	−317(4)
^{163}Dy	261.7(2)	−334(6)

In principle, already the spectroscopy signal could be used to lock the laser. However, for the 583-nm transition of Er and for the 626-nm transition of Dy broadening effects such as power broadening and pressure broadening affect the spectroscopy signal. The power broadening can be calculated by [31]

$$\Delta\omega_{\mathrm{FWHM}} = 2\pi \cdot \Delta\nu \left(1 + \frac{I}{I_{\mathrm{sat}}}\right)^{1/2}, \tag{5.5}$$

where $\Delta\nu$ is the natural linewidth and I_{sat} is the saturation intensity of the transition. For Dy a power of 4 mW leads to a power broadening of $\Delta\omega_{\mathrm{FWHM}} \geq 2\pi \cdot 1$ MHz. Additionally,

Table 5.3.: Calculated hyperfine transitions relative to the bosonic ^{162}Dy. For the calculations Eq. 5.3 is used and Table 5.2 gives the hyperfine coefficients A and B.

transition	$\Delta\nu$ (MHz)	$\Delta\nu_{\text{measured}}$ (MHz)
^{163}Dy: $F = 17/2 \rightarrow F' = 19/2$	212(2)	210(8)
^{163}Dy: $F = 15/2 \rightarrow F' = 17/2$	−1014(2)	−1011.0(1)
^{161}Dy: $F = 21/2 \rightarrow F' = 23/2$	−1470(2)	−1473.0(1)

the high background pressure in the HCL of 4 mbar, leads to pressure broadening of the transitions. The pressure broadening can be as large as 8.2 MHz [32]. Due to this two broadening effects the signal gets very large and therefore, this method is not optimal to lock the light of 583 nm and 626 nm, because the linewidths of these transitions are $\Gamma = 2\pi \cdot 190\,\text{kHz}$ and $\Gamma = 2\pi \cdot 136\,\text{kHz}$, respectively. By fitting the data points of our spectroscopy signal we extract a linewidth of $\Gamma = 2\pi \cdot \Delta\nu = 12.051(5)\,\text{MHz}$ for a total power of the two beams of approximately 10 mW. In Figure 5.5 one clearly sees, that the transmission peaks of the cavity are much narrower that the MTS spectroscopy signal and thus better for the locking purpose.

The spectroscopy still gives an absolute frequency reference to calibrate the frequency of the cavity modes by comparing the spectroscopy signal with the cavity transmission. Furthermore, it gives a stable reference, which can be used to determine the zero-crossing of the CTE of the cavity as discussed in the following section.

5.3. Zero Crossing of the ULE Cavity

One of the advantages of using mirrors and a cavity spacer out of ULE is that the coefficient of thermal expansion (CTE), α of ULE has a zero-crossing around room temperature (see Sec. 4.3 and Fig. 4.6). If the cavity is temperature stabilized at this special zero-crossing temperature T_C the length of the cavity becomes more stable against temperature fluctuations. For cavities stabilized at T_C frequency drifts on the order of Hz/s due to temperature fluctuations can be achieved [46, 71].

The cavity mirrors are optically contacted to the spacer and since both elements are made of ULE we expect T_C to be between 0 °C and 30 °C.

Around T_C the CTE of ULE can be approximated by

$$\alpha(T) = a\,(T - T_\text{C}) + b\,(T - T_\text{C})^2\,. \tag{5.6}$$

The linear expansion coefficient a is on the order of 10^{-9} /K^2 and the quadratic expansion coefficient b is on the order of 10^{-12} /K^2 [51]. Since we are interested only in a small region around T_C, keeping $(T - T_\text{C})$ small, and b is three orders smaller than a, the linear term is dominant (compare to Fig. 4.6) and we focus only on the linear approximation, which leads to a length change of

$$\mathrm{d}L = L\alpha\,(T)\,\mathrm{d}T = La\,(T - T_\text{C})\,\mathrm{d}T. \tag{5.7}$$

The relative change in frequency is directly connected to the change in length by

$$\frac{\Delta\nu}{\nu} = \frac{\Delta L}{L} = \frac{a}{2}(T - T_{\mathrm{C}})^2 \tag{5.8}$$

To determine T_{C}, we measure the frequency drift of the cavity resonance while changing the temperature of the cavity. The frequency drift is quantified by measuring the position of the cavity transmission relative to the modulation-transfer spectroscopy signal of the 626-nm transition for ^{162}Dy. For this the laser is scanned over more than one FSR and the respective traces are recorded with an oscilloscope[4]. Figure 5.5 shows the cavity transmission signal and the spectroscopy signal. The cavity transmission signal is fitted with a double Lorentzian function, whereas the spectroscopy signal is fitted with the theoretical spectroscopy signal derived in [63]

$$\begin{aligned} S(\omega_m) = & \frac{C}{\sqrt{\Gamma^2 + \omega_m^2}} \\ & \times [(L_{-1} - L_{-1/2} + L_{1/2} - L_1)\cos(\phi) \\ & + (D_1 - D_{1/2} - D_{-1/2} + D_{-1})\sin(\phi)], \end{aligned} \tag{5.9}$$

where

$$L_n = \frac{\Gamma^2}{\Gamma^2 + (\Delta - n\omega_m)^2} \tag{5.10}$$

and

$$D_n = \frac{\Gamma(\Delta - n\omega_m)}{\Gamma^2 + (\Delta - n\omega_m)^2}. \tag{5.11}$$

Γ is the linewidth of the transition, ω_m the modulation frequency, Δ the detuning from the atomic resonance and ϕ is the phase difference between the detected signal and the modulation field applied to the EOM to modulate the pump beam. The center position of the transmission peak of the cavity labeled with T in Fig. 5.5 is taken as frequency reference.

Additionally, we record the voltage at an NTC sitting on the aluminum block that holds the cavity (see Sec. 4.4) and use the associated temperature as actual cavity temperature. The NTC is part of a voltage divider and the temperature can be read out by calculating the resistance of the NTC. We changed the temperature from 27.0 °C to 17 °C in steps of 2 °C. Since the cavity has no thermal connection to the aluminum block, where the temperature is measured, the time between setting the temperature and measuring the relative position of the resonance was minimum 2 days. This ensures that the cavity has thermalized and reached the same temperature as the aluminum block. After reaching 17 °C we changed the temperature back to higher values to check if the time we waited for thermalization was enough or if we observe a hysteresis behavior as in [71]. Figure 5.6 shows the position of the ^{162}Dy transition relative to the cavity transmission as a function of the temperature of the aluminum block that holds the cavity. We do not observe a hysteresis behavior, which means, that the time we waited for thermalization was enough. For each data point

[4] LeCroy: SDA 760Zi-A.

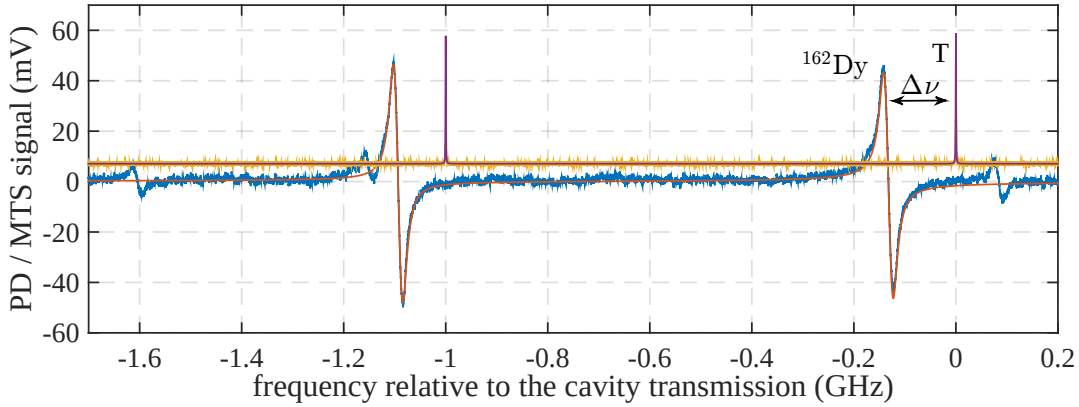

Figure 5.5.: Example of the spectroscopic trace recorded with the oscilloscope for the determination of the zero-crossing. The aluminum block that holds the cavity had a temperature of 16.58(6) °C

approximately 50 traces were recorded and the position was averaged. The error bars in Fig. 5.6 are the standard deviation, whereby the error bars for the temperature are not visible, because they are on the order of 5×10^{-2} °C. The data points are fitted with a quadratic function $\Delta\nu = c + \nu a(T - T_C)^2$, where c is a constant containing the minimal difference between the atomic resonance and the cavity transmission. From the fit we extract T_C to be

$$T_C = 21.78(5)\,°\mathrm{C}.$$

and the linear expansion coefficient a in Eq. 5.6 to be

$$a = 1.65(5) \times 10^{-9}\ /\mathrm{K}.$$

The error is the statistical error from the fit. We determine the temperature of the zero-crossing of the CTE with a precision of 50 mK, which satisfies the requirements given in Sec. 4.3. The result of 21.78(5) °C for T_C is very convenient because the temperature stabilization is very easy, i. e. no water cooling is required. Additionally, the difference to the room temperature is small and therefore the Peltier elements do not have to work at high power. In the following the cavity is stabilized at 21.78(5) °C and the locking of the 626 nm lasers is done.

5.4. Locking of the Laser Systems

The Pound-Drever-Hall (PDH) technique (see App. A.1) is used to lock the lasers for the light of 583 nm and of 626 nm. The idea is to modulate the laser light via a fiber-coupled EOM[5] with two different modulation frequencies, which results in sidebands at frequencies f_{shift} and f_{mod}. The frequencies are generated by two direct-digital synthesizer (DDS) and superimposed with a power combiner[6]. While the laser frequency is tuned to the atomic

[5]Jenoptik, PM635 (PM585) for the light of 626 nm (583 nm).
[6]Minicircuits, ZSC-2-4+.

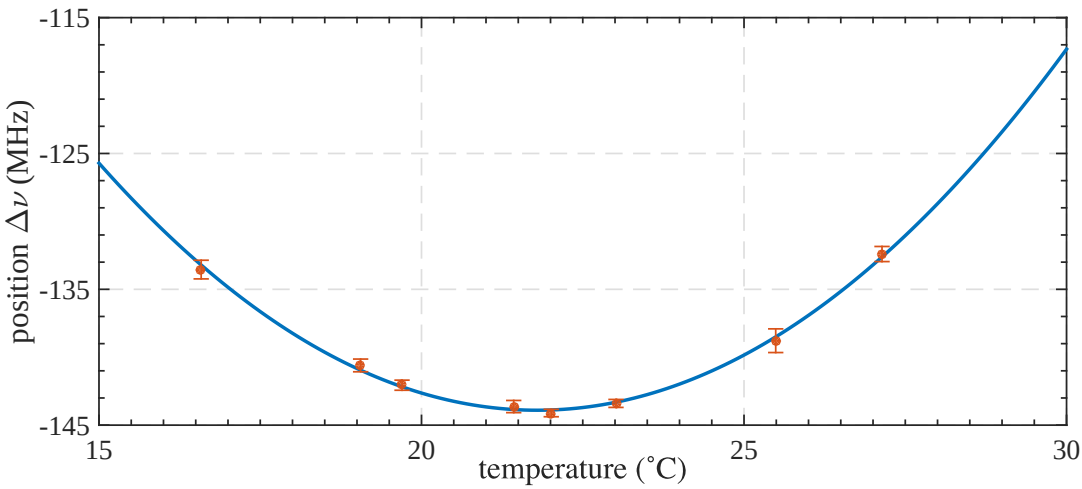

Figure 5.6.: The frequency difference of the ^{162}Dy spectroscopy transition and the cavity resonance is plotted as a function of the temperature of the aluminum block that hold the cavity. The data points are fitted with a quadratic function $\Delta\nu = c + \nu a(T - T_C)^2$. Each point is averaged over about 50 data points. The error bars are given by the standard deviation. The zero-crossing temperature is at 21.78(5) °C and $a = 1.65(5) \times 10^{-9}$ /K.

resonance, the locking is done with the additional sidebands by shifting f_{shift} to the cavity resonance and using this sideband together with the sidebands at f_{mod} to generate the error signal. In Figure 5.7 the locking scheme is illustrated schematically. f_{exp} labels the atomic resonance frequency and f_{n} labels the cavity modes. Figure 5.8 shows the schematic setup

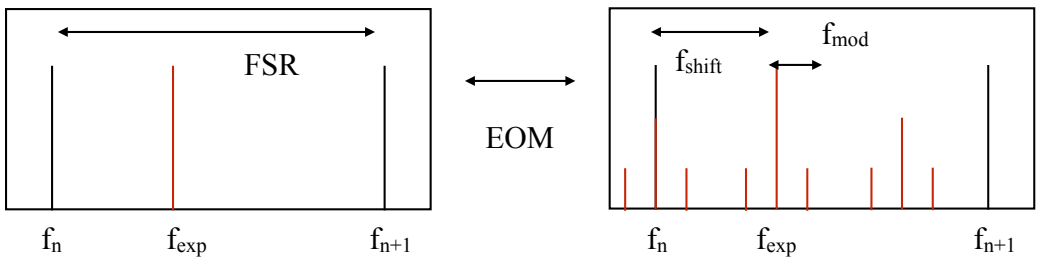

Figure 5.7.: Illustration of the locking scheme for the laser of light of 626 nm and 583 nm. f_{n} labels the cavity modes and f_{exp} labels the experimentally desired wavelength. f_{shift} and f_{mod} are the sidebands that are modulated by the EOM.

for the laser locking. The light of the laser gets divided by a polarizing beam splitter (PBS). Most of the power goes to the experiment and only approximately 5 mW are used for the laser locking. A fiber-coupled EOM modulates the sidebands at frequencies f_{shift} and f_{mod}. The reflected beam of the cavity is intercepted with a beam splitter and recorded with a photodiode. The detected signal is mixed with the modulation frequency f_{mod} to extract the PDH error signal. The laser is then stabilized with a PID controller. This locking method has several advantages compared to other systems realized with acousto-optic modulators (AOM) as in [58, 71]: The fiber-coupled EOM has a large bandwidth of 5 GHz, which gives

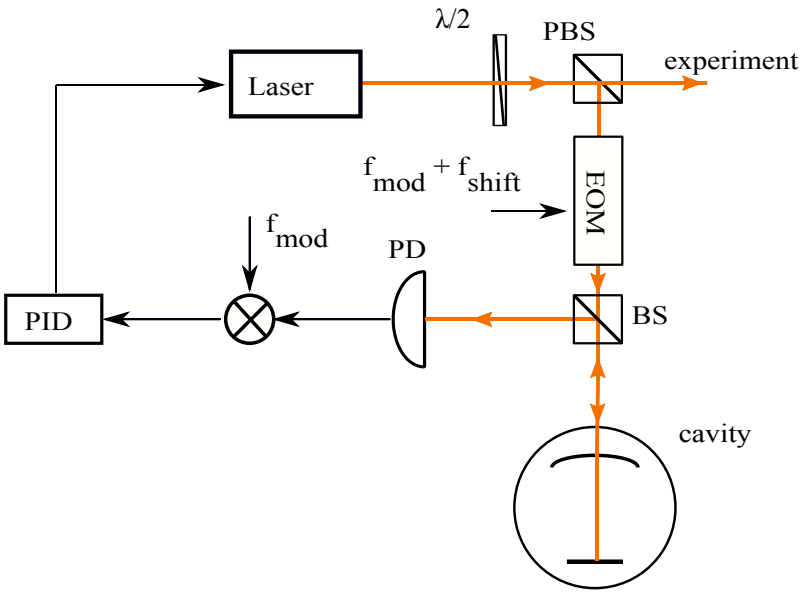

Figure 5.8.: Schematic drawing of the setup of the laser locking for the 626 nm light.

a large tuning range (large f_{shift} is possible) without the need to optimize the couplings to the AOMs. This facilitates the switching between the different isotopes. The optical setup gets much more easier compared to standard realizations of such systems [32, 58] because usually at least two AOMs in double pass configuration are necessary to obtain a sufficiently large frequency scan range for the laser light. The fiber-coupled EOM also provides a spatial mode cleaning, which makes the coupling into the cavity and the suppression of higher transversal modes easier. In total only one fiber-coupled EOM and one AOM are required with our system (see Fig. 3.7 and 5.8) for tuning, locking and power stabilization of the laser light. Figure 5.9 shows the PDH error signal that we obtain with a modulation frequency f_{mod} of 20 MHz. In Section 5.5 we extract the linewidth and therefore the finesse out of the error signal. Figure 5.10 shows the cavity transmission signal and the signal of the MTS, while the laser was scanned over more than one FSR. The sidebands are at a frequency of 200 MHz, whereas the sidebands at 20 MHz used for locking are not visible due to the low amplitude. This plot can be used as a reference to check how large the frequency f_{shift} must be, to shift the sideband to the cavity resonance to lock the laser light of 626 nm.

5.5. Performance of the Cavity

Beside the zero-crossing of the CTE, the free spectral range (FSR), the finesse, and the linewidth of the cavity are important parameters. In the following section we determine this three properties with different measurement methods. For all three measurements we use the light of 626 nm.

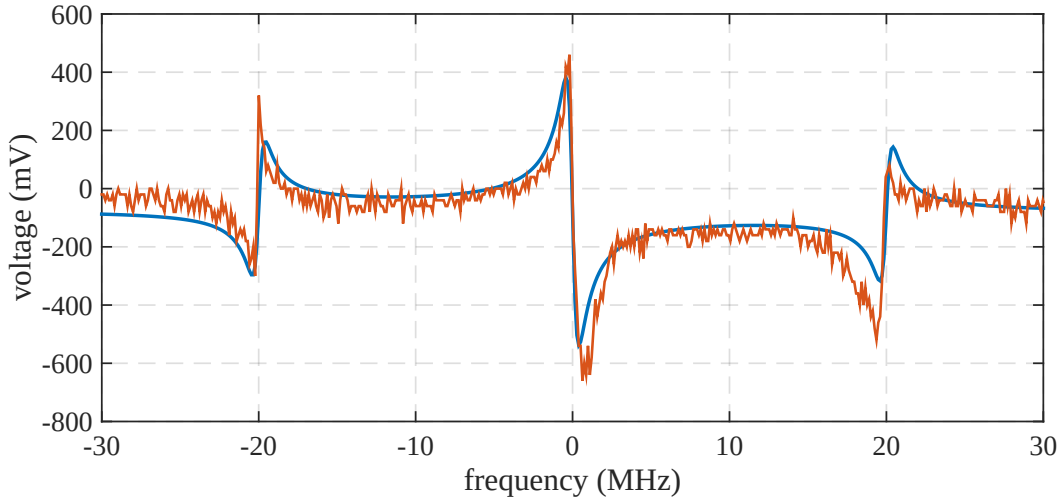

Figure 5.9.: PDH error signal of the 626 nm light obtained with the cavity.

Free Spectral Range and Linewidth out of the Transmission Signal

In this subsection we extract the FSR and the linewidth out of the transmission signal of the cavity. For this, we modulate sidebands on the laser light with the fiber-coupled EOM and scan the frequency of the laser over more than one FSR (1 GHz). We record the transmission of the cavity with an oscilloscope[7] and use the sidebands at known frequencies to convert the time axis into a frequency axis. Figure 5.10 shows the transmission of the cavity with sidebands modulated at 200 MHz. To measure the FSR we take the frequency difference between the center positions of the carrier of the transmission peaks (labled with C in Fig. 5.10), which are fitted with a Lorentzian function

$$f(x) = \frac{1}{\pi} \frac{A}{s^2 + (x - t)^2}. \tag{5.12}$$

Figure 5.11 shows a zoom into one cavity transmission peak and the Lorentzian fit. We did this with three different modulation frequencies, 100 MHz, 120 MHz, and 200 MHz and average the FSR to

$$\mathcal{F} = 989(8)\,\text{MHz}.$$

The slightly lower value than the expected FSR of 1 GHz can be explained by the optically contacted mirrors. Due to the mirrors, especially the curved mirror, the cavity distance is slightly increased, leading to a smaller free spectral range.

Since the linewidth of our 626 nm laser light is on the order of a few 10 kHz and therefore lower than the linewidth of the cavity for the theoretically best coating case of the mirrors ($\approx$ 50 kHz), it is possible to measure the linewidth by scanning the laser over the cavity resonance. We fit each transmission peak in Fig. 5.10 with the Lorentzian Function 5.12 and extract the linewidth. All 6 linewidths are then averaged to $\Delta\nu = 630(9)$ kHz.

[7] LeCroy: SDA 760Zi-A.

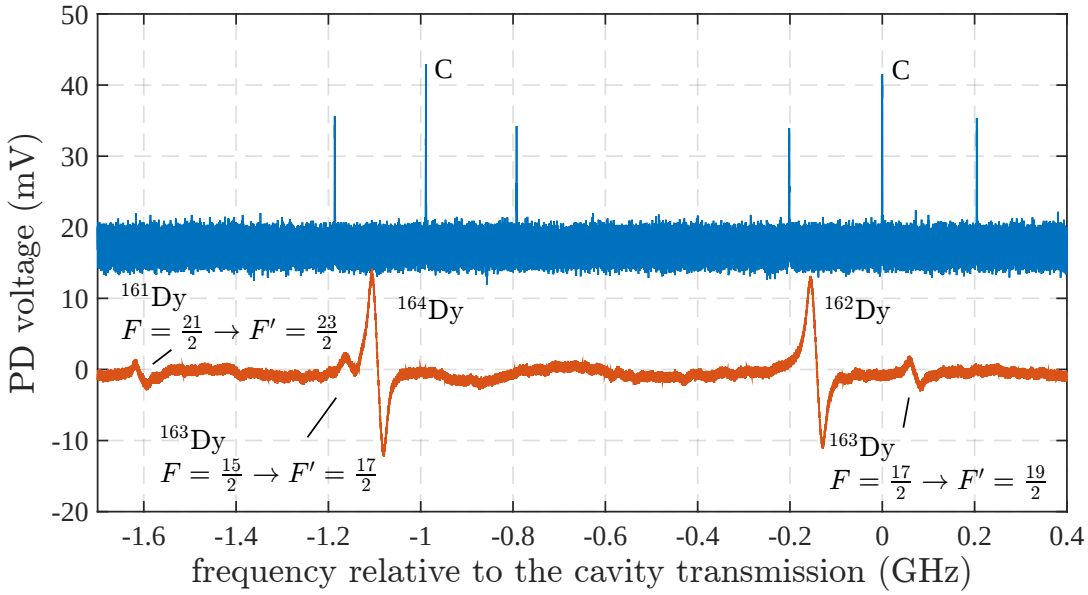

Figure 5.10.: Cavity transmission and the MTS signal. The laser is scanned over more than one free spectral range with a modulation frequency of 200 MHz switched on. The 20 MHz sidebands, that will be used for the generation of the PDH-signal, are not visible here because there amplitude is too small.

By combining the results obtained for the FSR and the linewidth of the cavity we calculate the finesse with Eq. 4.9 to

$$\mathcal{F} = 1569(23). \tag{5.13}$$

Finesse and Linewidth out of the Cavity Ring-Down Measurement

Another method to determine the linewidth of the cavity and to calculate the finesse with Eq. 4.9 is the cavity ring-down measurement. The working principle of the cavity ring-down measurement is based on the decay time of the light stored in the cavity. If the laser is locked to the cavity light enters the cavity and due to the reflections of the mirrors a part of the light remains trapped in the cavity modes. The equilibrium between the leaving $I_{\text{out}}(t)$ and entering intensity $I_{\text{in}}(t)$ is described by

$$\dot{I}_{\text{out}}(t) = \frac{1}{\tau}\left(I_{\text{in}}(t) - I_{\text{out}}(t)\right). \tag{5.14}$$

τ is the decay constant and defined as

$$\tau = \frac{1}{\alpha c}, \tag{5.15}$$

where α is the total lost per length unit and c the speed of light. If at $t = \xi$, the incoming intensity is suddenly switch of, $I_{\text{in}}(\xi) = 0$, then Eq. 5.14 reduces to

$$\dot{I}_{\text{out}}(t > \xi) = -\frac{1}{\tau} I_{\text{out}}(t). \tag{5.16}$$

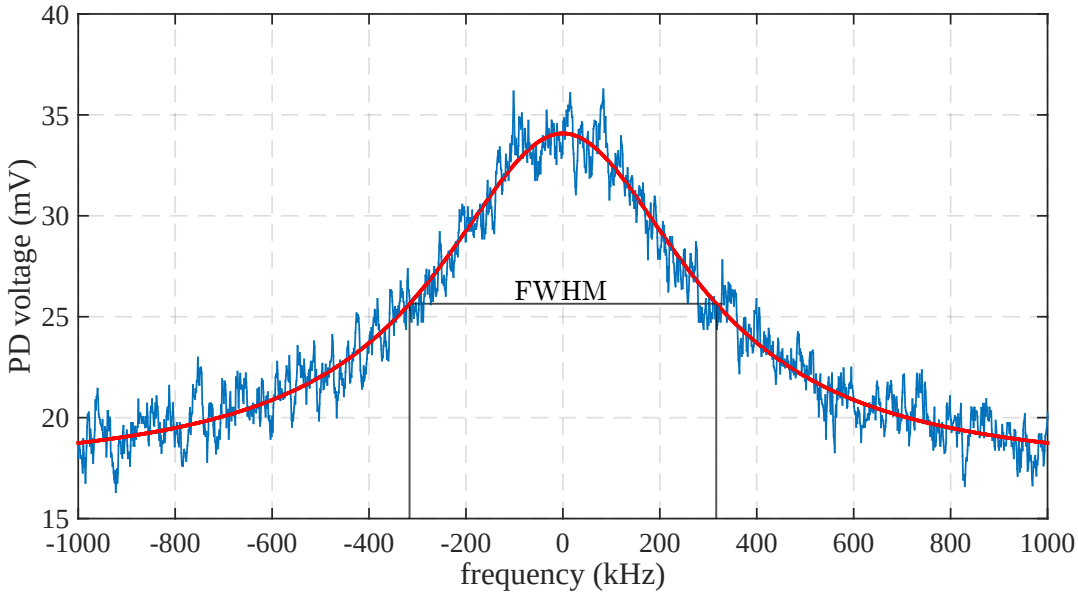

Figure 5.11.: Zoom into one cavity transmission peak. The cavity resonance is fitted with the Lorentz function from Eq. 5.12. The frequency axis is set to be zero at the resonance.

This differential equation has the simple solution

$$I_{\text{out}} = I_0 e^{-t/\tau}, \tag{5.17}$$

where I_0 is the intensity stored in the cavity. For this measurement we lock the 626-nm laser onto the cavity resonance as explained in Sec. 5.4 and change suddenly the frequency f_{shift} of the sideband, which is shifted to the cavity resonance. Since the sideband is not resonant to the cavity anymore, the input intensity is turned off. The intensity transmitted through the cavity is recorded with a photodiode. Figure 5.12 shows the exponential decay of the measured intensity. It is important that the switching occurs much faster than the decay time. Otherwise, the assumption of $I_{\text{in}}(t > \xi) = 0$ is not valid anymore and the decay is determined by the switching time. The EOM has a specified switching time of 0.2 ns and is therefore fast enough for this purpose, since we expect a decay time $\tau > 100$ ns.

To extract the decay time, the exponential function

$$f(t) = A + B \cdot e^{-\frac{t}{\tau}} \tag{5.18}$$

is fitted to the data. The constant A describes the intensity offsets, including stray light and the offset from the photodiode and B is the amplitude of the decay function. The photon lifetime can be determined to

$$\tau = 260.4(7)\,\text{ns},$$

which results, in a linewidth of the cavity of

$$\Delta\nu = 611(2)\,\text{kHz},$$

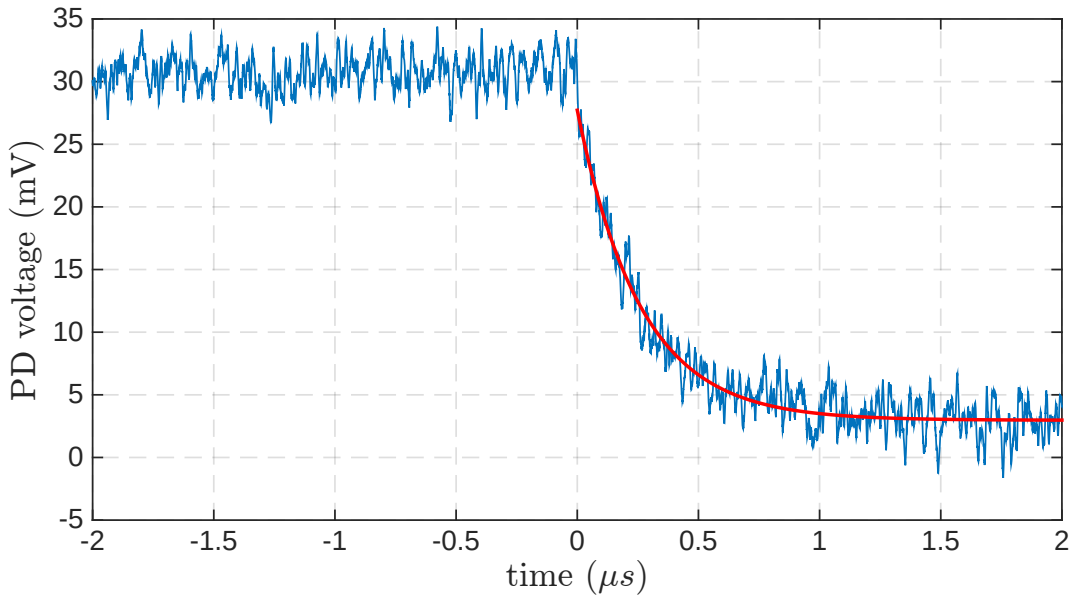

Figure 5.12.: Cavity transmission signal as a function of time. The intensity decays after shifting the sideband, on which the laser is locked, out of resonance.

by using Eq. 4.11. Combining the FSR of 989(8) MHz calculated with the cavity transmission and the obtained linewidth, the finesse of the cavity can be calculated using Eq. 4.9 to

$$\mathcal{F} = 1636(4).$$

Linewidth out of the PDH Error Signal

Beside the determination of the linewidth out of the cavity transmission signal and the cavity ring-down as a third method the linewidth is extracted out of the PDH error signal. This is done, by fitting [62]

$$S(\Delta) = A + B \cdot \frac{\Gamma\Delta\Omega\left(\sin(\varphi)\Gamma\left(\Gamma^2+\Delta^2+\Omega^2\right)+\cos(\varphi)\Omega\left(\Gamma^2-\Delta^2+\Omega^2\right)\right)}{\left(\Gamma^2+\Delta^2\right)\left(\Gamma^2+(\Delta+\Omega)^2\right)\left(\Gamma^2+(\Delta-\Omega)^2\right)} \tag{5.19}$$

to the data points, where A is a general offset, B is the amplitude of the signal, Γ is the linewidth of the cavity, Δ is the laser detuning with respect to the cavity resonance, Ω is the modulation frequency and φ is the phase between the reflected signal and the modulation signal.

In Figure 5.9 shows the fit to the recorded error signal. We extract a linewidth of 410(20) kHz. By using the FSR of 989(8) obtained before we can calculate the finesse to

$$\mathcal{F} = 2213(120). \tag{5.20}$$

Function 5.19 does not fit perfect to the data. This explains the deviation from the results obtained with the cavity transmission and the ring-down measurement. Nevertheless, the linewidth and therefore the finesse is of the same order and confirms the other results.

Discussion of the Cavity Parameters

Table 5.4 gives a summary of the results obtained via the three different measurement methods discussed above. Theoretically, following the coating curves for the mirrors in Fig. 4.4 provided by Lens-Optics[8] and using Eq. 4.10, one obtains for the finesse for light at 626 nm a minimum value of 6300, which is approximately a factor of 4 higher than in our case.

Table 5.4.: Summary of the results obtained for the finesse $\mathcal{F}$, the FSR, the linewidth $\Delta\nu$, and the reflection coefficient R with the different measurement methods.

	min. theo. calculated	trans. signal	cavity ring-down	PDH error signal
FSR (MHZ)	1000	989(8)	–	–
$\mathcal{F}$	6300	1569(23)	1636(4)	2213(120)
$\Delta\nu$ (kHZ)	159	630(9)	611(2)	410(20)
R (%)	99.95	99.800(3)	99.8082(5)	99.86(1)

One reason for the low finesse could be that the mirrors are not as good as specified. To verify the quality of the mirrors we measured the transmission for both type of mirror coatings with two mirrors, which we have in spare. We used light of 421 nm for the mirrors coated from 380 nm – 450 nm and light of 626 nm for the other mirror coating type. Table 5.5 gives the reflection coefficients that are calculated with the measured transmission. To take into account that some of the light is absorbed from the mirror substrate we assume an absorption of 10 %, according to Fig. 4.5. Although the absorption is estimated quite high, the finesse calculated for 626-nm with the measured transmission coefficient lies within the specifications and is higher than the finesses measured with the cavity. As a check we estimate the finesse of the cavity also for the light at 421 nm. For this we record the transmission with the oscilloscope and estimated the linewidth to be > 1 MHz. The corresponding finesse is lower than 1000. This leads to the conclusion that the mirror coatings are not casing the low finesse.

Table 5.5.: Measured transmission for both type of mirror coatings. Additionally the resulting finesse is calculated with this reflection coefficient and a FSR of 989(8) MHz.

wavelength	power (mW)	trans. power (µW)	ref. coeff. (%)	finesse
421 nm	38.0(2)	28.5(2)	99.92(2)	3800(38)
626 nm	10.0(2)	3.45(1)	99.96(9)	8277(62)

Another possible explanation for the low finesse is that during the evacuation water steamed up on the mirrors. This happens especially if the evacuation occurs too fast or the vacuum chamber gets reopened without floating the chamber with argon. Since we pump without any special needle valve that controls the pumping speed and had also to reopen

[8] Lens-Optics GmbH

the chamber once, this is a good explanation. According to Lens-Optics[9] the steaming effect should get stronger for wavelengths in the UV. This agrees with the estimated finesse of the cavity for the light of 421 nm. Therefore this effect could be a plausible explanation for the unexpected low finesse.

In summary, for light of 626 nm the finesse of the cavity is approximately by a factor of 4 lower than for the worst theoretical value. Since the mirrors coated for light of 626 nm, 583 nm, 741 nm, and 631 nm have the highest reflection at 626-nm we assume that the finesses for the other wavelengths are even worse. For the locking of the laser light this means, that the slope of the PDH errror signal is 4 times less than expected, because the slope is proportional to $\frac{1}{\Delta\nu}$. The transitions of 626 nm and 583 nm have linewidths of 136 kHz and 190 kHz. Since the lasers for these transitions have a small enough fee running linewidth the main task of the cavity is the long term stabilization. The lock of this two lasers is therefore possible. However, for the lasers of 741 nm and 631 nm as well for the lasers for Rydberg excitation the transition linewidths are below 10 kHz and therefore the locking is, if at all possible, very challenging.

[9] Private communication.

6. Conclusion and Outlook

The main goal of this master thesis was to set up and characterize an optical cavity, which can be used to stabilize different lasers at several wavelengths. In the main experiment these lasers will be used for slowing, cooling, and trapping of Er and Dy atoms and for Rydberg excitation. To reach a high stability against temperature fluctuations we chose ultra low expansion glass (ULE) as material for the mirrors and the cavity spacer. Due to technical limitations it is not possible to produce mirrors with high reflectivity at all necessary wavelengths. Therefore, we decided to built a double cavity. This means we used one ULE spacer but two different pairs of mirrors. One pair of mirrors is coated for the wavelengths at 583 nm, 626 nm, 631 nm, and 741 nm, which are cooling transitions in erbium and dysprosium. The second pair of mirrors is coated for the range from 380 nm to 450 nm to be able to lock lasers for Rydberg excitation.

To shield the cavity as good as possible from the environment, i. e. from acoustic and thermal noise, the cavity is placed in a vacuum chamber with a pressure on the order of 2×10^{-8} mbar. For further stability, the cavity inside the vacuum chamber is surrounded by two additional heat shieldings. The temperature of the outer one of these two shieldings is stabilized via Peltier elements. For monitoring of the temperature several thermistors are distributed over the vacuum chamber and can be read out with an Arduino system.

The temperature where the ULE exhibits a minimal thermal expansion was determined to be at 21.78(5) °C and therefore the cavity is stabilized to this value. To determine the free spectral range (FSR), the linewidth, and finesse of the cavity we performed three different measurements. First, we determined the FSR to 989(8) MHz by scanning the 626-nm laser over two cavity resonances and extracted the frequency difference of the transmission peaks by fitting a Lorentzian function. Additionally, we modulated sidebands on the laser beam with an electro-optical modulator (EOM) and used them to calibrate the frequency axis. Further, the linewidth was extracted from the fit of the transmission peaks and was determined to 630(9) kHz, which leads to a finesse of 1569(23). As a second measurement we performed a cavity ring-down and the resulting finesse was 1636(4). Finally, we extracted a linewidth of 410(20) kHz out of the PDH error signal, leading to a finesse of 2213(120).

The finesse obtained with these three methods deviate by a factor of $\approx$ 4 form the theoretically expected value. We come to the conclusion, that due to too fast pumping and reopening of the cavity water steamed up on the mirrors. This could have degraded the reflection of the mirrors and caused therefore the lower finesse compared to the expected value. Nevertheless, it was possible to lock the 626 nm laser light to the cavity.

The next step in the experiment will be the realization of the single- and double-species magneto optical traps (MOTs) of Er and Dy.

6.1. Er–Dy Quantum Mixture: Motivation and Vision

So far, quantum-mixture experiments with dipolar atoms has not yet been realized and even never considered in theory. Our experiment would then be the first to go in this direction. We indeed plan to combine two strongly magnetic atomic species for the first time. From the experimental realization point of view the Er–Dy mixture presents several advantages. One advantage for the combination of Er and Dy is that they share many similar properties, e. g. strength of the laser cooling transitions, polarizability, anisotropic interaction character, and similar atomic masses and melting points. Both elements give a convenient choice of bosonic and fermionic isotopes (see Table 2.1) that gives opportunities to have three different types of mixtures: Bose-Bose, Fermi-Fermi and Bose-Fermi.

A first aspect to be studied is the interspecies interaction of Er and Dy having an imbalance on the dipolar interaction, where $\mu = 7\mu_B$ for Er and $\mu = 10\mu_B$ for Dy and different total angular momentum J. Both elements offer a rich spectrum of intraspecies Feshbach resonances [34, 59, 60]. The Feshbach spectroscopy of the mixture will add important information for the understanding of scattering physics of dipolar gases.

For the Fermi-Fermi mixture the crossover from a Bose-Einstein Condensate (BEC) to Bardeen-Cooper-Schrieffer (BCS) superfluid (BEC–BCS crossover) with dipole-dipole interaction (DDI) is of large interest. The BEC-BCS crossover is important for the understanding of superconductors and the associated superfluidity [82]. Depending on the interaction strength between the atoms, given by the scattering length a, the fermions can either form molecules or weakly bound pairs, so called Cooper-pairs. Both the BEC and the Cooper-pairs give explanation to different types of superfluids. In many experiments the BEC–BCS crossover has been shown, e. g. in ^{6}Li and ^{40}K [18, 70], and the whole range from BEC to BCS can be investigated. These experiments have in common that they work with alkali atoms having isotropic interaction. Dipolar atomic species give the possibility to study the crossover under the influence of long-range and anisotropic dipolar interaction. Atoms forming a Cooper-pair have opposite momentum, because of the conservation of momentum [40]. In momentum space the Fermi surface for alkali atoms is spherical, due to the isotropic interaction, whereas for dipolar atomic species the Fermi surface can be deformed [2], which may have an impact on the Cooper-pairing mechanism. For alkali atoms such as ^{6}Li and ^{40}K the experimental technique is to prepare the atoms equally in their lowest two spin states and tune the interaction by a Feshbach resonance. However, for dipolar atoms this type of preparation is complicated by dipolar relaxation effects [14] occurring as a consequence of the long-range dipolar interaction. In a dipolar relaxation process the spin is flipped, since for dipol-dipol interaction the total spin is not preserved and the atoms relax into the state with lowest energy. This issue can be circumvented by using two different atomic species. The idea is to prepare both species in their lowest spin states. Again a Feshbach resonance can then be used to tune the interaction between the atoms.

Another interesting case is to investigate the behavior of the atoms without the external magnetic field, that polarizes the atoms. Without the polarization, the dipoles of the atoms are not frozen anymore and will organize their orientation by them self. Spinor Bose gases are gases with a spin degree of freedom that, similar to the BEC–BCS crossover, have been

studied in detail with alkali atoms [75]. The dipolar characteristic of Er and Dy will add new aspects. Since the dipole dipole interaction is spin dependent, this will lead to a competition with the spin dependent contact interaction for the local spin ordering of the spinor gas. For ^{87}Rb in the $F = 1$ state the ratio (ϵ_{dd}) between the dipole-dipole interaction strength ($a_{\mathrm{dd}} = {}^{\mu_0\mu^2 m}/_{12\pi\hbar^2}$) and the contact interaction strength given by the scattering length a is $\epsilon_{\mathrm{dd}} = 0.002$. In comparison, for Dy, ϵ_{dd} is on the order of 1 for a typical scattering length [75]. The large total angular momentum quantum number J of Er ($J = 6$) and Dy ($J = 8$) gives rise to the realization of spin-N systems with large N, i. e. $2J + 1$ different states (13 for Er and 17 for Dy).

6.2. Rydberg Excitation

An atom excited to a Rydberg state is a highly excited atom with a large principal quantum number n. Rydberg atoms exhibit many special properties, e. g. a large orbital radius scaling with n^2, which leads to a high polarizability, and a long lifetime proportional to n^3 (for Rubidium the theoretical lifetime of the $110S_{1/2}$ state is 1.7 ms) [7, 57]. However, for Rydberg states with a high angular momentum quantum number l, the lifetime increases further with a scaling $\tau \propto n^5$ [35]. Due to the high polarizability a large electric dipole moment can be induced, resulting in a strong long-range interaction. Similar to a Feshbach resonance, the interaction strength is tunable [6].

Rydberg excitation using a single photon excitation scheme is technically challenging from the aspect of laser technology, as usually laser light in the UV is required. In order to overcome this problem, two photon excitation schemes are commonly used in the field of ultracold Rydberg atoms. Here, the excitation lasers are operated with a detuning with respect to the intermediate state in order to minimize photon scattering, which eventually results in a heating of the ultracold sample. However, this intermediate state detuning also results in a reduction of the coupling strength between ground- and Rydberg state. The rich level structure of Er, as shown in Chap. 2, allows for various two photon excitation schemes via a narrow line intermediate state, which potentially can be utilized to increase the coupling between ground and Rydberg state.

Further, the sub-merged shell electron configuration of Er (see Sec. 2.1) allows to excite either an electron in the $6s$ or the $4f$ state. Utilizing a two photon excitation scheme, the excitation of an $4f$ electron to states with a high angular momentum and therefore, Rydberg states up to $l = 5$ are reachable in a straight forward manner.

In addition, similar to alkaline earth atoms, the core of an Er Rydberg atom remains optically active and thus still can be addressed, e. g. for trapping, detecting or further cooling.

A. Appendix

A.1. Pound-Drever-Hall Error Signal

The Pound-Drever-Hall (PDH) technique [25] is a very powerful technique to frequency stabilize laser systems using a Fabry-Perot cavity as frequency reference. The PDH error signal is created by modulating sidebands on the laser beam and by extracting the phase difference between the sidebands and the carrier of the laser beam after it is reflected from the Fabry-Perot cavity. The following Appendix gives a brief summary of the derivation of the PDH error signal.

First, we want to concentrate on the reflection of a monochromatic beam from a Fabry-Perot cavity. The incoming electrical field can be written as

$$E_{\text{inc}} = E_0 \mathrm{e}^{i\omega t}$$

while the reflected beam is

$$E_{\text{ref}} = E_1 \mathrm{e}^{i\omega t}$$

E_0 and E_1 are the complex amplitudes, containing the relative phase. The ratio between the incoming and the reflected beam leads to the reflection coefficient [12]

$$F(\omega) = \frac{E_{\text{inc}}}{E_{\text{ref}}} = \frac{r\left(\mathrm{e}^{\frac{i\omega}{FSR}} - 1\right)}{1 - r^2 \mathrm{e}^{\frac{i\omega}{FSR}}}, \tag{A.1}$$

where r is the reflection coefficient of the mirrors and FSR the free spectral range. If the frequency of the laser light is exactly an integer multiple of the FSR, the phase difference between the incoming and reflected beam is 180° and therefore this two beams interfere destructively. If the laser frequency does not match the FSR, the phase difference is different from 180° and the two electric field do not cancel out each other. The phase difference indicates, on which side of the cavity resonance the laser frequency is on. To measure the phase of the reflected beam, the incoming beam gets phase modulated, which generates sidebands on the laser beam. After the reflection of the cavity the sidebands interfere with the carrier and the phase is extracted from the beat pattern.

For the phase-modulation of the laser light and therefore, for the creation of the sidebands a Pockels-crystal is used. An important attribute of a Pockels crystal is that the refraction index depends linearly on the applied electric field:

$$n(E) = n + aE$$

For the PDH technique a sinusoidal electrical field is applied to the crystal and the electrical field of the laser beam after the crystal can be described by

$$E_{\text{inc}} = E_0 \mathrm{e}^{i(\omega t + \beta \sin(\Omega t))},$$

where Ω is the frequency of the electrical field, which is applied to the Pockels crystal and β is the parameter for the modulation depth. If $\beta < 1$, the expression of the incoming electrical field can be expanded using the Bessel functions [12]

$$E_{\text{inc}} \approx E_0 \left[J_0(\beta) + 2iJ_1(\beta)\sin(\Omega t)\right] \mathrm{e}^{i\omega t}$$

where terms of higher order are neglected, because $J_1(\beta)/J_0(\beta) \approx 0.2$ for $\beta = 1$. For $\beta < 1$ this ration becomes even smaller. Using $\sin(ix) = \frac{\mathrm{e}^{ix} - \mathrm{e}^{-ix}}{2i}$ the electrical field becomes

$$E_{\text{inc}} = E_0 \left[J_0(\beta)\mathrm{e}^{i\omega t} + J_1(\beta)\mathrm{e}^{i(\omega+\Omega)} - J_1(\beta)\mathrm{e}^{i(\omega-\Omega)}\right] \tag{A.2}$$

In Eq. A.2 terms with frequencies ω, $\omega - \Omega$ and $\omega + \Omega$ appear, where ω is the frequency of the carrier and $\omega \pm \Omega$ are the frequencies of the two sidebands. The power in the carrier and in each first-order sideband is given by [12]

$$P_{\text{C}} = J_0^2(\beta)\, P_0 \tag{A.3}$$

for the carrier and

$$P_{\text{S}} = J_1^2(\beta)\, P_0 \tag{A.4}$$

for the sidebands, where P_0 is the total power of the incident beam. The distribution of the power between the carrier and the sidebands depends on the modulation depth β. With the reflection coefficient from Eq. A.1 and the modulated incoming beam in Eq. A.2 the reflected beam can be written as [12]

$$E_{\text{ref}} = E_0 \left[F(\omega)J_0(\beta)\mathrm{e}^{i\omega t} + F(\omega+\Omega)J_1(\beta)\mathrm{e}^{i(\omega+\Omega)} - F(\omega-\Omega)J_1(\beta)\mathrm{e}^{i(\omega-\Omega)}\right] \tag{A.5}$$

The power measured at the photodiode is $P_{\text{ref}} = |E_{\text{ref}}|^2$. In comparison to a beam at single frequency without sidebands Eq. A.5 leads to additional terms appearing due to the interaction of the carrier with the sidebands. The most interesting terms are the one which oscillate at the modulation frequency Ω, because they sample the phase of the reflected carrier:

$$2\sqrt{P_{\text{C}}P_{\text{S}}}\mathrm{Re}\left[F(\omega)F^*(\omega+\Omega) - F^*(\omega)F(\omega-\Omega)\right]\cos(\Omega t)$$

and

$$2\sqrt{P_{\text{C}}P_{\text{S}}}\mathrm{Im}\left[F(\omega)F^*(\omega+\Omega) - F^*(\omega)F(\omega-\Omega)\right]\sin(\Omega t).$$

Usually, depending on the modulation frequency only one of these two terms will survive, i. e. for low modulation frequencies $F(\omega)F^*(\omega+\Omega) - F^*(\omega)F(\omega-\Omega)$ is purely real, whereas for high frequencies it is purely imaginary. Using a mixer, which forms the product of two signals, the terms can be extracted. The product of two sine waves is

$$\sin(\Omega t)\sin(\Omega_0 t) = \frac{1}{2}\left\{\cos[(\Omega-\Omega_0)t] + \cos[(\Omega+\Omega_0)t]\right\} \tag{A.6}$$

For the case that $\Omega \approx \Omega_0$, the cosine which contains the frequency difference becomes a dc signal, which can be isolated using a low-pass filter. Thereby mixing the output signal of

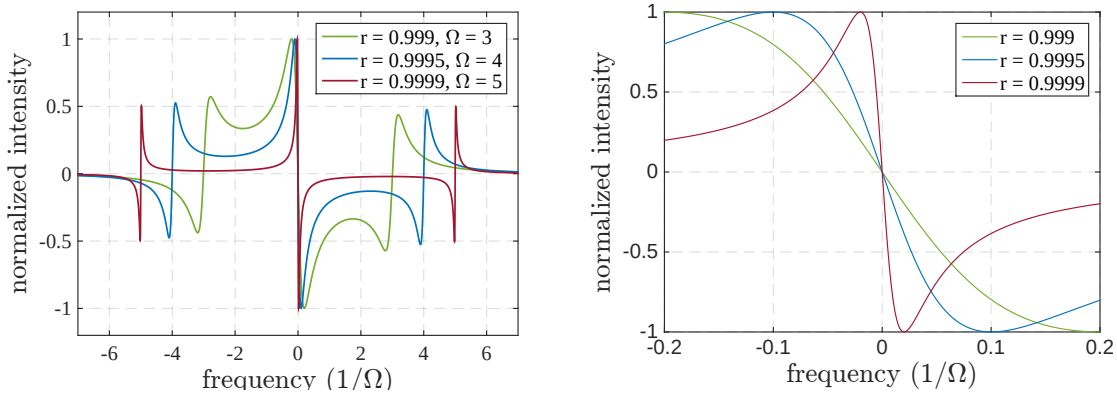

(a) Overview with differend reflection coefficients and modulation frequencies.

(b) Zoom-in on the slope of the central peak.

Figure A.1.: (a) PDH error signal with 3 different modulation frequencies and 3 different reflection coefficients. (b) Slope of the PDH error signal with 3 different reflection coefficients.

the photodiode with the modulation signal and applying a low-pass filter we can extract the PDH error signal for high modulation frequencies. Since at low modulation frequencies the term $F(\omega)F^*(\omega+\Omega) - F^*(\omega)F(\omega-\Omega)$ is purely imaginary only the cosine term is relevant and the signal need to be phase shifted to obtain the same mixing behavior. Afterwards the error signal can be fed to a PID controller that stabilizes the laser, e. g. by changing the laser current and the grating angle with a piezo element for an external cavity diode laser.

In Figure A.1(a) three different error signals as a function of the detuning are plotted. For each signal the modulation frequency of the EOM and the reflection coefficient of the mirrors, thus the finesse (Eq. 4.9), are changed. The change of the modulation frequency results in a different position for the wings of the error signal. A higher modulation frequency leads to a higher capture range, i. e. the region where the error signal is unequal zero and has the correct sign for driving the laser back onto resonance. However, the drawback of a higher modulation frequency is that the value of the error signal between the wings is small and therefore the influence on the regulation decreases. On the other hand, the change of the reflection coefficient results in a displacement of the minima and maxima, respectively. A higher reflection coefficient shifts the minima and maxima towards the center and therefore the slope around the central point increases. This central slope of the error signal can be expressed by [12]

$$D = -8\frac{\sqrt{P_C P_S}}{\Delta\nu}. \tag{A.7}$$

The slope is proportional to the power of the carrier and the sidebands and to the inverse of the linewidth of the cavity. The sensitivity of the laser stabilization with the PDH technique to frequency fluctuations is directly related to the steepness of the slope. The steeper the slope, the higher the inherent gain of the laser stabilization. A simple electronic amplification also amplifies the present technical noise and would therefore not lead to an increased signal-to-noise ratio. Figure A.1(b) shows the slope for three different reflection

coefficients for the same modulation frequency. For a given linewidth of the cavity, one can maximize the slope D by finding an optimal value for $\sqrt{P_C P_S}$. The maximum value for D can be found if $P_S/P_C = 0.42$, which corresponds to a modulation depth of $\beta = 1.08$.

A.2. Modulation-Transfer Spectroscopy

The modulation-transfer spectroscopy (MTS) is a spectroscopy technique based on two counter-propagating beams, called pump and probe beam. The pump beam passes through an electro-optical modulator (EOM) and sidebands are imprinted on the beam. The modulation is already described in Appendix A.1. After the EOM the pump beam can be represented by the carrier frequency ω_C and sidebands separated by the modulation frequency ω_m [63]

$$\begin{aligned} E = E_0 \Bigg[& \sum_{n=0}^{\infty} J_n(\delta) \sin(\omega_C + n\omega_m) t \\ & + \sum_{n=1}^{\infty} (-1)^n J_n(\delta) \sin(\omega_C + n\omega_m) t - J_1(\delta) \sin(\omega_C - \omega_m) t \Bigg]. \end{aligned} \tag{A.8}$$

$J_n(\delta)$ represents the Bessel function of order n and δ is the modulation index. If the modulation index $\delta < 1$, only the first order sidebands have to be considered and Eq. A.8 simplifies to [63]

$$E = E_0 \left[J_0(\delta) \sin \omega_C t + J_1(\delta) \sin(\omega_C + \omega_m) t - J_1(\delta) \sin(\omega_C - \omega_m) t \right]. \tag{A.9}$$

Therefore, the pump beam consists of three frequency components after the EOM, i. e. ω_C, $\omega_C + \omega_m$, and $\omega_C - \omega_m$. When the pump and the probe beam are overlapped in the spectroscopy cell four-wave mixing occurs, where a fourth wave is generate by the combination of three other waves [69]. The four-wave mixing is related to the non-linear polarization of the medium

$$P_{NL} = \chi^{(3)} E^3.$$

If E is the sum of three waves of three different frequencies ω_1, ω_2, and ω_3, E^3 leads to different frequency combinations and the generation of a fourth wave. In the case of the MTS, two frequency components of the pump beam combine with the frequency of the probe beam and generate a fourth frequency component that can be treated as a sideband of the probe beam. The sidebands of the probe beam, modulated in the vapor of the spectroscopy cell, beat with the probe beam leading to [63]

$$\begin{aligned} U_{PD}(\Delta, t) = & \frac{C}{\sqrt{\Gamma^2 + \omega_m^2}} \\ & \times \left[(L_{-1} - L_{-1/2} + L_{1/2} - L_1) \cos(\omega_m t + \phi) \right. \\ & \left. + (D_1 - D_{1/2} - D_{-1/2} + D_{-1}) \sin(\omega_m t + \phi) \right], \end{aligned} \tag{A.10}$$

where

$$L_n = \frac{\Gamma^2}{\Gamma^2 + (\Delta - n\omega_m)^2} \tag{A.11}$$

and

$$D_n = \frac{\Gamma(\Delta - n\omega_m)}{\Gamma^2 + (\Delta - n\omega_m)^2}. \tag{A.12}$$

Δ denotes the detuning of the laser frequency to the atomic resonance frequency and Γ is the linewidth of the transition. The beat signal $S(\omega_m)$ is detected with a photodiode and a phase detector mixes the signal of the photodiode with the modulation signal. Using the trigonometric formula A.6 leads to a DC term and an oscillating term. With a low-pass filter the DC term can be extracted and the spectroscopy signal

$$\begin{aligned} S(\Delta) = & \frac{C}{\sqrt{\Gamma^2 + \omega_m^2}} \\ & \times \left[(L_{-1} - L_{-1/2} + L_{1/2} - L_1) \cos(\phi) \right. \\ & \left. + (D_1 - D_{1/2} - D_{-1/2} + D_{-1}) \sin(\phi) \right] \end{aligned} \tag{A.13}$$

obtained. It is important to note, that the modulation occur only, if the condition for the sub-Doppler resonance is fulfilled. Otherwise, the four-wave mixing does not transfer the sidebands onto the probe beam. This means that only atoms of the velocity class zero contribute to the spectroscopy signal and therefore the transition is not broadened by the motion of the atoms. The resonance position of the MTS signal is always located at the center of the sub-Doppler resonance.

A.3. Electronic Circuits

All used electronic circuits are designed by Dr. Manfred Mark.

Measurement Bridge

There are two measurement bridges (MBs) on one circuit, which are framed with the black dashed line in the electronic circuit below. The MB for the resistor two with negative temperature coefficient (NTC2) consists of has a potentiometer to set the desired temperature. The aim of the temperature PID is to regulate the resulting temperature difference of the MB to zero. Therefore, with the MB for NTC2 we can reach the following resistance values:

$$R_{\mathrm{NTC}} = R_{11} \frac{R_8 + R_{\mathrm{poti}}}{R_{12}} \tag{A.14}$$

for minimum temperature and

$$R_{\mathrm{NTC}} = R_{11} \frac{R_8}{R_{12} + R_{\mathrm{poti}}} \tag{A.15}$$

for maximum temperature. If instead of a NTC a PTC (positive temperature coefficient) is used the minimum an maximum temperature are reversed. The resistor R_8, which defines the reachable temperature range is not predefined and has to be chosen appropriately.

For the NTC1, additionally to R_{16}, dip switches are implemented, that can be used to add additional resistors in series to R_{16}. Therefore, with this measurement bridge a higher temperature range can be reached:

$$R_{\mathrm{NTC}} = R_5 \frac{R_{16} + R_{\mathrm{poti}} + R_{\mathrm{switch}}}{R_6} \tag{A.16}$$

for the minimum temperature and

$$R_{\mathrm{NTC}} = R_5 \frac{R_{16}}{R_6 + R_{\mathrm{poti}}} \tag{A.17}$$

for the maximum temperature. The other elements on the circuit are either for the supply voltage or not used. The connection from the MB to the PID is done via a SUB-D15 connector.

Temperature PID

The temperature PID is adapted to the measurement bridge and consists also of two independent PIDs. The circuits of both PIDs are the same, whereby for the resistors and capacitors different values can be inserted to adjust the proportional, integral and differential part. Besides the PID, there are are also other parts on the circuits such as voltage supply and monitor output. Table A.1 gives a list of all resistors and capacitors, which we have chosen properly.

Table A.1.: Values for the different components of the temperature PIDs. The designations are consistent with the circuit below. The derivative term is not used in our case.

Component	Value
Rp1 1	13 kΩ
Rp1 2	100 kΩ
Rd1	–
Cd1	–
C_In 1	470 µF
Rp2 1	11 kΩ
Rp2 2	150 kΩ
Rd2	–
Cd2	–
C_In 2	100 µF

For the temperature stabilization of the cavity the derivative part of the PID is not used, because he reacts on the rate of change, which is slow for temperature. With the potentiometer $R_{\mathrm{pot}}1$ and $R_{\mathrm{pot}}2$ the output current of the PID can be limited. For this the connections $P11$ and $P5$ have to be jumpered.

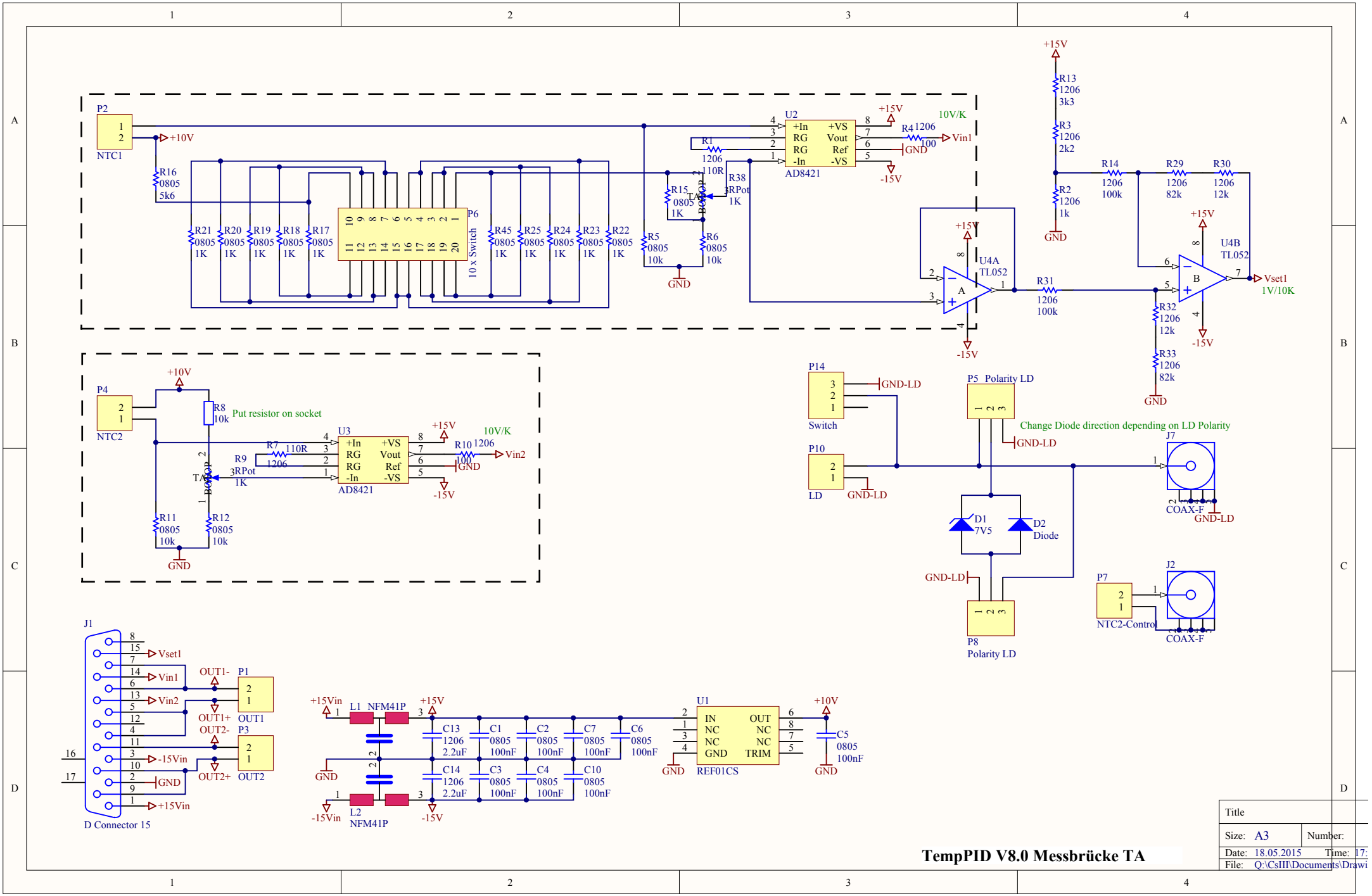
P2
NTC1
+10V
R16
0805
5k6
R21 0805 1K
R20 0805 1K
R19 0805 1K
R18 0805 1K
R17 0805 1K
P6
10 x Switch
R45 0805 1K
R25 0805 1K
R24 0805 1K
R23 0805 1K
R22 0805 1K
R5 0805 10k
R6 0805 10k
R15 0805 1K
R38 3RPot 1K
TA
BOOP
GND
U2
AD8421
+In
RG
RG
-In
+VS
Vout
Ref
-VS
R1 1206 110R
R4 1206 100
10V/K
Vin1
+15V
-15V
U4A
TL052
A
R31 1206 100k
R13 1206 3k3
R3 1206 2k2
R2 1206 1k
R14 1206 100k
R29 1206 82k
R30 1206 12k
U4B
TL052
B
Vset1
1V/10K
R32 1206 12k
R33 1206 82k
P4
NTC2
R8 10k
Put resistor on socket
R7 1206 110R
R9 3RPot 1K
U3
AD8421
R10 1206 100
Vin2
R11 0805 10k
R12 0805 10k
P14
Switch
GND-LD
P10
LD
P5 Polarity LD
Change Diode direction depending on LD Polarity
J7
COAX-F
D1 7V5
D2 Diode
P8
Polarity LD
P7
NTC2-Control
J2
COAX-F
J1
D Connector 15
Vset1
Vin1
Vin2
-15Vin
+15Vin
OUT1-
OUT1+
OUT2-
OUT2+
P1
OUT1
P3
OUT2
L1 NFM41P
L2 NFM41P
C13 1206 2.2uF
C14 1206 2.2uF
C1 0805 100nF
C2 0805 100nF
C3 0805 100nF
C4 0805 100nF
C7 0805 100nF
C6 0805 100nF
C10 0805 100nF
U1
REF01CS
IN
NC
NC
GND
OUT
NC
NC
TRIM
C5 0805 100nF
TempPID V8.0 Messbrücke TA
Title
Size: A3
Number:
Date: 18.05.2015
Time: 17:
File: Q:\CsIII\Documents\Drawi

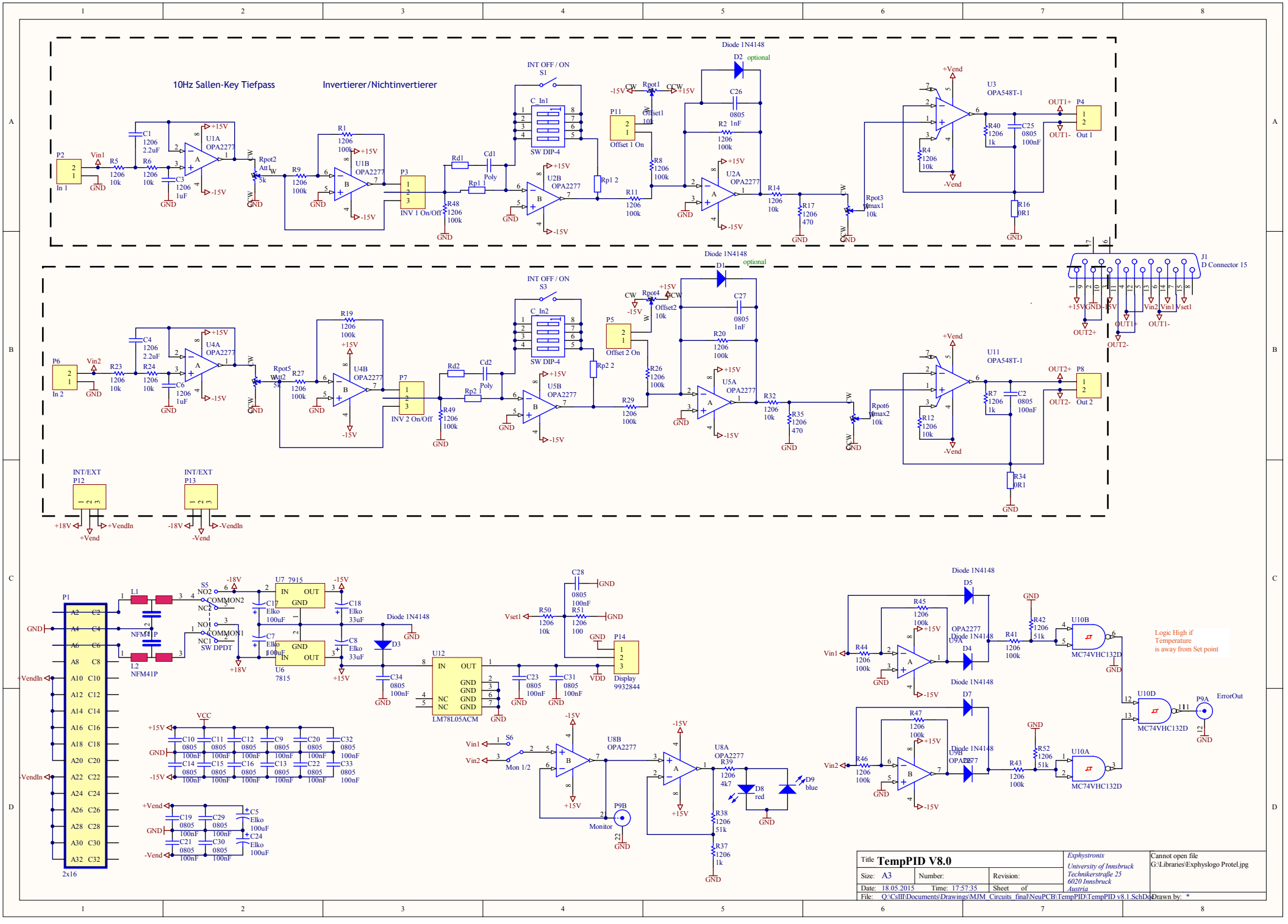
10Hz Sallen-Key Tiefpass
Invertierer/Nichtinvertierer
INT OFF / ON
S1
S3
SW DIP-4
C_In1
C_In2
Diode 1N4148
D1
D2
optional
P2
In 1
P6
In 2
P3
INV 1 On/Off
P7
INV 2 On/Off
P11
Offset 1 On
P5
Offset 2 On
U1A OPA2277
U1B OPA2277
U2A OPA2277
U2B OPA2277
U4A OPA2277
U4B OPA2277
U5A OPA2277
U5B OPA2277
U3 OPA548T-1
U11 OPA548T-1
P4
Out 1
P8
Out 2
OUT1+
OUT1-
OUT2+
OUT2-
J1
D Connector 15
INT/EXT
P12
P13
+18V
+Vend
+VendIn
-18V
-Vend
-VendIn
P1
2x16
S5
NO2
COMMON2
NC2
NO1
COMMON1
NC1
SW DPDT
L1
L2
NFM41P
U7 7915
U6 7815
Elko
Diode 1N4148
D3
U12
LM78L05ACM
P14
Display
9932844
VCC
S6
Mon 1/2
Monitor
P9B
U8B OPA2277
U8A OPA2277
D8
red
D9
blue
Diode 1N4148
D4
D5
D7
U9A OPA2277
U9B OPA2277
U10B
U10D
U10A
MC74VHC132D
Logic High if
Temperature
is away from Set point
P9A
ErrorOut
Title TempPID V8.0
Size: A3
Number:
Revision:
Date: 18.05.2015
Time: 17:57:35
Sheet of
File: Q:\CsIII\Documents\Drawings\MJM_Circuits_final\NeuPCB\TempPID\TempPID v8.1.SchDoc
Exphystronix
University of Innsbruck
Technikerstraße 25
6020 Innsbruck
Austria
Cannot open file
G:\Libraries\Exphyslogo Protel.jpg
Drawn by: *

A.4. Assembly of the Vacuum Chamber

In this Appendix, we describe the main steps of the assembly of the vacuum chamber. Figure A.2 shows the base plate of the cavity with the copper plate on the Peltier elements. The Peltier elements are not glued and therefore we fix the positions slightly with Kapton™ tape. The copper plate is screwed to the base plate with plastic screws for better thermal isolation and to reduce the force acting on the Peltier elements. Figure A.3 shows the inside of the vacuum chamber without the shieldings. The lower flange is placed on the copper plate. We used tin foil between the Peltier elements and the lower flange to increase the thermal contact and fixed the position of the Peltier elements again with Kapton™ tape. The NTCs are glued[1] into small holders (see Fig. A.7), which are screwed onto the vacuum chamber at different positions. Figure A.4 shows the outer shielding sitting on the Pelter elements. On both sides of the shieldings windows are glued into holes (see Fig. A.5). On the bottom of the outer shielding, see Fig. A.6, spacers out of Teflon and additional holders for NTCs are placed. The outer shielding is screwed onto the lower flange with vacuum compatible M2.5 screws[2]. The Teflon spacers reduce the thermal contact from the inner shielding to the outer one. Figure. A.8 shows the cavity sitting on the V-shaped aluminum block inside the inner shielding. To monitor the temperature of the aluminum holder two NTCs are glued into two holes on the side of the aluminum block. The inner shielding is closed (Fig. A.9) and the wires for to the NTC are guided through a hole in the top of the shielding to the feedthrough.

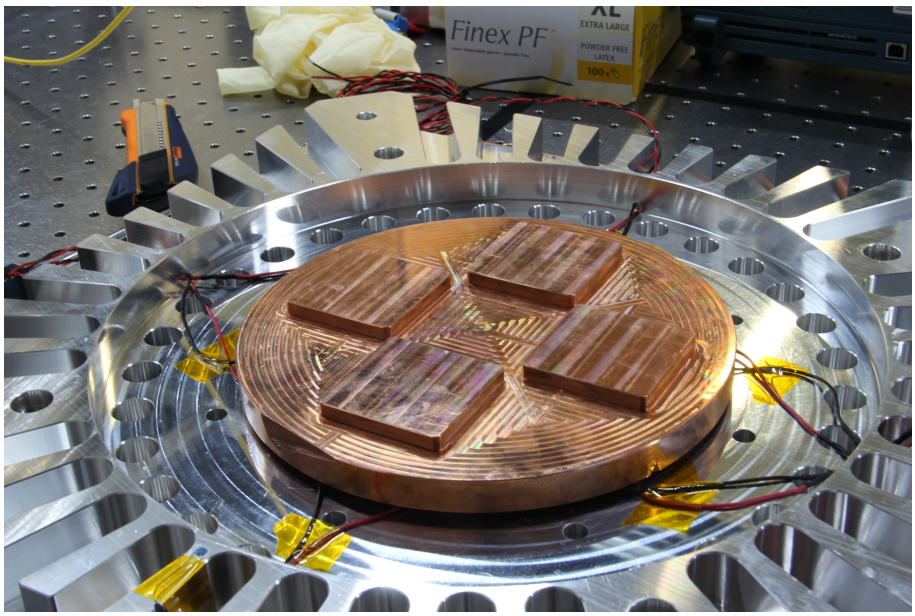

Figure A.2.: Heat sink of the vacuum chamber with the additional copper plate. Between the copper plate and the heat sink six Peltier elements are placed to temperature stabilize the copper plate.

[1]The NTCs are glued with Torr Seal.
[2]Vacom, VFC-2.506-25 and VFC-2.510-25.

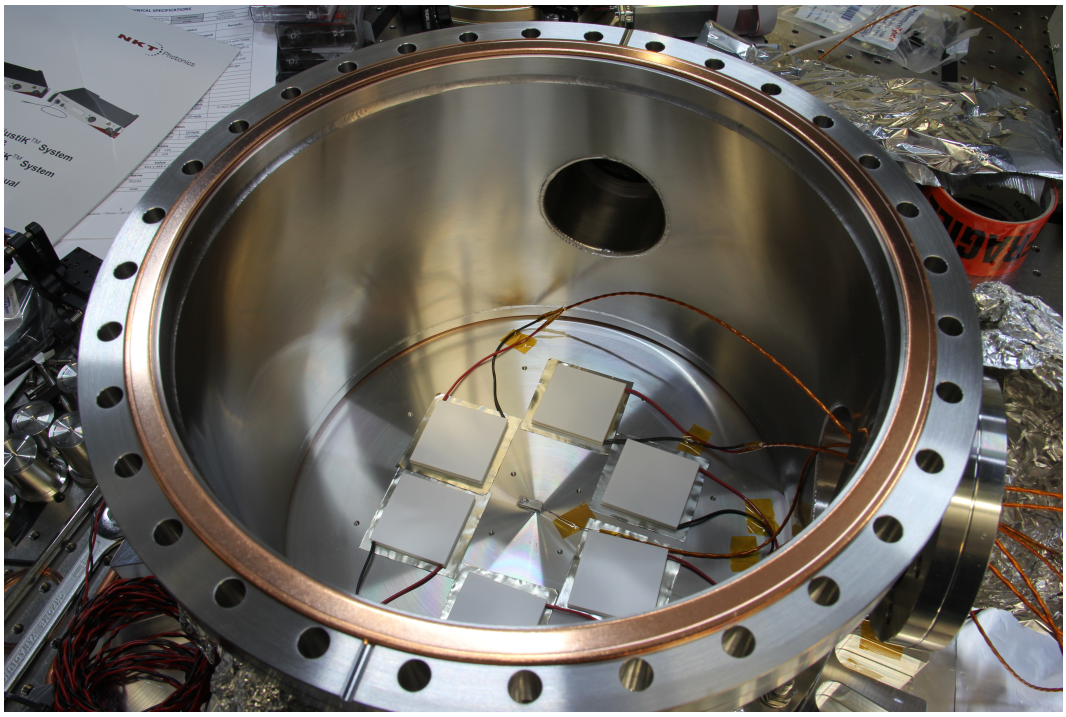

Figure A.3.: Framework of the vacuum chamber with Pelter elements inside. The positions of the Peltier elements are fixed with Kapton™and holders for the NTC are screwed on at different positions.

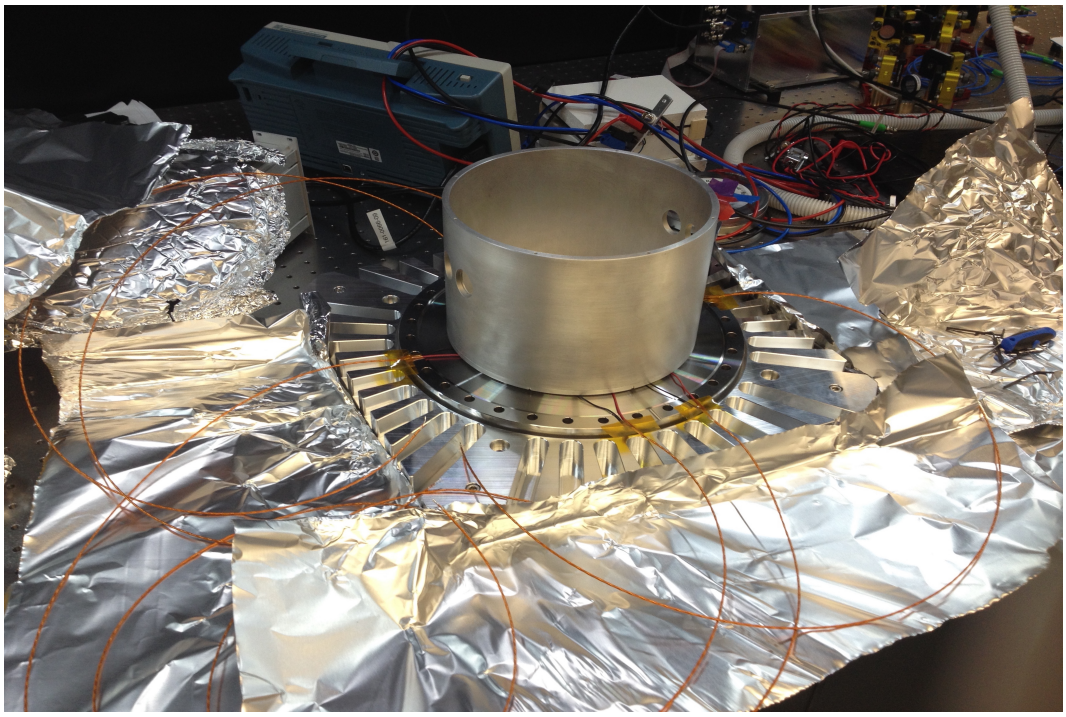

Figure A.4.: The outer shielding sits on the Pelter elements on the lower flange.

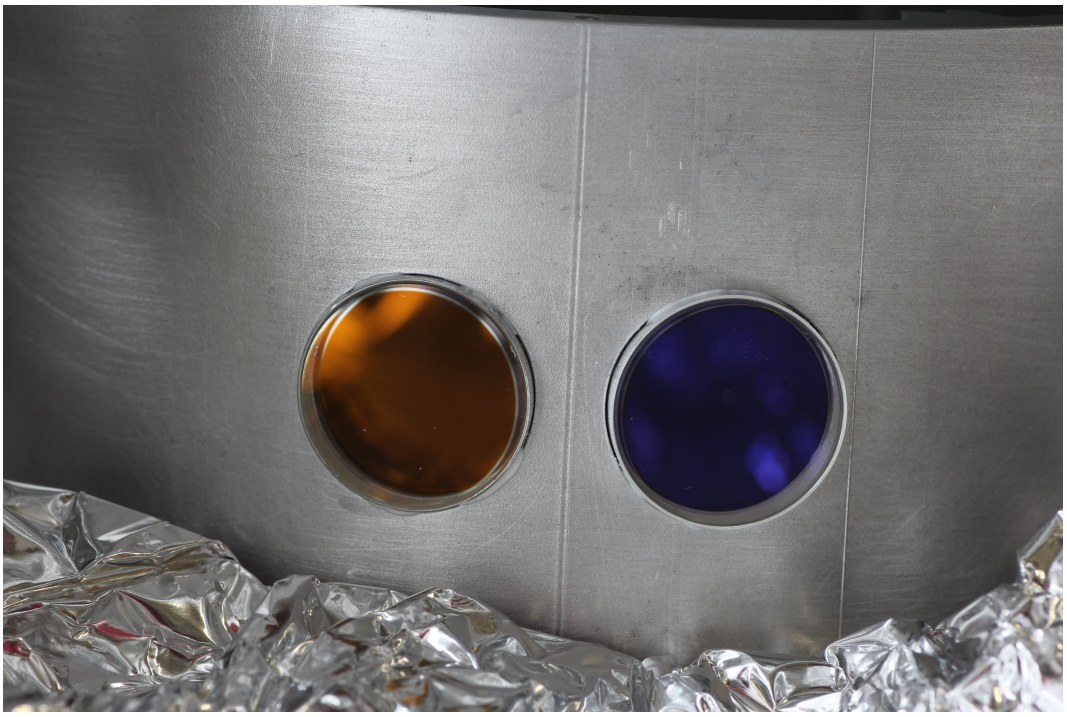

Figure A.5.: Windows on the outer and inner shielding are glued in. They are coated for the necessary linewidths, respectively.

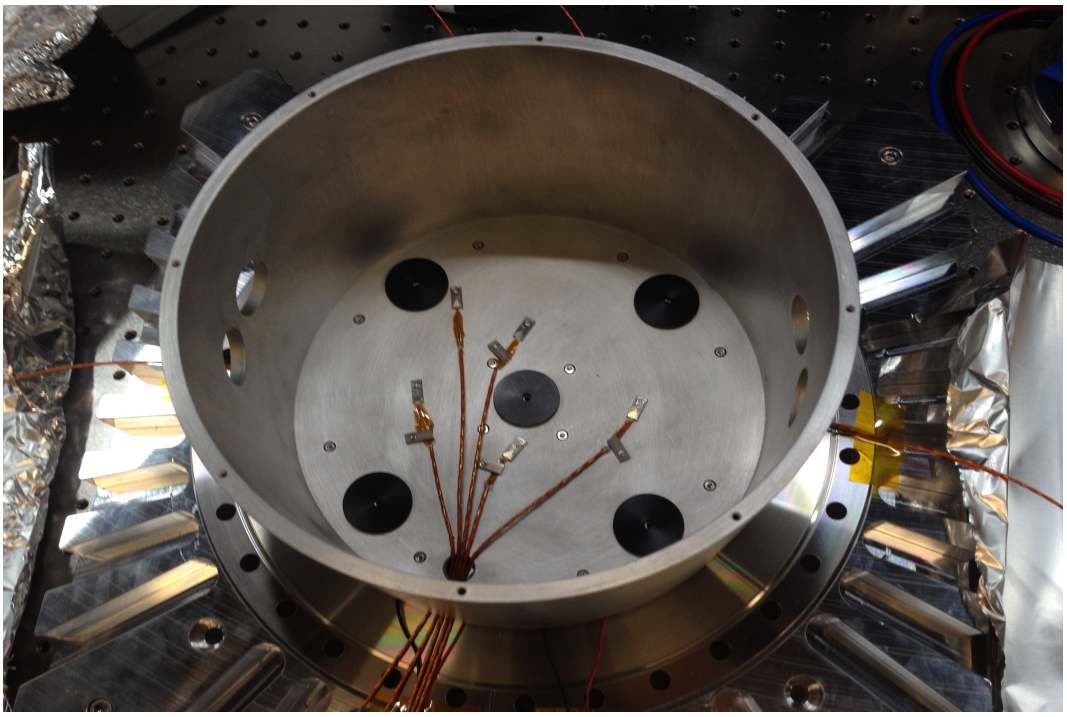

Figure A.6.: Inside of the outer shielding. The inner one is sitting on Teflon spacer to reduce the thermal contact.

Figure A.7.: NTCs are glued into holders which can be screwed onto the vacuum chamber.

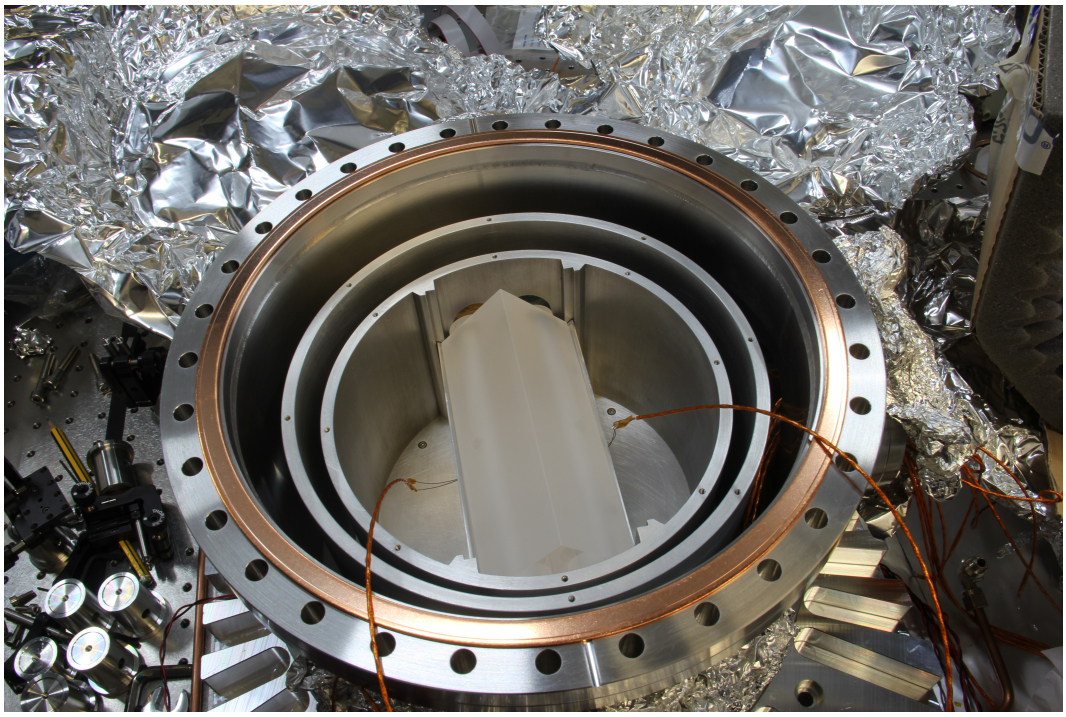

Figure A.8.: Open chamber with ULE cavity inside.

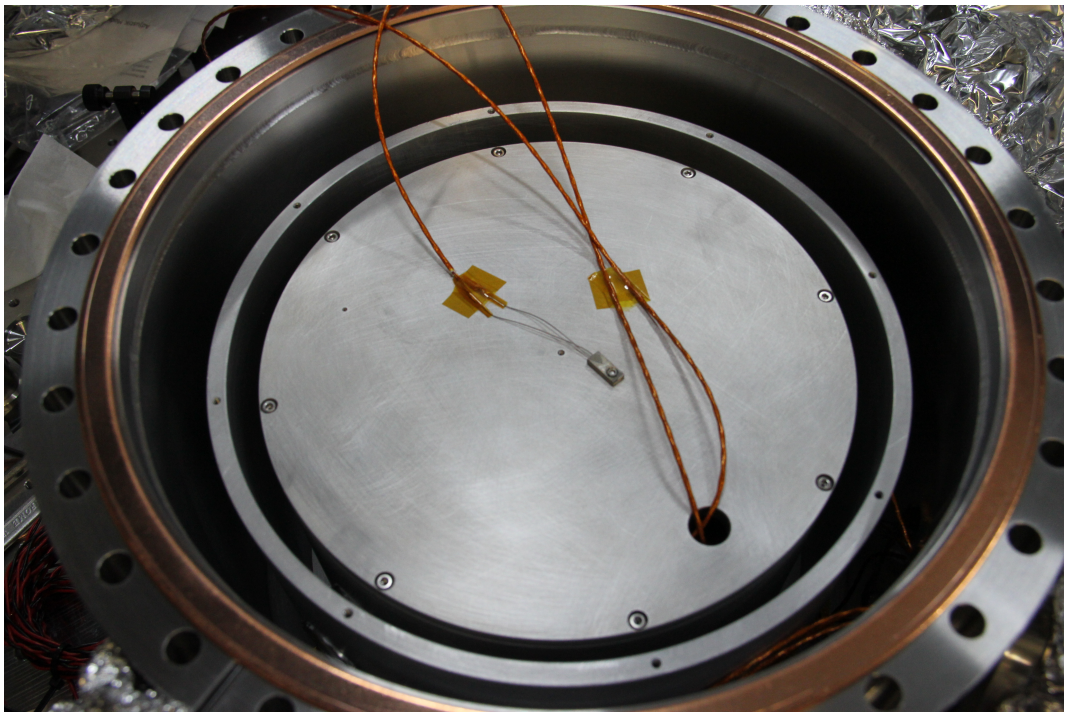

Figure A.9.: Both shieldings are closed and an additional temperature sensor is screwed on the top.

Bibliography

[1] K. Aikawa et al. *Bose-Einstein Condensation of Erbium*. Phys. Rev. Lett. 108 (2012), p. 210401.

[2] K. Aikawa et al. *Observation of Fermi surface deformation in a dipolar quantum gas*. Science 345. (2014), pp. 1484–1487.

[3] J. F. Allen and A. D. Misener. *Flow of Liquid Helium II*. Nature 141. (1938), pp. 75–75.

[4] J. Alnis et al. *Subhertz linewidth diode lasers by stabilization to vibrationally and thermally compensated ultralow-expansion glass Fabry-Pérot cavities*. Phys. Rev. A 77 (2008), p. 053809.

[5] M. H. Anderson et al. *Observation of Bose-Einstein Condensation in a Dilute Atomic Vapor*. Science 269. (1995), pp. 198–201.

[6] J. B. Balewski. *A single electron in a Bose-Einstein condensate*. PhD thesis. University of Stuttgart, 2014.

[7] Jonathan B. Balewski et al. *Coupling a single electron to a Bose–Einstein condensate*. Nature 502. (2013), pp. 664–667.

[8] H. Y. Ban et al. *Laser cooling transitions in atomic erbium*. Opt. Express 13. (2005), pp. 3185–3195.

[9] J. Bardeen, L. N. Cooper, and J. R. Schrieffer. *Microscopic Theory of Superconductivity*. Phys. Rev. 106 (1957), pp. 162–164.

[10] J. G. Bednorz and K. A. Mueller. *Possible high Tc Superconductivity in the Ba–La–Cu–O System*. Zeitschrift fuer Physik B Condensed Matter 64 (1986), pp. 189–193.

[11] A. J. Berglund, J. L. Hanssen, and J. J. McClelland. *Narrow-Line Magneto-Optical Cooling and Trapping of Strongly Magnetic Atoms*. Phys. Rev. Lett. 100 (2008), p. 113002.

[12] E. D. Black. *An introduction to Pound-Drever-Hall laser frequency stabilization*. American Journal of Physics 69. (2001), pp. 79–87.

[13] C. C. Bradley et al. *Evidence of Bose-Einstein Condensation in an Atomic Gas with Attractive Interactions*. Phys. Rev. Lett. 75 (1995), pp. 1687–1690.

[14] N. Q. Burdick et al. *Fermionic Suppression of Dipolar Relaxation*. Phys. Rev. Lett. 114 (2015), p. 023201.

[15] Lisheng Chen et al. *Vibration-induced elastic deformation of Fabry-Perot cavities*. Phys. Rev. A 74 (2006), p. 053801.

[16] Y.C. Chen et al. *Effect of the trapping laser linewidth on the atom number in a magneto-optical trap*. Chinese Journal of Physics 38. (2000), pp. 920–926.

[17] C. Chin et al. *Feshbach resonances in ultracold gases*. Rev. Mod. Phys. 82 (2010), pp. 1225–1286.

[18] C. Chin et al. *Observation of the Pairing Gap in a Strongly Interacting Fermi Gas*. Science 305. (2004), pp. 1128–1130.

[19] J. K. Chin et al. *Evidence for superfluidity of ultracold fermions in an optical lattice*. Nature 443 (Oct. 2006), pp. 961–964.

[20] C. B. Connolly et al. *Large spin relaxation rates in trapped submerged-shell atoms*. Phys. Rev. A 81 (2010), p. 010702.

[21] J. G. Conway and B. G. Wybourne. *Low-Lying Energy Levels of Lanthanide Atoms and Intermediate Coupling*. Phys. Rev. 130 (1963), pp. 2325–2332.

[22] K. B. Davis et al. *Bose-Einstein Condensation in a Gas of Sodium Atoms*. Phys. Rev. Lett. 75 (1995), pp. 3969–3973.

[23] W. Demtröder. *Experimentalphysik 3*. Springer Berlin Heidelberg, 2010.

[24] D. Dreon et al. *Optical cooling and trapping highly magnetic atoms: The benefits of a spontaneous spin polarization*. ArXiv e-prints (2016).

[25] R. W. P. Drever et al. *Laser phase and frequency stabilization using an optical resonator*. App. Phys. B 31. (1983), pp. 97–105.

[26] P. Dubé et al. *A narrow linewidth and frequency-stable probe laser source for the 88Sr+ single ion optical frequency standard*. Applied Physics B 95. (2009), pp. 43–54.

[27] F. B. Dunning et al. *Recent advances in Rydberg physics using alkaline-earth atoms*. Journal of Physics B: Atomic, Molecular and Optical Physics 49. (2016), p. 112003.

[28] J. Eichler and H.J. Eichler. *Laser: Bauformen, Strahlführung, Anwendungen*. Physics and astronomy online library. Springer, 2003.

[29] J. Ferch, W. Dankwort, and H. Gebauer. *Hyperfine structure investigations in DyI with the atomic beam magnetic resonance method*. Phys. Lett. A 49. (1974), pp. 287 –288.

[30] Richard P. Feynman. *Simulating physics with computers*. International Journal of Theoretical Physics 21. (1982), pp. 467–488.

[31] C.J. Foot. *Atomic physics*. Oxford University Press, 2005.

[32] A. Frisch. *Dipolar Quantum Gases of Erbium*. PhD thesis. University of Innsbruck, 2014.

[33] A. Frisch et al. *Narrow-line magneto-optical trap for erbium*. Phys. Rev. A 85 (2012), p. 051401.

[34] A. Frisch et al. *Quantum chaos in ultracold collisions of gas-phase erbium atoms*. Nature 507 (2014), pp. 475–479.

[35] T.F. Gallagher. *Rydberg Atoms*. Cambridge Monographs on Atomic. Cambridge University Press, 2005.

[36] J. Goldwin et al. *Two-species magneto-optical trap with* ^{40}K *and* ^{87}Rb. Phys. Rev. A 65 (2002), p. 021402.

[37] M. Greiner et al. *Quantum phase transition from a superfluid to a Mott insulator in a gas of ultracold atoms*. Nature 415. (2002), pp. 39–44.

[38] A. Griesmaier et al. *Bose-Einstein Condensation of Chromium*. Phys. Rev. Lett. 94 (2005), p. 160401.

[39] R. Grimm. *Ultracold Fermi gases in the BEC-BCS crossover: a review from the Innsbruck perspective*. eprint arXiv:cond-mat/0703091 (Mar. 2007).

[40] R. Gross and A. Marx. *Festkörperphysik*. Oldenbourg Wissenschaftsverlag, 2012.

[41] W. Hogervorst et al. *Isotope shifts and hyperfine structure of natural dysprosium*. Physics Letters A 65. (1978), pp. 220 –222.

[42] W. G. Jin et al. *Hyperfine Structure and Isotope Shift in Er I by the Atomic-Beam Laser Spectroscopy*. Journal of the Physical Society of Japan 59. (1990), pp. 3148–3154.

[43] H. Kamerlingh Onnes. *The Superconductivity of Mercury*. Leiden Com. (1911).

[44] P. Kapitza. *Viscosity of Liquid Helium below the λ-Point*. Nature 141. (1938), pp. 74–74.

[45] J. Keller et al. *Simple vibration-insensitive cavity for laser stabilization at the 10-16 level*. App. Phys. B 116. (2014), pp. 203–210.

[46] G. Kirchmair. *Frequency stabilization of a Titanium-Sapphire laser for precision spectroscopy on Calcium ions*. MA thesis. University of Innsbruck, 2006.

[47] E. Kirilov et al. *Compact, robust, and spectrally pure diode-laser system with a filtered output and a tunable copy for absolute referencing*. Applied Physics B 119. (2015), pp. 233–240.

[48] T. Lahaye et al. *d-Wave Collapse and Explosion of a Dipolar Bose-Einstein Condensate*. Phys. Rev. Lett. 101 (2008), p. 080401.

[49] T. Lahaye et al. *The physics of dipolar bosonic quantum gases*. Reports on Progress in Physics 72. (2009), p. 126401.

[50] N. Leefer, A. Cingöz, and D. Budker. *Measurement of hyperfine structure and isotope shifts in the Dy 421 nm transition*. Opt. Lett. 34. (2009), pp. 2548–2550.

[51] T. Legero, T. Kessler, and U. Sterr. *Tuning the thermal expansion properties of optical reference cavities with fused silica mirrors*. J. Opt. Soc. Am. B 27. (2010), pp. 914–919.

[52] Y. Liu and P. H. Daum. *Relationship of refractive index to mass density and self-consistency of mixing rules for multicomponent mixtures like ambient aerosols*. Journal of Aerosol Science 39. (2008), pp. 974 –986.

[53] M. Lu. *Quantum Bose and Fermi Gases of Dysprosium: Production and Initial Study*. MA thesis. Stanford University, 2014.

[54] M. Lu, S. H. Youn, and B. L. Lev. *Trapping Ultracold Dysprosium: A Highly Magnetic Gas for Dipolar Physics*. Phys. Rev. Lett. 104 (2010), p. 063001.

[55] M. Lu et al. *Strongly Dipolar Bose-Einstein Condensate of Dysprosium*. Phys. Rev. Lett. 107 (2011), p. 190401.

[56] Mingwu Lu, Seo Ho Youn, and Benjamin L. Lev. *Spectroscopy of a narrow-line laser-cooling transition in atomic dysprosium*. Phys. Rev. A 83 (2011), p. 012510.

[57] R. Löw et al. *An experimental and theoretical guide to strongly interacting Rydberg gases*. Journal of Physics B: Atomic, Molecular and Optical Physics 45. (2012), p. 113001.

[58] T Maier. *Interactions in a Quantum Gas of Dysprosium Atoms*. PhD thesis. University of Stuttgart, 2015.

[59] T. Maier et al. *Broad universal Feshbach resonances in the chaotic spectrum of dysprosium atoms*. Phys. Rev. A 92 (2015), p. 060702.

[60] T. Maier et al. *Emergence of Chaotic Scattering in Ultracold Er and Dy*. Phys. Rev. X 5 (2015), p. 041029.

[61] T. Maier et al. *Narrow-line magneto-optical trap for dysprosium atoms*. Opt. Lett. 39. (2014), pp. 3138–3141.

[62] M. J. Mark. *Wechselwirkungseffekte eines Caesium-BEC in eindimensionalen Gittern*. MA thesis. University of Innsbruck, 2007.

[63] D. J. McCarron, S. A. King, and S. L. Cornish. *Modulation transfer spectroscopy in atomic rubidium*. Measurement Science and Technology 19. (2008), p. 105601.

[64] J. J. McClelland and J. L. Hanssen. *Laser Cooling without Repumping: A Magneto-Optical Trap for Erbium Atoms*. Phys. Rev. Lett. 96 (2006), p. 143005.

[65] P. McQuillen et al. *Imaging the Evolution of an Ultracold Strontium Rydberg Gas*. Phys. Rev. A 87 (2013), p. 013407.

[66] W. Meissner and R. Ochsenfeld. *Ein neuer Effekt bei Eintritt der Supraleitfähigkeit*. Naturwissenschaften 21. (1933), pp. 787–788.

[67] P. J. Mohr, D. B. Newell, and B. N. Taylor. *CODATA recommended values of the fundamental physical constants: 2014**. Rev. Mod. Phys. 88 (2016), p. 035009.

[68] B. Pasquiou et al. *Spin Relaxation and Band Excitation of a Dipolar Bose-Einstein Condensate in 2D Optical Lattices*. Phys. Rev. Lett. 106 (2011), p. 015301.

[69] R. K. Raj et al. *High-Frequency Optically Heterodyned Saturation Spectroscopy Via Resonant Degenerate Four-Wave Mixing*. Phys. Rev. Lett. 44 (1980), pp. 1251–1254.

[70] C. A. Regal, M. Greiner, and D. S. Jin. *Observation of Resonance Condensation of Fermionic Atom Pairs*. Phys. Rev. Lett. 92 (2004), p. 040403.

[71] A. Rietzler. *Narrow-Line Cooling Light for a Magneto-Optical Trap of Erbium Atoms*. MA thesis. University of Innsbruck, 2012.

[72] B.E.A. Saleh and M.C. Teich. *Fundamentals of photonics*. Wiley series in pure and applied optics. Wiley, 1991.

[73] P. Schauß et al. *Observation of spatially ordered structures in a two-dimensional Rydberg gas*. Nature 491. (2012), pp. 87–91.

[74] M. Segel. *Stable and narrow-line diode-laser system for STIRAP*. MA thesis. University of Innsbruck, 2015.

[75] D. M. Stamper-Kurn and M. Ueda. *Spinor Bose gases: Symmetries, magnetism, and quantum dynamics.* Rev. Mod. Phys. 85 (2013), pp. 1191–1244.

[76] P. Unterwaditzer. *Aufbau eines vollstaendigen Diodenlasersystems zur Laserkuehlung und Detektion von gespeicherten Cs-Atomen.* MA thesis. University of Innsbruck, 2005.

[77] E. Urban et al. *Observation of Rydberg blockade between two atoms.* Nature Physics 5. (2009), pp. 110–114.

[78] M. Weidemüller. *Rydberg atoms: There can be only one.* Nature Physics 5. (2009), pp. 91–92.

[79] A. C. Wilson et al. *A 750-mW, continuous-wave, solid-state laser source at 313 nm for cooling and manipulating trapped 9Be+ ions.* Applied Physics B 105. (2011), pp. 741–748.

[80] B.G. Wybourne and L. Smentek. *Optical Spectroscopy of Lanthanides: Magnetic and Hyperfine Interactions.* CRC Press, 2007.

[81] S. H. Youn et al. *Dysprosium magneto-optical traps.* Phys. Rev. A 82 (2010), p. 043425.

[82] W. Zwerger. *The BCS-BEC Crossover and the Unitary Fermi Gas.* Lecture Notes in Physics. Springer Berlin Heidelberg, 2011.

Acknowledgement

First of all I want to thank Francesca for giving me the opportunity to do my master thesis in the RARE experiment. She supported me during the whole time, especially with the preparation of my seminar talk and during the writing phase of my thesis. Further, I want to thank her that she gave me the opportunity to participate at the "Enrico Fermi" Summer School in Varenna, which was a unique experience.

Ein großer Dank geht an alle Mitglieder des Erbium- sowie des RARE-Teams für ihre ständige Hilfsbereitschaft und Geduld bei offenen Fragen. Ein ganz besonderer Dank gilt an dieser Stelle Philipp, der mich von Beginn an bei der Masterarbeit unterstützt und bei Fragen immer ein offenes Ohr gehabt hat. Weiters danken möchte ich Manfred, der mir immer mit gutem Rat beiseite stand und mich sehr beim Schreiben der Masterarbeit unterstützt hat. Arno möchte ich für seine Hilfsbereitschaft mit LaTeX und das Lesen von Teilen der Arbeit danken. Ein Dank geht auch an Emil, der mir beim Bauen des Lasers im flexure design geholfen hat und auch sonst immer für Fragen zur Verfügung stand. Ein großer Dank geht auch an die Werkstatt des IQOQI, wo Stefan, Andreas und Bernhard immer wieder große Hilfsbereitschaft gezeigt haben. Abseits der Universität möchte ich mich bei der Fußballmannschaft des ASV Riffian-Kuens bedanken, wo ich während meines Studiums trotz sehr bescheidener Trainingspräsenz spielen durfte. Ein Dank geht auch an meine langjährigen Mitbewohner Paul und Hannes, mit denen ich einige tolle Jahre zusammen wohnen durfte.

Abschließend geht der allergrößte Dank noch an meine Eltern, meine Großeltern und meine Freundin, welche mich immer unterstützt und motiviert haben.

Leopold-Franzens-Universität Innsbruck

Eidesstattliche Erklärung

Ich erkläre hiermit an Eides statt durch meine eigenhändige Unterschrift, dass ich die vorliegende Arbeit selbständig verfasst und keine anderen als die angegebenen Quellen und Hilfsmittel verwendet habe. Alle Stellen, die wörtlich oder inhaltlich den angegebenen Quellen entnommen wurden, sind als solche kenntlich gemacht.

Die vorliegende Arbeit wurde bisher in gleicher oder ähnlicher Form noch nicht als Magister- /Master- /Diplomarbeit /Dissertation eingereicht.

Datum	Unterschrift